AIRBORNE HYPERSPECTRAL IMAGING FOR WETLAND MAPPING IN THE YUKON FLATS, ALASKA

By

Patrick Ryan Graham, B.A.

A Thesis Submitted in Partial Fulfillment of the Requirements for the Degree of

Master of Science

in

Geology

University of Alaska Fairbanks

May 2020

APPROVED:

Anupma Prakash, *Committee Chair*
Jordi Cristóbal Rosselló, *Committee Co-Chair*
Rudiger Gens, *Committee Member*
Paul McCarthy, *Chair*
    Department of Geosciences
Kinchel C. Doerner, *Dean*
    College of Natural Science and Mathematics
Michael Castellini, *Dean of the Graduate School*

Abstract

This study involved commissioning HySpex, a hyperspectral imaging system, on a single-engine Bush Hawk aircraft; using it to acquire images over selected regions of the Yukon Flats National Wildlife Refuge; establishing a complete processing flow to convert raw data to radiometrically and geometrically corrected hypercubes, and further processing the data to classify wetlands. Commissioning involved designing a customized mount to simultaneously install two-camera systems, one operating in the visible and near infrared region, and the other operating in the shortwave infrared region. Flight planning incorporated special considerations in choosing the flight direction, speed, and time windows to minimize effects of the Bidirectional Reflection Distribution Function (BRDF) that are more dominant in high latitudes. BRDF effects were further minimized through a special processing step, that was added to the established hyperspectral data processing chain developed by the German Space Agency (DLR). Instrument commissioning included a test flight over the University of Alaska Fairbanks for a bore-sight calibration between the HySpex system's two cameras, and to ensure the radiometric and geometric fidelity of the acquired images. Calibration resulted in a root mean square error of 0.5 pixels or less for images acquired from both cameras at 1-meter spatial resolution for each geometrically corrected flight line. Imagery was radiometrically corrected using the ATCOR-4 software package. No field spectra of the study areas were collected due to logistics constraints. However, a visual comparison between current spectral libraries and acquired hyperspectral image spectra was used to ensure spectral quality. For wetlands mapping, a 6-category legend was established based on previous United States Geological Survey and United States Fish and Wildlife Service information and maps, and three different classification methods are used in two selected areas: hybrid classification, spectral angle mapper, and maximum likelihood. Final maps were successfully

classified using a maximum likelihood method with high Kappa values and user's and producer's accuracy are more than 90% for nearly all categories. The maximum likelihood classifier generated the best wetland classification results, with a Kappa index of about 0.90. This was followed by the SAM classifier with a Kappa index of about 0.57 and lastly by the hybrid classifier that achieved a Kappa index of only 0.42. Recommendations for future work include using higher-accuracy GPS measurements to improve georectification, building a spectral library for Alaskan vegetation, collection of ground spectral measurements concurrently with flight image acquisition, and acquisition of LiDAR or RGB-photo derived digital surface models to improve classification efforts.

Table of Contents

List of Figures

List of Tables

List of Appendices

Publications related to and derived from this MSc Thesis

1. Cristóbal, J., P. Graham, M. Buchhorn and A. Prakash (2016) A new integrated high-latitude thermal and hyperspectral laboratory for characterization of land surface processes in Alaska's Arctic and boreal regions. Data. 1(2), 13; doi:10.3390/data1020013.

2. Prakash, A., J. Cristóbal, M. Buchhorn, P. Graham, M. Stuefer (2016). HyLab: a hyperspectral laboratory for surface water and vegetation characterization in Alaska's Arctic and boreal regions. The 14th International Circumpolar Remote Sensing Symposium, September 12-16, Homer, Alaska (oral presentation)

3. Cristóbal, J., M. Buchhorn, A. Prakash, and P. Graham (2016). Observations from field to space: a new integrated high-latitude hyperspectral laboratory for surface water and vegetation characterization in Alaska's Arctic and boreal regions. Arctic Observing Summit. March, 12-18, Fairbanks. (poster presentation)

4. Graham, P., J. Cristóbal (2016). Integrating Multiplatform Remote Sensing and Field Data to Estimate Surface Energy Fluxes in Arctic Ecosystems. Alaska Geological Society Technical Conference, April 22nd, University of Alaska Fairbanks, Fairbanks. (poster presentation)

5. Prakash, A., Buchhorn, M., Cristóbal, J., Kokaly, R. F., Graham, P., Waigl, C., Hampton, D., Werdon, M. (2015) Field-Based and Airborne Hyperspectral Imaging for Applied Research in the State of Alaska. AGU Fall meeting. December 14-18, San Francisco, USA. (poster presentation)

6. Graham, P.; Cristóbal, J.; A. Prakash. (2015) Integrating multiplatform remote sensing and field data to estimate energy fluxes under snow conditions in Arctic ecosystems. Alaska Space Grant Program Education and Research Symposium, April 23-24 Fairbanks, United States of America (poster presentation).

7. Cristóbal, J.; A. Prakash; P. Graham; M. C. Anderson; W. P. Kustas; C. Kongoli; C. Hain; E. Euskirchen; D.Toll. (2015) I Multitemporal estimation of surface energy fluxes in Alaska using the thermal-based two-source energy balance model: results in the Arctic Tundra. Alaska Space Grant Program Education and Research Symposium, April 23-24 Fairbanks, United States of America (oral presentation).

Acknowledgements

1   Introduction

Observed warming of surface air temperature over several decades has been linked to large-scale changes in the earth's climate system. Understanding the impacts of climate change on land, and the biogeochemical and biophysical feedbacks that the land surface has on climate is critical for human societies. Remote sensing has proven to be a powerful and efficient tool for timely and accurate mapping, monitoring, and quantification of biogeochemical and biophysical characteristics of land surfaces. Furthermore, remote sensing is particularly well-suited to investigations of remote and critically under-studied regions. One such region is the wetlands of Yukon Flats National Wildlife Refuge in Alaska. A detailed mapping and monitoring of vegetation cover is critical to understand how vegetation is responding to the rapidly changing climate, however current land cover maps are out of date and lack the resolution to accurately characterize the wetland ecosystem. Imaging spectroscopy or hyperspectral remote sensing has demonstrated strong potential for mapping and discrimination of spatially and compositionally diverse wetland vegetation. Through the development of airborne high-resolution hyperspectral image collection techniques suitable for high-latitudes and land-surface characterization of an Alaskan wetland, this study adds to the current body of knowledge to further understand and quantify the effects, impacts, and implications of a changing global climate.

1.1 Climate change and its impact in Interior Alaska

Global warming in recent decades is unequivocally apparent, with increases in surface air temperature being the most pronounced in the Arctic (Serreze and Barry, 2011). The "arctic amplification" of globally-rising air temperatures is leading to widespread melting of terrestrial snow and ice at high latitudes, sea-ice retreat, and a rise in the mean global sea level (Bates et al.,

2008; Meltofte, 2013). The ecological response to the climatic change is dramatic in Interior Alaska (Jorgenson et al., 2006, 2001; Solomon et al., 2007; Wendler and Shulski, 2009). Included among these changes are widespread and sometimes rapid degradation and thawing of permafrost (Jorgenson et al., 2006, 2001; Schuur et al., 2008; Solomon et al., 2007; Wendler and Shulski, 2009), increased occurrence and severity of wildfires (Duffy et al., 2007; Johnson, 1996; Randerson et al., 2006), decreased thickness and duration of winter snow cover (Wendler and Shulski, 2009), acceleration of the hydrologic cycle and increases in river discharge (Bintanja and Selten, 2014; Huntington, 2006; Lammers et al., 2001; Yang et al., 2003), and significant changes in vegetation (Bhatt et al., 2010; McGuire et al., 2002; Verbyla, 2008; Yang et al., 2003), among others.

The combination of warmer temperatures with constant or reduced precipitation may lead to a large decrease in water availability for natural and agricultural systems as well as for human needs (Jackson et al., 2001), especially in arid or semiarid areas such as Interior Alaska (Jung et al., 2010). Warmer and drier conditions have led to "browning" and higher tree mortality in the boreal forest (Goetz et al., 2005). Tree heights are increasing, and shrub cover is becoming denser and taller (Arctic Council, 2013; Meltofte, 2013). While the boreal forest is experiencing a browning effect, Arctic ecosystems have shown evidence over the past three decades of "greening" (Jia et al., 2003; Xu et al., 2013), with an approximate 14% increase in peak vegetation in the Arctic tundra (Bhatt et al., 2010). In addition, the ecotone between the tundra and forest is continually observed shifting northward. The changes in landscape in interior Alaska are particularly complex. Warmer temperatures have on the one hand caused drying and some browning of vegetation (Verbyla, 2008), and on the other hand have caused thawing of permafrost and development of wetlands (Jorgenson et al., 2001).

1.2 Wetland ecosystems

Wetlands ecosystems are a combination of terrestrial and aquatic ecosystems. Wetlands are characterized by substrates that are at least periodically saturated with, or covered by, water (Flagstad et al., 2013). Most terrestrial habitats gain water from precipitation and ground- and surface-water inputs and lose water through evapotranspiration and ground- and surface-water outflow. Wetland ecosystems however represent a water flux regime where inputs either exceed or are at least equal to outputs. The mechanisms for greater water input than output may result from combinations of high inflow, storage capacity, and low outflow within a wetland system (Figure 1. Components of the wetland water budget. ($P + SWI + GWI = ET + SWO + GWO + \Delta S$, where P is precipitation, SWI is surface-water inflow, SWO is surface-water outflow, GWI is ground water inflow, GWO is ground-water outflow, ET is evapotranspiration, and ΔS is change in storage.) Figure and caption
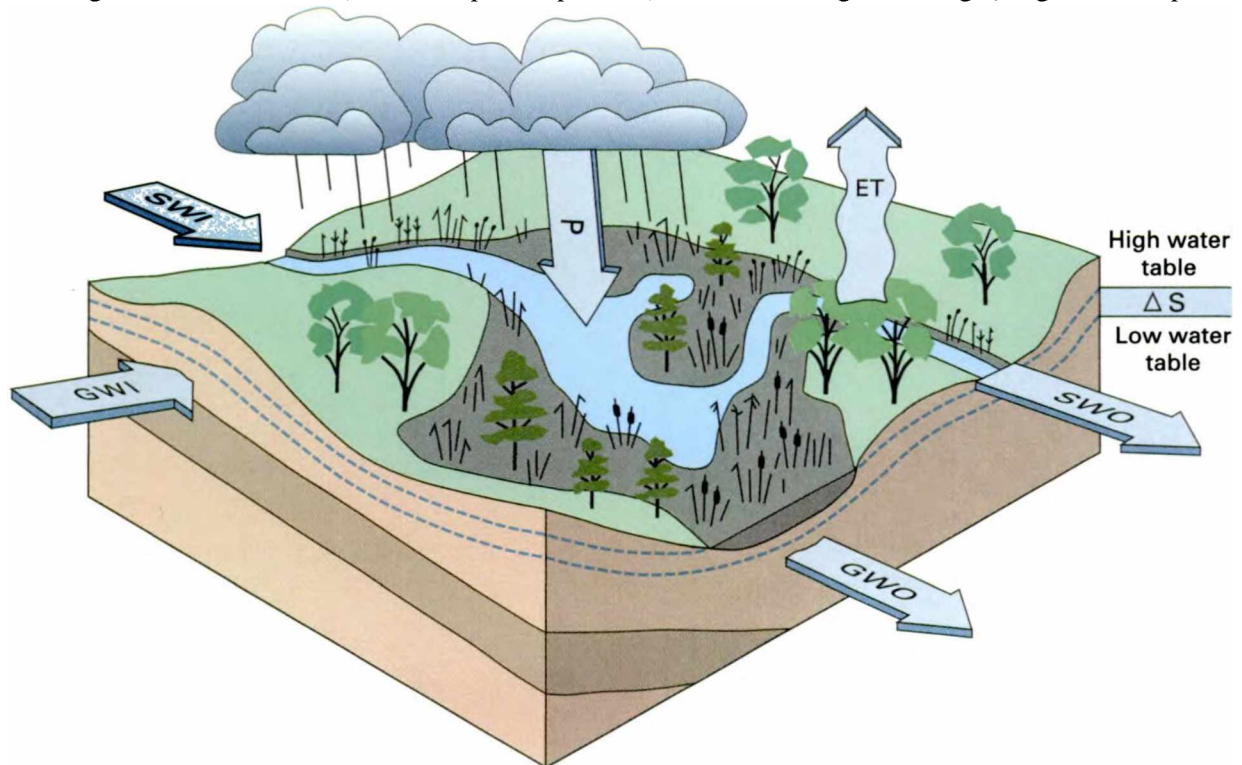
Figure 1. Components of the wetland water budget. ($P + SWI + GWI = ET + SWO + GWO + \Delta S$, where P is precipitation, SWI is surface-water inflow, SWO is surface-water outflow, GWI is ground water inflow, GWO is ground-water outflow, ET is evapotranspiration, and ΔS is change in storage.) Figure and caption from Carter, V. 1996. Wetland hydrology, water quality, and associated functions. National Water Summary on Wetland Resources, p. 36.

3

from Carter, V. 1996. Wetland hydrology, water quality, and associated functions. National Water Summary on Wetland Resources, p. 36.). Deepwater habitats are features found frequently within wetlands. These are permanently flooded areas, such as ponds and lakes that lack emergent vegetation, often occur due to topographic barriers (Cowardin et al., 2005), and include ponds, lakes, bays, sounds, fjords, lagoons, and inlets (Hall et al., 1994).

In Alaska, wetlands cover an estimated twenty two percent of the state's area according to the most recent survey carried out by Flagstad et al. (2013). The state's wetlands develop in areas of low topography, or along slope breaks where the groundwater table is at ground surface (Figure 2 upper panel A), and where shallow bedrock and low permeability layers of silt and clay horizons or ice-rich permafrost (Figure 2 lower panel C) inhibit water flux out of the wetland (Flagstad et
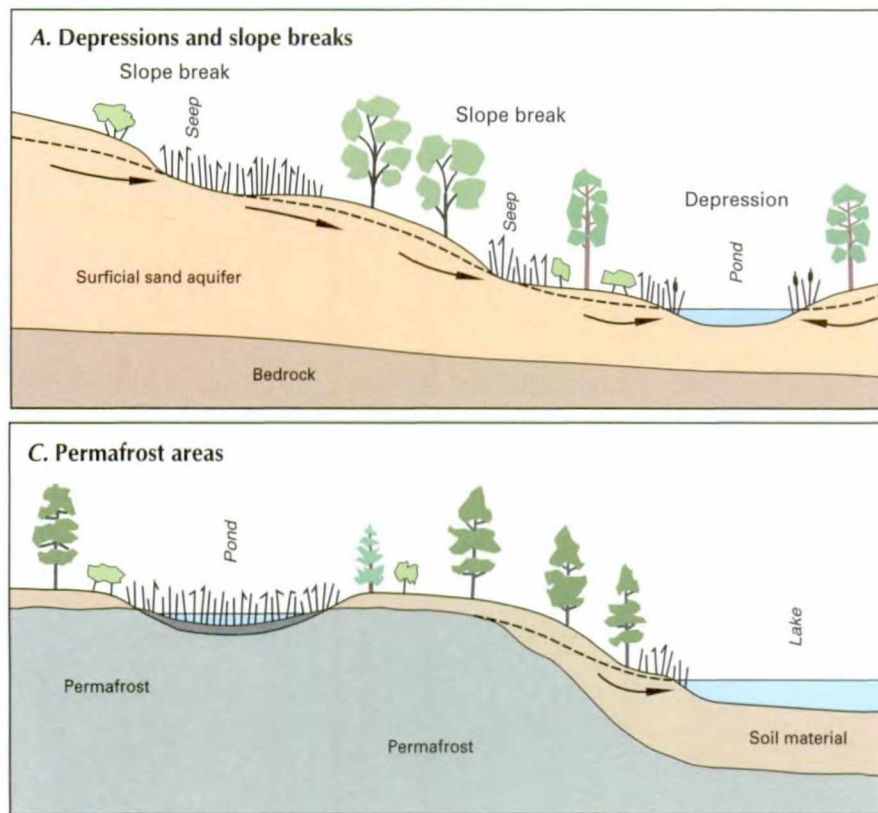
Figure 2. Predominant hydrogeologic settings for wetlands in Alaska. Upper panel (A), slope break and depression. Lower panel (C), permafrost areas. Figure from Carter, V. 1996. Wetland hydrology, water quality, and associated functions. National Water Summary on Wetland Resources, p. 42.

al., 2013; Carter, 1996). These barriers to water outflow produce water-saturated, low-oxygen hydric soils. The temporal and spatial variation of water amounts and levels in wetlands results in a highly diverse assemblage of plant species that are tolerant of changing hydrologic conditions and animal species whose life cycles require both terrestrial and aquatic habitats, while excluding plants and animals not adapted to the varying moisture regimes that occur in wetland ecosystems (Cowardin et al., 2005; Flagstad et al., 2013). The relative importance of each component in maintaining wetlands varies both spatially and temporally, but all these components interact to create the hydrology of an individual wetland (Carter, 1996).

Wetlands in Alaska represent an important habitat that provide essential ecosystem functions and many benefits to humans, plants, and animals from local to continental scales. These benefits include food and habitat for vegetation, wildlife, fish and shellfish species, food and habitat for human subsistence gathering, flood storage and stormflow modification, ground-water recharge and discharge, and maintenance of water quality (Carter, 1996; Hall et al., 1994). Wetlands can also influence local or regional weather and climate by moderating seasonal temperature fluctuations and local atmospheric circulation, affecting moisture convection, cloud formation, thunderstorms occurrence, and precipitation pattern change (Carter, 1996).

Alaska has lost less than one percent of its wetland area over the past 200 years, compared to an estimated fifty three percent loss in other states in the United States (Dahl, 1990). However, as global mean annual temperatures continue to rise and remain more pronounced for areas of high latitude, the stability of Alaska's wetland ecosystems may begin to deteriorate as the hydrological inputs necessary for wetland formation change in response. The many climate destabilizers that Interior Alaska is experiencing may cause wetland degradation specifically through thermal erosion, permafrost thaw, changing snow cover amounts and duration, shifting precipitation

patterns, and paludification (Chen et al., 2014; Flagstad et al., 2013; Jorgenson et al., 2001; Roach et al., 2013). In addition, degradation or loss of wetlands may result in significant changes in weather systems and alter precipitation patterns themselves (Carter, 1996).

Monitoring and describing changes to all physical, chemical, and biological parameters for Alaska wetlands is unrealistic in its scope and practical feasibility. However, using identified and interpreted proxies to assess the condition of an environment is a proven ecological method (Niemi and McDonald, 2004). Complex interactions between geology, topography, climate, and physical, biological, and chemical systems result in various hydrological regimes and wetland types, each with their own plant and animal species assemblages. With the increase in extremity of hydrological regime, the degree of specialization and fidelity of plant species increases (Tiner, 2012). Therefore, vegetation species assemblages may be used to infer wetland type and is the basis for the widely utilized Cowardin wetland classification system (Cowardin et al., 2005; Finlayson and van der Valk, 1995).

1.3 Hyperspectral remote sensing: an introduction

Traditionally, vegetation mapping and wetland inventories requires labor-intensive, costly, and time-consuming field work, including taxonomical information, collateral and ancillary data analysis, and the visual estimation of percentage cover for each species (Adam et al., 2010). This amount of work effort is exacerbated in Alaska from the added difficulty of accessing wetland areas that are far from population centers, road systems, or aircraft landing strips, and requires traversing difficult terrain to reach study areas. Remote sensing techniques offer an economical and practical alternative to discriminate and estimate biochemical and biophysical parameters of

6

wetland species (Adam et al., 2010), and to assist academic researches and government agencies in mapping and monitoring wetlands (Klemas, 2011; Ozesmi and Bauer, 2002).

Hyperspectral Imaging, also called Imaging Spectroscopy, is a remote sensing technique that acquires images in contiguous and narrow spectral regions (e.g. 400 to 2500 nm in steps of 0.3 nm) such that each spatial pixel in an image has a spectral reflectance curve (Kaufmann et al., 2012). Unlike multispectral sensors that may collect several to dozens of broad, targeted bands (e.g. 13 discrete bands within the 400 to 2500 nm region) and that utilize a subset of the spectrum, hyperspectral imaging uses continuous and contiguous ranges of wavelengths and collects hundreds of spectral bands. Certain materials have characteristic regions in the electromagnetic spectrum that reflect less or absorb more of incident electromagnetic radiation, known as absorption features (Figure 3).
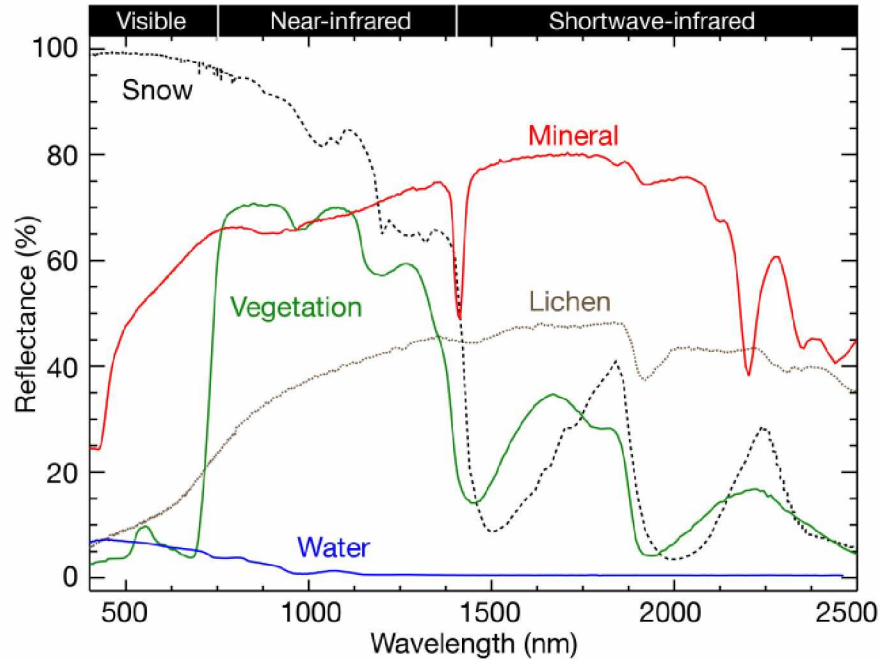
Figure 3. Selected reflectance spectra of Earth's surface materials. Spectra from the USGS Digital Spectral Library (speclab.cr.usgs.gov/spectral.lib06/)

7

Material absorption features relate to the harmonics and overtones of vibrational electronic transitions of chemical bonds that can be detected with narrow wavelength measurements. These features, while too small to be detected by multispectral sensors can be detected by the higher spectral resolution of hyperspectral imaging and enable identification of the materials that make up a scanned object (Kaufmann et al., 2012) (Figure 4). This level of spectral detail is promising for the improved mapping of wetlands (Adam et al., 2010; Govender et al., 2009; Klemas, 2011; Silva et al., 2008).

The varying location, depth, width, and shape of absorption features can be used to characterize material properties such as minerology (Clark et al., 2003), lithology (Bedini, 2009), soil type (Ben-Dor et al., 2002), or vegetation condition (Knipling, 1970). While many geological cover types contain minerals with easily identifiable and characteristic absorption features, the general shape of vegetation spectra are similar due to similar biochemical composition between species (Schmidt and Skidmore, 2003). Absorption features are broadened further along the spectrum due to multiple scattering within the photosynthetic structures of plants (Schmidt and Skidmore, 2003; Silva et al., 2008). However, as pigment concentrations, biochemical content, leaf characteristics, and canopy structure vary between different vegetation types, so does absorption and reflectance (Schmidt and Skidmore, 2003). Therefore, within a habitat, absorption features and reflectance may be used to determine different vegetation classes. By identifying the diagnostic absorption features and surface reflectance for land cover types, species and/or plant communities may be differentiated and classified.
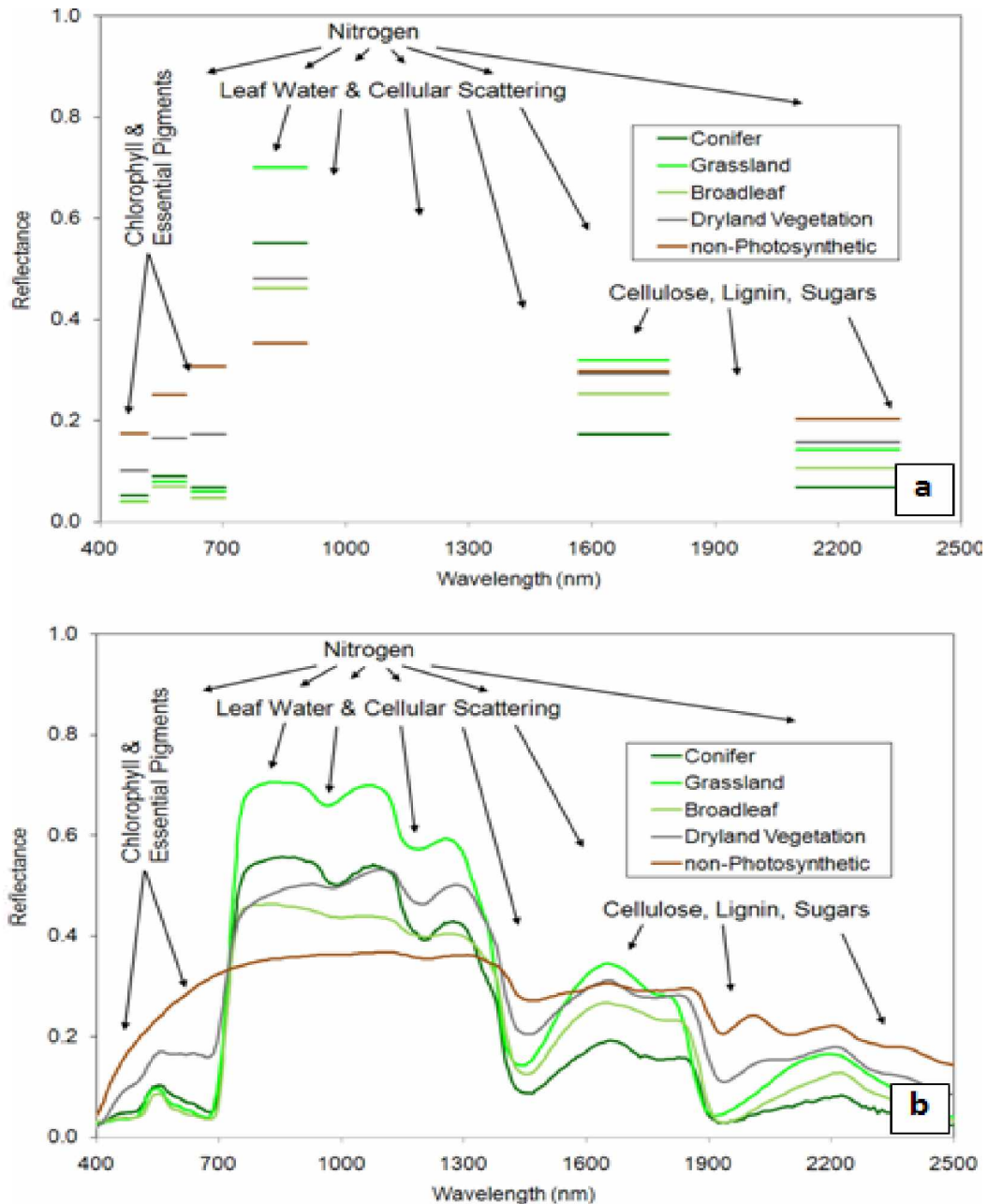
Figure 4. Vegetation spectra from a multispectral (a) and hyperspectral (b) sensor. From Green et al. (2017)

The structure and chemical composition of leaves determines the spectral response of vegetation (Figure 4**Error! Reference source not found.**). In the visible region of the spectrum (380 to 740 nm) the presence and concentration of pigments used plants for photosynthesis absorb a larger proportion of red (~740 to 600 nm) and blue (~400 to 500 nm) light than green light (~500

to 600 nm). These absorption features are diagnostic of healthy green vegetation in the visible wavelengths. Further absorption occurs beyond the 1300nm region of the spectrum where liquid water absorbs strongly near 1500, 1900, and 2600 nm. In the near infrared region (~800 to 2500 nm), incoming infrared energy is scattered and reflected strongly by refractive index discontinuities caused primarily by the interface between interstitial air or space and cell walls of the spongy mesophyll of a leaf (Silva et al., 2008). This jump in reflectance between the visible and near-infrared regions is commonly referred to as the red edge. Vegetation during senescence undergo desiccation that increases the air/cell wall interface scattering, and increases reflectance in the near-infrared wavelengths (Best et al., 1981; Silva et al., 2008). However, moderate stress results in a lower reflectance in the near-infrared region (Carter, 1993; Carter and Knapp, 2001). Additionally, vegetative stress will shift the red edge to lower wavelengths (Filella and Penuelas, 2007), and reduce the absorption of chlorophyll pigments, causing a "yellowing" effect in the visible spectrum as the reflectance of red and blue wavelengths increase in proportion to green wavelengths. In general terms, plant stress results in an increased visible reflectance due to lower absorption by pigments, a blue-shift in the red-edge reflectance feature, and overall decreased reflectance in the near-infrared until advanced desiccation of the leaf occurs and near-infrared absorption by water decreases and reflectance increases.
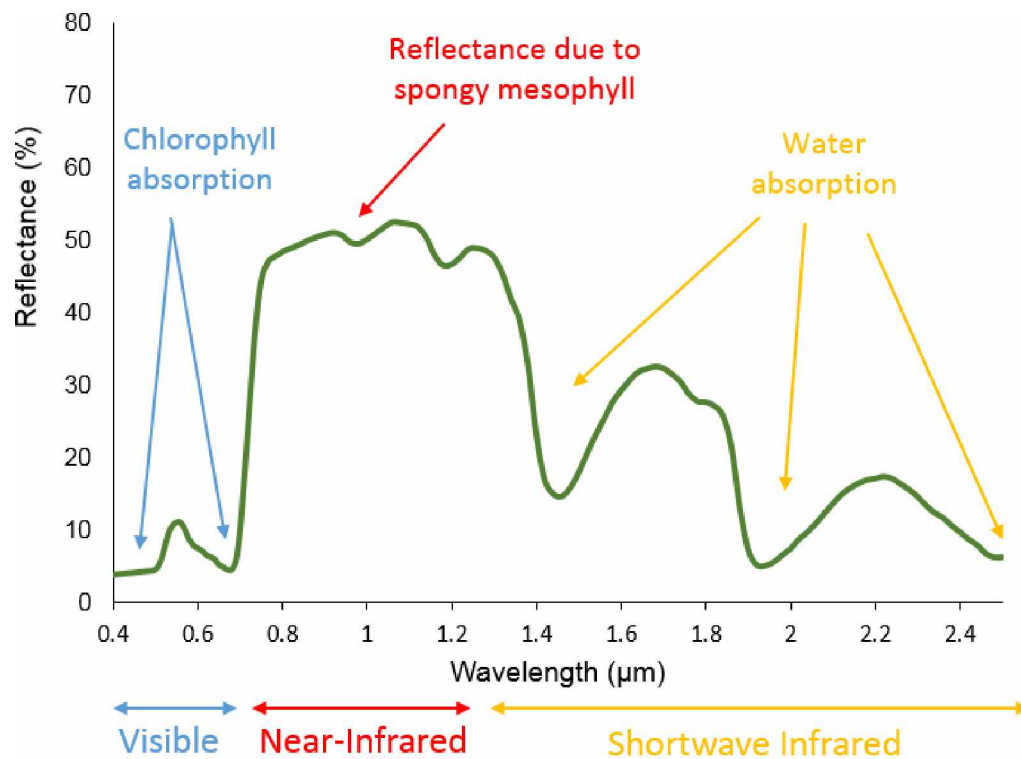
Figure 5. Vegetation spectral profile. Effects of pigments, leaf structure, and chemical composition of vegetation on reflectance at various regions of the electromagnetic spectrum shown. Source Humboldt State University GSP 216 Introduction to Remote Sensing (http://gsp.humboldt.edu/OLM/Courses/GSP_216_Online/lesson2-1/vegetation.html)

1.4. Goals and objectives

As previously stated, the larger goal of this study is to add to the current understanding of the biogeochemical and biophysical fluxes between the atmosphere and the land surface altered by climate change in an Alaskan wetland. Characterization of these fluxes first requires a detailed mapping of the land surface, and the development, deployment, and assessment of high-latitude hyperspectral remote sensing techniques and sensors to support wetland imaging.

The national wetland inventory for the state of Alaska is based almost entirely on 1978 to 1986, 1:60,000-scale, color-infrared imagery collected as part of the Alaska High Altitude Photography Acquisition Program, or AHAP, with only forty percent of the state's wetlands

having been mapped as of 2009 (Tiner, 2009). More recent inventories and studies of Alaskan wetlands (Chen et al., 2014; Flagstad et al., 2013; Jorgenson et al., 2004; Pastick et al., 2013; Roach et al., 2013) are often based on medium-resolution multi-spectral earth observation imagery, such as Landsat. Prior to 2015, there was no direct access to a research-grade hyperspectral imaging system in the state of Alaska that could be deployed for airborne hyperspectral remote sensing (Cristóbal et al., 2016). Imagery and studies utilizing hyperspectral imaging was limited to proposals seeking new data acquisitions utilizing the NASA AVIRIS sensor that were often uncompetitive when the full cost of deployments to Alaskan study sites were factored in. This is a reason why only one campaign of the thousands flown has been over Alaska since the NASA AVIRIS program started in 1987. Additionally, while orbital hyperspectral sensors such as Hyperion on board the EO-1 satellite have acquired high latitude imagery, there are several drawbacks to their use, especially in wetland studies including inadequate spatial resolution for upland wetland delineation and mapping (Klemas, 2011) and substantial periods of cloud cover during summer in high-latitudes that reduce the chance of quality data acquisition during a satellite overpass. In addition, low sun angles at high latitudes, even during midsummer introduce pronounced anisotropic effects to images, adding further complexity to hyperspectral remote sensing studies (Buchhorn, 2014).

This study focuses on accurate identification and delineation of vegetation types in a part of the Yukon Flats in interior Alaska using advanced airborne hyperspectral remote sensing techniques. The goal of this study is to demonstrate the capability of airborne hyperspectral imaging for wetland mapping using the Yukon Flats National Wildlife Refuge as a test case. Specific objectives are to:

1. Commission a hyperspectral imaging system, HySpex, in a small aircraft for airborne data acquisition in high-latitude environments;

2. correct for geometric distortions, and radiometric distortions that are uniquely inherent in a high-latitude environment;

3. develop image processing protocols to generate seamless mosaics, hypercubes, and thematically classified image products and;

4. map and characterize major vegetation and water types in the Yukon Flats.

This thesis is organized into six chapters, this chapter being the Introduction. In Chapter 2, the study area, the hyperspectral camera commissioning, and the data acquisition are presented. Chapter 3 describes all the data pre- and post-processing from bore-sight calibration to final image mosaicking. In Chapter 4, the three methodologies to map wetlands are presented. Chapter 5 is dedicated to presentation and discussion of the results. And finally, in Chapter 6, the main manuscript conclusions are drawn together and recommendations for future work are presented.

2. Study Area, Hyperspectral Camera Commissioning and Data Acquisition

The first steps in this research included selecting the research sites within the broader study area in the Yukon Flats National Wildlife Refuge, commissioning the Hyspex imaging system in an aircraft, and then acquiring imagery over the selected sites.

2.1. Study area

The study area (Figure 6) is located within the Yukon Flats National Wildlife Refuge in north-central Interior Alaska. The refuge encompasses an area of approximately 11,000 sq mi (28,490 km^2). It is centered on the confluence of the Yukon River, Porcupine River, and Chandalar River, laying between the Brooks Range to the north and the White and Crazy mountains to the south, and extends for 360 km east to west along the Arctic Circle, between 65° 45' and 67° 30' north latitude and 142° 30' and 150° 00' west longitude. The area has low relief, and is situated upon a broad plain of active and abandoned poorly-drained alluvial floodplain deposits with a high water table (Heglund and Jones, 2003).

The Refuge experiences a cold continental subarctic climate, with extremes of temperature and solar radiation between summer and winter. Although the refuge lacks long records of historical meteorological data, the Fairbanks International Airport, located roughly 150 km south of the refuge experiences a similar climate and based on National Climatic Data Center values from 1951 to 2009 (Chen et al., 2014) records a mean annual temperature of -3° C, mean January temperature of -23° C, and mean July temperature of 17° C. Annual precipitation at Fairbanks International Airport is 26.7 cm water equivalent with snow cover from October through April (Chen et al., 2014).

Much of the Yukon Flats is underlain by discontinuous permafrost (Pastick et al., 2013), which substantially affects the surface and subsurface hydrology. Approximately 40,000 shallow lakes cover an area of 1,147 km², and are mainly oxbow or thermokarst type lakes (Arp and Jones, 2009). Although the area receives little annual precipitation, permafrost layers inhibit water movement and drainage, and permafrost thaw leads to the development of shallow thermokarst lakes (Arp and Jones, 2009; Chen et al., 2014; Heglund and Jones, 2003; Shur et al., 2012). In addition, the short ice-free season in the region limit water loss due to evapotranspiration (Ford and Bedford, 1987). There are closed lakes (no outlet) and open lakes (with outlets) found within the Yukon flats with some lakes having direct contact with the groundwater table (Talik) (Heglund
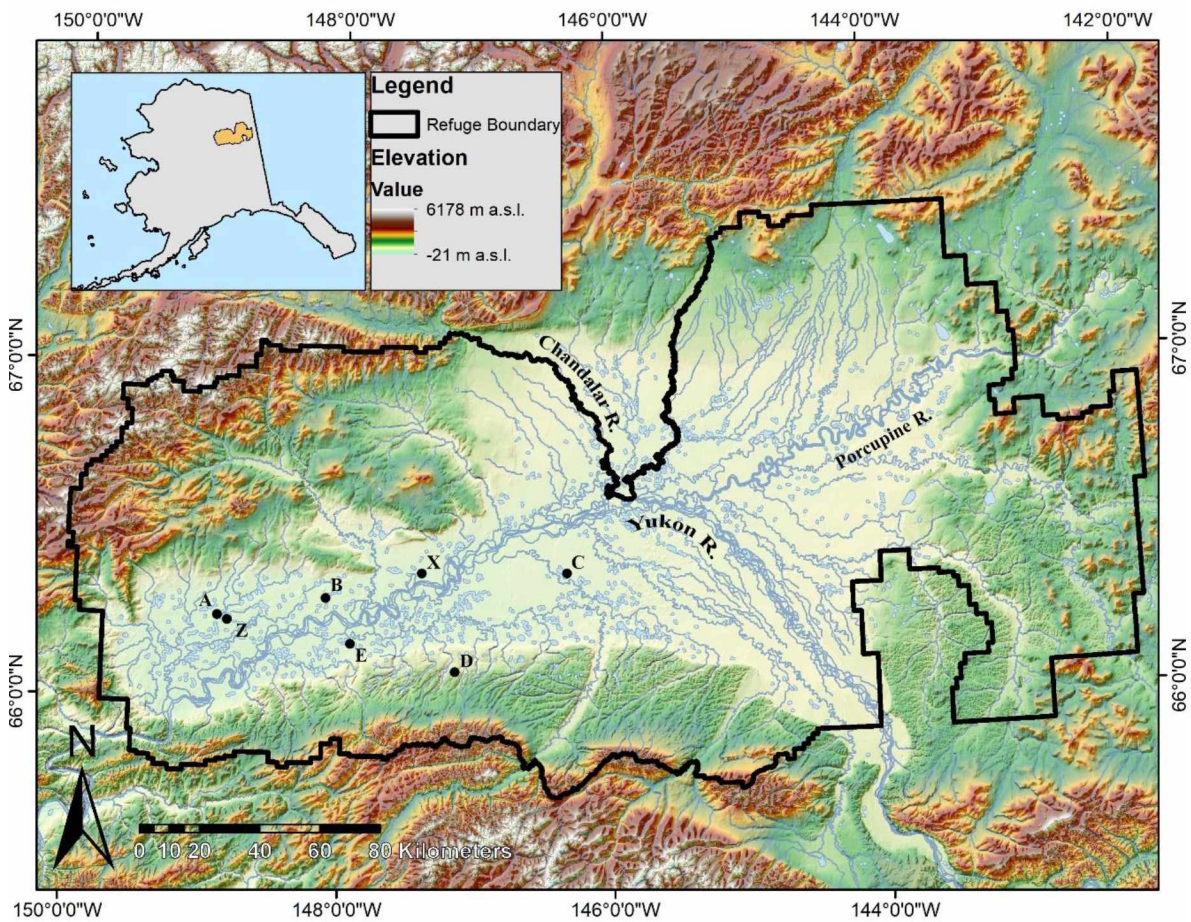
Figure 6. Map of the Yukon Flats National Wildlife Refuge, Alaska. Flight areas labeled, A, B, C, D, E, X, and Z

and Jones, 2003). Due to the shallowness of the lakes, there is little stratification within the water column, with diurnal mixing during summer and most freezing to the sediment during winter, and a lack of permanent fish stock (Heglund and Jones, 2003). The shallow lakes, developed in the complex carbonate-rich alluvial sediments of the basin have highly variable nutrient concentrations, but most water bodies within the Refuge are rich in nutrients, and are either eutrophic or hypereutrophic (Heglund and Jones, 2003). The high nutrient levels of many lakes allow for high populations of phytoplankton and invertebrates (Heglund and Jones, 2003). Moreover, many lakes (~25 %) are slightly brackish (Heglund and Jones, 2003) with the potential of increased salinity concentrations and eutrophication as annual temperatures continue to rise, and evaporation and permafrost degradation increase (Lewis et al., 2015b).

In addition to the abundant lakes and waterways, the Yukon Flats hosts a variety of habitats, with mixed boreal forest dominated by black spruce (*Picea mariana*) and white spruce (*Picea glauca*) covering much of the area. Stands of Alaska birch (*Betula neoalaskana*), and quaking aspen (*Populus tremuloides*) are common, along with willow (*Salix* ssp.) and alder (*Alnus* ssp.) thickets. Graminoid and sedge (*Carex* spp.) grasslands occupy many areas, while emergent plants (*Equisetum* spp., *Typha* spp., *Scirpus* spp.) are found within the wetlands and peripheries of lakes. The abundance and diversity of land cover types, along with the large amount of shallow, nutrient-rich water bodies has made the Yukon Flats an important breeding habitat for waterfowl (Lewis et al., 2015a), with over 100 different species, and an estimated 0.5 to 1.5 million ducks, geese, and swans nesting there annually, including lesser scaup (*Aythya affinis*), white-winged scoters (*Melanitta fusca*), and horned grebes (*Podiceps auratus*) utilizing the area (Heglund, 1994).

17

2.2. HySpex hyperspectral imaging system

The HySpex hyperspectral imaging system, manufactured by Norsk Elektro Optikk (NEO) is configured for airborne acquisition using two sensors connected to a data acquisition unit (DAU) and an inertial measurement unit (IMU). The sensors are pushbroom (or along track) scanners, meaning that a line of detectors is arranged perpendicular to the flight direction of an acquisition platform (Figure 7). As the platform moves forward, the remotely sensed image is built one pixel-line at a time. Both sensors have low stray light levels, low polarization sensitivity, and high signal to noise ratios that allow for imaging highly dynamic scenes.
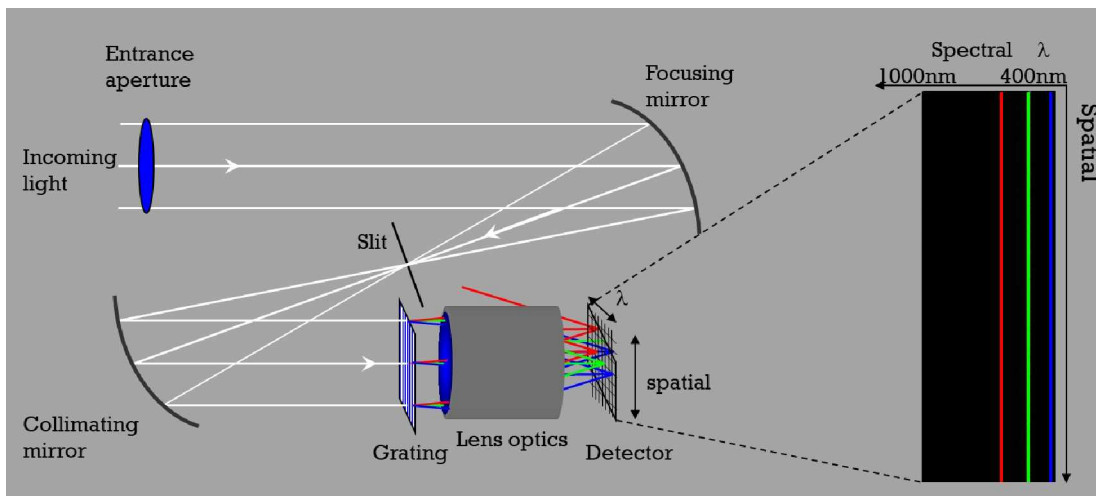
Figure 7. Hyspex pushbroom scanning design. From Norsk Elektro Optikk AS, "HySpex Imaging Spectrometer User Manual."

The VNIR-1800 sensor (Figure 8a) samples spectra in the 400 to 1000 nanometer region, with 182 spectral channels sampling 3.26 nm per channel, with a 16-bit radiometric resolution. It has a 17-degree field of view, with 1800 spatial pixels of 0.16 milliradians across-track by 0.32 milliradians along-track. The SWIR-384 sensor (Figure 8b) samples spectra in the 950 to 2500 nanometer region, with 288 spectral channels sampling 5.45 nm per channel, with a 16-bit radiometric resolution. It has 384 spatial pixels with a spatial resolution of 0.73 milliradians along-

track by 0.73 milliradians cross-track, and a 16-degree field of view. Both sensors were equipped with a field expander optic to allow for increased flight speed at the same altitude, and to cover more ground area for the available flight time. The optics double the pixel field of view (FOV) along and across track, for a VNIR-1800 FOV and SWIR-384 FOV of 32 degrees and 34 degrees, respectively.

The DAU (Figure 8c) is a purpose-built Windows 7 machine, containing an Intel 530 series solid state drive (SSD), 240 gigabyte operating system disk, four 240 gigabyte Intel SSD (510 series) disks, an Xcelera_CL-PX4 framegrabber, an Xcelera_CL-PX8 framegrabber, 32 gigabytes of DDR3 memory, an Intel i7 quad-core processor, and a frequency divider to divide down the frequency for synchronization between multiple HySpex cameras and for event input on navigation systems. It runs the HySpex acquisition and control software, HySpex AIR and provides power to the HySpex sensors. The DAU software is monitored and controlled by the system operator in-air via a retroreflective touch screen (Figure 8d).

The IMU (Figure 8e) is an IMAR iTrace RT-F400 IMU/GPS. Coupled with a GPS receiver antenna (Figure 8g), the IMU provides all kinematic measurements during acquisition as acceleration, angular rate and roll, pitch, and yaw of the aircraft, as well as position and velocity.
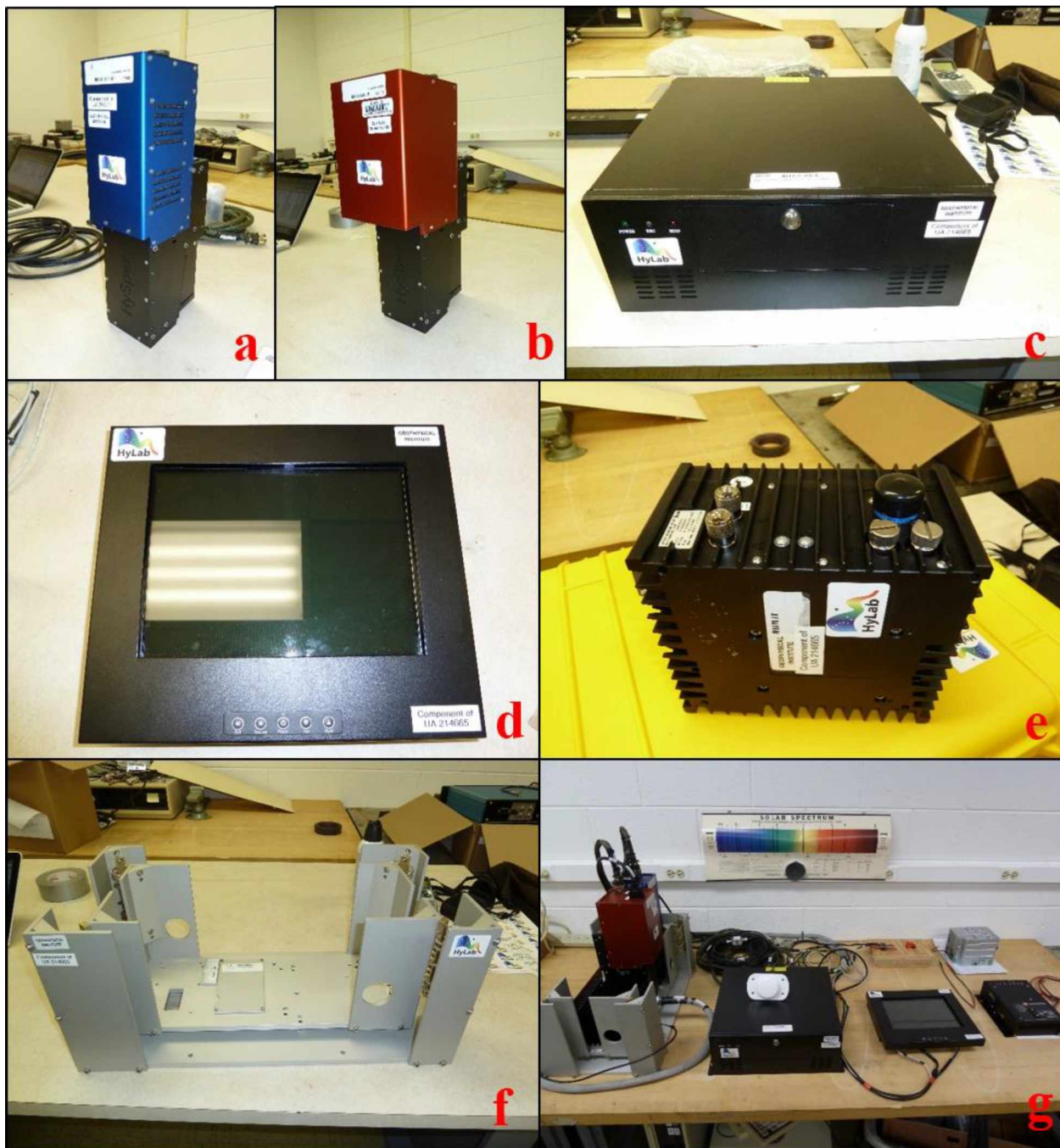
Figure 8. Components of the HySpex system. (a) VNIR-1800; (b) SWIR-384; (c) air data acquisition unit (DAU); (d) iTrace RT-F400 IMU/GPS; (e) transreflective touchscreen; (f) vibration dampening mount; (g) lab setup of the Hyspex system with GPS antenna sitting on DAU, and power system, top right.

2.3 Integration of HySpex into aircraft

A Found Aircraft single-engine Bush Hawk, owned and operated by the US Fish and Wildlife Service (USFWS) served as the acquisition platform for the HySpex system (Figure 9a). The VNIR-1800 and SWIR-384 sensors, along with an IMAR iTrace RT-f400 IMU/GPS (Inertial Measurement Unit / Global Positioning System) unit were attached to a passive vibration dampening mount (Figure 9b) and secured to the aircraft, with the across-track sensor line perpendicular to the aircraft's flight direction (Figure 9c). A GPS antenna connected to the IMU by coaxial cable was mounted to the roof of the aircraft, and X and Y offsets between the antenna and IMU were measured and input into the IMU for the post processing georectification of collected images. Field of view expander lenses were attached to each sensor (Figure 9d), increasing the VNIR-1800 and SWIR-384 across track field-of-view of 17° and 16° to 34° and 32°, respectively. This allowed for maintaining a flight altitude that would capture approximately one-meter ground pixel resolution in the SWIR image, while reducing the number of flight lines needed to cover a selected flight area with the required 40 to 75% side-lap for later mosaicking of the scene.

Finally, the system was controlled in flight by the compact, high-performance data acquisition unit (DAU), connected with a 1 terabyte solid state hard drive and a compact, touch screen flat-panel monitor for in-flight operation and system-monitoring (Figure 9e).

A QUINT-UPS 24-volt/3.4 amp-hour uninterruptible power supply provided power to the HySpex system in flight and was fed by a 12-volt to 24-volt DC converter plugged in to the aircraft's electrical system (see Figure 10 for a complete system diagram). The system was powered and tested prior to flight to ensure reliable operation and an unobstructed view through the aircraft's floor aperture. While performing a ground test acquisition of the HySpex system, a

Figure 9. Commissioning the HySpex system for airborne acquisition. (a) USFWS Found Aircraft Bush Hawk; (b) VNIR-1800, Swir-384, and IMU/GPS units mounted to vibration dampening plate; (c) field of view expander optic attached to VNIR 1800 and SWIR 384 sensors; (d) detail of HySpex sensors in aircraft; (e) overhead view of the system secured and operating in aircraft; (f) testing system visibility through floor aperture of the aircraft.

visible and near-infrared high contrast checkboard was placed below the aircraft aperture and

moved perpendicular to the detector lines of the HySpex sensors to simulate aircraft movement

over ground, and the resulting VNIR and SWIR images were inspected visually to determine that

the view angles of both sensors would be unobstructed by the aircraft fuselage during flight

acquisition (Figure 9e).
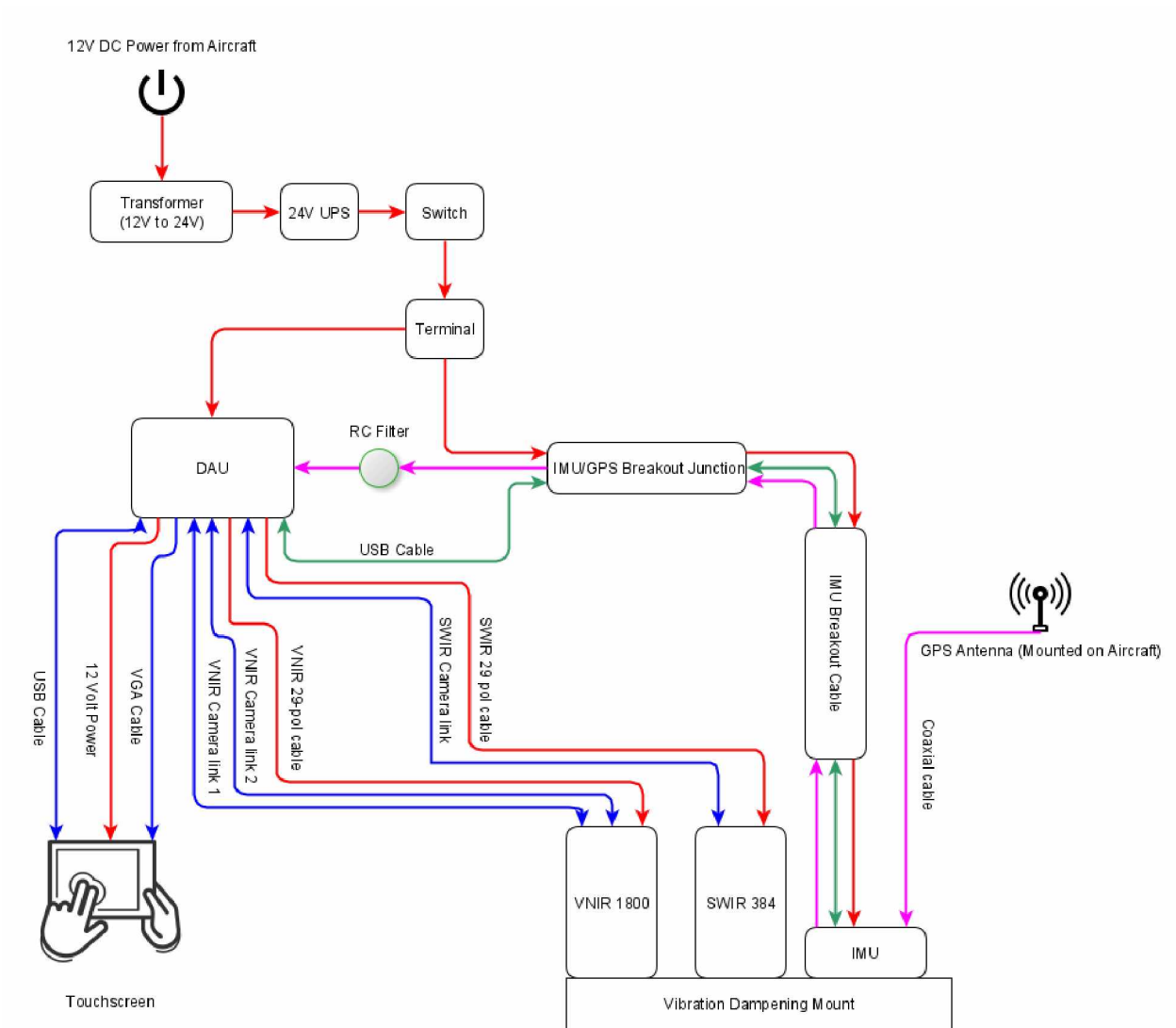
Figure 10. HySpex system diagram for Bush Hawk commission. Power from a 24-volt UPS fed the DAU and IMU units. The DAU was operated via touchscreen and controlled and collected data from the sensors, while providing power to the VNIR and SWIR cameras. Key: Red = power; Blue = Data Cable; Green = IMU data; Pink = GPS data/coaxial cable.

2.4 Flight planning and data acquisition

On September 2nd and 3rd 2015, seven selected areas of around 4 by 5 km from the Yukon Flats National Wildlife Refuge were flown at 1 m spatial resolution using the HySpex VNIR-1800 and SWIR-384 sensors (Figure 12, Figure 13, and Table 1). These seven areas, consisting of a total of 70 flight lines, were chosen because of their different water chemistry, ecological habitat, and for the baseline information that the USFWS had previously collected that were intended to be used for wetland mapping (see Appendix 1 for detailed information about the flight planning). Two flight areas B and C (Figure 12 and Figure 13) were identified by USFWS personnel as "high priority" targets due to their firsthand knowledge of the plant communities in these areas and Refuge management priorities. The target spatial resolution was of 50 cm for the VNIR-1800, and 1 m for the SWIR-384 determined at a flight altitude of 2451 feet above ground level at 165 km·hr^{-1} flight speed. Setting the frameperiod time for each camera was based on Table 2 and Table 3 provided by the system manufacturer, NEO and the maximum frameperiod possible without under-sampling the ground scene was determined by the flight altitude and ground speed used. A 40 % sidelap between flightlines was planned to account for banking of the aircraft during acquisition, and to aid in the georectification process.

Integration time for each camera was determined in flight at each flight area before acquisition of individual flightlines began based on Hyspex time integration tables (Table 2 and Table 3). A test acquisition flightline was flown over the target area, with increasing integration times until at least one spectral band saturated for the relevant ground cover. The integration time was then reduced by roughly 10 % of the saturation value to optimize the data quality for the ground cover type, while still having a margin for variability in reflectance levels throughout the spectral bands.

Flightlines were planned to be flown within two hours before and after solar noon in a direction east to west, or north to south (i.e. acquisition for all flightlines in an area would begin in the east and end in the west) to account for and reduce bidirectional reflectance distribution function (BRDF) effects that are more pronounced in areas of high latitude. An example of the BRDF effect between flightlines in imagery opportunistically collected on September 2, 2015 and flown northeast to southwest is shown in Figure 14.
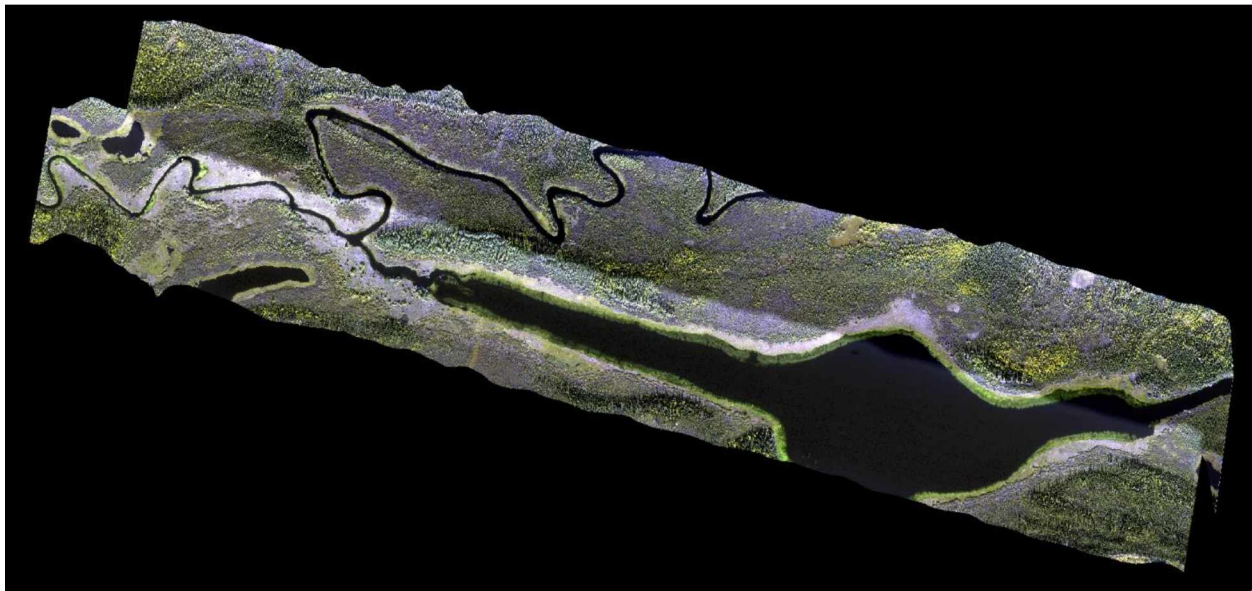
Figure 11. BRDF Effect. Orthomosaic of HySpex imagery in true color showing BRDF effect between two flightlines flown northeast to southwest. Note the flightline at the top of the image is darker for the same ground cover type.
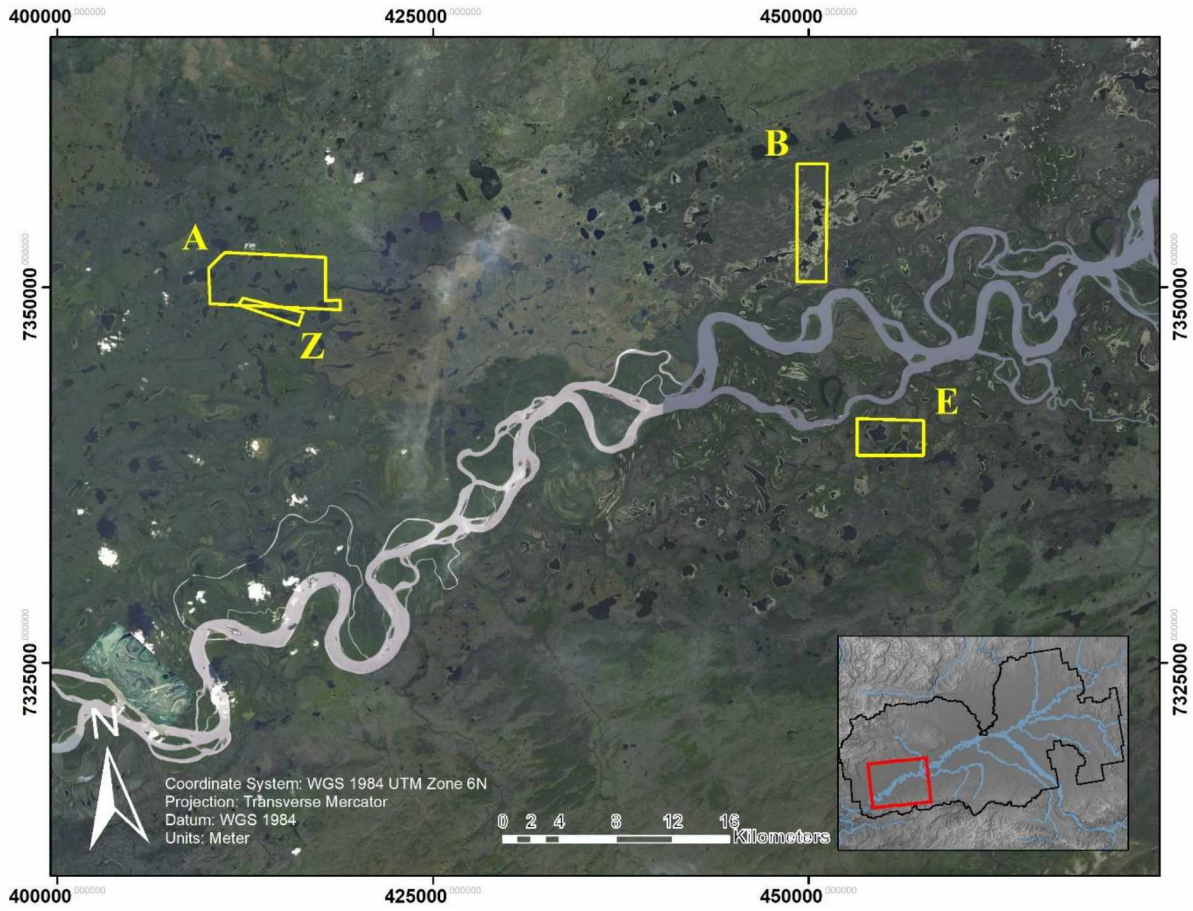
Figure 12. Flight area western detail. Four out of seven flight areas shown, A, B, E, and Z.
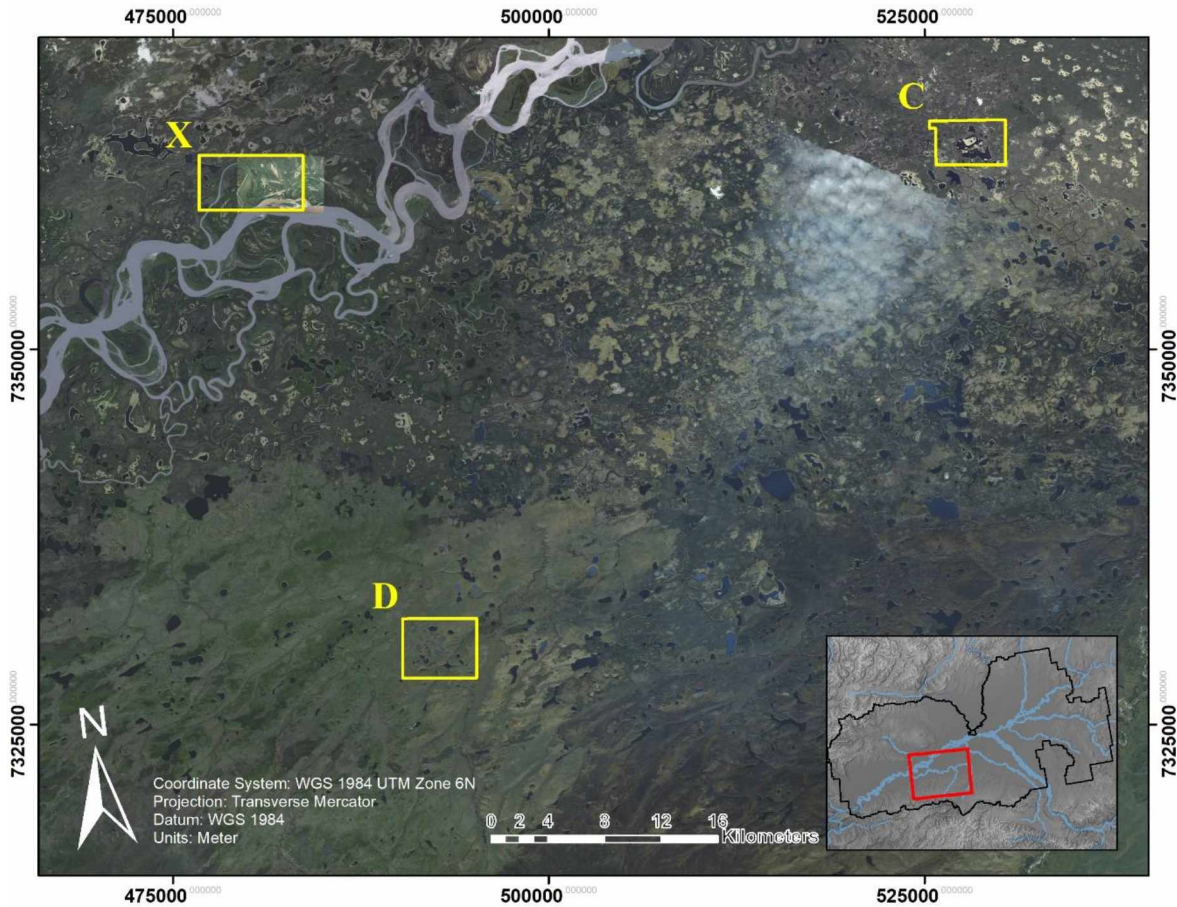
Figure 13. Flight area eastern detail. Three out of seven flight areas shown, C, D, and X.

Raw image files for the VNIR and SWIR sensors and navigational data files from the IMU/GPS that were recorded and stored on the DAU were transferred, post-flight to a processing computer's disk drives for long term storage and subsequent processing.

Table 1. Flight acquisitions in the Yukon Flats National Wildlife Refuge

Flight area	Flight lines acquired	Acquisition Date (MM/DD/YYYY) and start time (in AKDT)	Flight direction	Upper Left UTM-6N coordinates	Lower right UTM-6N coordinates
A	15	09/02/2015 10:52:54	East to West	414028 E 7348316 N	418919 E 7348478 N
B	07	09/02/2015 11:00:00	North to South	450310 E 7353237 N	451075 E 7350357 N
C	11	09/02/2015 15:13:09	East to West	530587 E 7364626 N	530660 E 7362194 N
D	15	09/03/2015 11:11:13	East to West	493652 E 7330049 N	495315 E 7328177 N
E	09	09/03/2015 12:55:02	East to West	454686 E 7340425 N	457682 E 7338826 N
X	02	09/02/2015 12:55:58	Northwest to Southeast	414702 E 7349772 N	416239 E 7347618 N
Z	12	09/03/2015 14:45:36	East to West	480217 E 7362235 N	483791 E 7359278 N

Table 2. Altitude and ground speed vs frame time for SWIR-384 with FOV Expander

☑ FOV Expander

SWIR-384 frame times (ms) for different flight alititudes and ground speeds:

miles/h	km/h	Knots	100	200	300	400	500	600	700	800	900	1000	1100	1200	1300	1400	1500	1600	1700	1800	1900	2000	2500	3000
	Altitude (ft):		328	656	984	1312	1640	1969	2297	2625	2953	3281	3609	3937	4265	4593	4921	5249	5577	5906	6234	6562	8202	9843
													FRAME TIME (ms)												
115,08	185,20	100	2,84	5,68	8,51	11,35	14,19	17,03	19,87	22,70	25,54	28,38	31,22	34,06	36,89	39,73	42,57	45,41	48,25	51,08	53,92	56,76	70,95	85,14
120,832	194,46	105	2,70	5,41	8,11	10,81	13,51	16,22	18,92	21,62	24,33	27,03	29,73	32,43	35,14	37,84	40,54	43,25	45,95	48,65	51,35	54,06	67,57	81,09
126,59	203,72	110	2,58	5,16	7,74	10,32	12,90	15,48	18,06	20,64	23,22	25,80	28,38	30,96	33,54	36,12	38,70	41,28	43,86	46,44	49,02	51,60	64,50	77,40
132,34	212,98	115	2,47	4,94	7,40	9,87	12,34	14,81	17,27	19,74	22,21	24,68	27,15	29,61	32,08	34,55	37,02	39,49	41,95	44,42	46,89	49,36	61,70	74,04
138,09	222,24	120	2,37	4,73	7,10	9,46	11,83	14,19	16,56	18,92	21,29	23,65	26,02	28,38	30,75	33,11	35,48	37,84	40,21	42,57	44,94	47,30	59,13	70,95
143,848	231,5	125	2,27	4,54	6,81	9,08	11,35	13,62	15,89	18,16	20,43	22,70	24,97	27,24	29,52	31,79	34,06	36,33	38,60	40,87	43,14	45,41	56,76	68,11
149,60	240,76	130	2,18	4,37	6,55	8,73	10,92	13,10	15,28	17,46	19,65	21,83	24,01	26,20	28,38	30,56	32,75	34,93	37,11	39,30	41,48	43,66	54,58	65,49
155,356	250,02	135	2,10	4,20	6,31	8,41	10,51	12,61	14,72	16,82	18,92	21,02	23,12	25,23	27,33	29,43	31,53	33,64	35,74	37,84	39,94	42,04	52,56	63,07
161,11	259,28	140	2,03	4,05	6,08	8,11	10,14	12,16	14,19	16,22	18,24	20,27	22,30	24,33	26,35	28,38	30,41	32,43	34,46	36,49	38,52	40,54	50,68	60,81
166,86	268,54	145	1,96	3,91	5,87	7,83	9,79	11,74	13,70	15,66	17,62	19,57	21,53	23,49	25,44	27,40	29,36	31,32	33,27	35,23	37,19	39,15	48,93	58,72
172,62	277,80	150	1,89	3,78	5,68	7,57	9,46	11,35	13,24	15,14	17,03	18,92	20,81	22,70	24,60	26,49	28,38	30,27	32,16	34,06	35,95	37,84	47,30	56,76
178,37	287,06	155	1,83	3,66	5,49	7,32	9,15	10,99	12,82	14,65	16,48	18,31	20,14	21,97	23,80	25,63	27,46	29,30	31,13	32,96	34,79	36,62	45,77	54,93
184,13	296,32	160	1,77	3,55	5,32	7,10	8,87	10,64	12,42	14,19	15,96	17,74	19,51	21,29	23,06	24,83	26,61	28,38	30,15	31,93	33,70	35,48	44,34	53,21
189,88	305,58	165	1,72	3,44	5,16	6,88	8,60	10,32	12,04	13,76	15,48	17,20	18,92	20,64	22,36	24,08	25,80	27,52	29,24	30,96	32,68	34,40	43,00	51,60
195,63	314,84	170	1,67	3,34	5,01	6,68	8,35	10,02	11,69	13,36	15,02	16,69	18,36	20,03	21,70	23,37	25,04	26,71	28,38	30,05	31,72	33,39	41,74	50,08
201,39	324,10	175	1,62	3,24	4,87	6,49	8,11	9,73	11,35	12,97	14,60	16,22	17,84	19,46	21,08	22,70	24,33	25,95	27,57	29,19	30,81	32,43	40,54	48,65
207,14	333,36	180	1,58	3,15	4,73	6,31	7,88	9,46	11,04	12,61	14,19	15,77	17,34	18,92	20,50	22,07	23,65	25,23	26,80	28,38	29,96	31,53	39,42	47,30
212,89	342,62	185	1,53	3,07	4,60	6,14	7,67	9,20	10,74	12,27	13,81	15,34	16,87	18,41	19,94	21,48	23,01	24,54	26,08	27,61	29,15	30,68	38,35	46,02
218,65	351,88	190	1,49	2,99	4,48	5,97	7,47	8,96	10,46	11,95	13,44	14,94	16,43	17,92	19,42	20,91	22,41	23,90	25,39	26,89	28,38	29,87	37,34	44,81
224,40	361,14	195	1,46	2,91	4,37	5,82	7,28	8,73	10,19	11,64	13,10	14,55	16,01	17,46	18,92	20,38	21,83	23,29	24,74	26,20	27,65	29,11	36,38	43,66
230,16	370,40	200	1,42	2,84	4,26	5,68	7,10	8,51	9,93	11,35	12,77	14,19	15,61	17,03	18,45	19,87	21,29	22,70	24,12	25,54	26,96	28,38	35,48	42,57
235,91	379,66	205	1,38	2,77	4,15	5,54	6,92	8,31	9,69	11,08	12,46	13,84	15,23	16,61	18,00	19,38	20,77	22,15	23,53	24,92	26,30	27,69	34,61	41,53
241,66	388,92	210	1,35	2,70	4,05	5,41	6,76	8,11	9,46	10,81	12,16	13,51	14,87	16,22	17,57	18,92	20,27	21,62	22,97	24,33	25,68	27,03	33,79	40,54
247,42	398,18	215	1,32	2,64	3,96	5,28	6,60	7,92	9,24	10,56	11,88	13,20	14,52	15,84	17,16	18,48	19,80	21,12	22,44	23,76	25,08	26,40	33,00	39,60
253,17	407,44	220	1,29	2,58	3,87	5,16	6,45	7,74	9,03	10,32	11,61	12,90	14,19	15,48	16,77	18,06	19,35	20,64	21,93	23,22	24,51	25,80	32,25	38,70
258,93	416,70	225	1,26	2,52	3,78	5,05	6,31	7,57	8,83	10,09	11,35	12,61	13,87	15,14	16,40	17,66	18,92	20,18	21,44	22,70	23,97	25,23	31,53	37,84
264,68	425,96	230	1,23	2,47	3,70	4,94	6,17	7,40	8,64	9,87	11,11	12,34	13,57	14,81	16,04	17,27	18,51	19,74	20,98	22,21	23,44	24,68	30,85	37,02
270,43	435,22	235	1,21	2,42	3,62	4,83	6,04	7,25	8,45	9,66	10,87	12,08	13,28	14,49	15,70	16,91	18,11	19,32	20,53	21,74	22,95	24,15	30,19	36,23
276,19	444,48	240	1,18	2,37	3,55	4,73	5,91	7,10	8,28	9,46	10,64	11,83	13,01	14,19	15,37	16,56	17,74	18,92	20,10	21,29	22,47	23,65	29,56	35,48
281,94	453,74	245	1,16	2,32	3,48	4,63	5,79	6,95	8,11	9,27	10,43	11,58	12,74	13,90	15,06	16,22	17,38	18,53	19,69	20,85	22,01	23,17	28,96	34,75
287,70	463,00	250	1,14	2,27	3,41	4,54	5,68	6,81	7,95	9,08	10,22	11,35	12,49	13,62	14,76	15,89	17,03	18,16	19,30	20,43	21,57	22,70	28,38	34,06
293,45	472,26	255	1,11	2,23	3,34	4,45	5,56	6,68	7,79	8,90	10,02	11,13	12,24	13,36	14,47	15,58	16,69	17,81	18,92	20,03	21,15	22,26	27,82	33,39
230,16	370,40	200	1,42	2,84	4,26	5,68	7,10	8,51	9,93	11,35	12,77	14,19	15,61	17,03	18,45	19,87	21,29	22,70	24,12	25,54	26,96	28,38	35,48	42,57
Ground sampling distance(m):			0,15	0,29	0,44	0,58	0,73	0,88	1,02	1,17	1,31	1,46	1,61	1,75	1,90	2,04	2,19	2,34	2,48	2,63	2,77	2,92	3,65	4,38

SWIR-384   FOV Expander

Black frame times are suitable for max frame rate
Blue frames times are suitable only for binning modes
Red values indicate that the combination of altitude and speed will give sub-sampled images.

Spalt   0,3735 µm
Read-out t   110 µs

Binning	Max frame rate (Hz)	max int
1x binning	400	0,00250
2x	400	0,00250
3x	400	0,00250

Table 3. Altitude and ground speed vs frame time for VNIR-1800 with FOV expander

☑ FOV Expander

VNIR-1800 frame times (ms) for different flight altitudes and ground speeds:

miles/h	km/h	Knots	100	200	300	400	500	600	700	800	900	1000	1100	1200	1300	1400	1500	1600	1700	1800	1900	2000	2500	3000
		Altitude (ft):	328	656	984	1312	1640	1969	2297	2625	2953	3281	3609	3937	4265	4593	4921	5249	5577	5906	6234	6562	8202	9843
miles/h	km/h	Knots											FRAME TIME (ms)											
115,08	185,20	100	1,24	2,49	3,73	4,98	6,22	7,46	8,71	9,95	11,20	12,44	13,68	14,93	16,17	17,42	18,66	19,90	21,15	22,39	23,64	24,88	31,10	37,32
120,832	194,46	105	1,18	2,37	3,55	4,74	5,92	7,11	8,29	9,48	10,66	11,85	13,03	14,22	15,40	16,59	17,77	18,96	20,14	21,33	22,51	23,70	29,62	35,54
126,59	203,72	110	1,13	2,26	3,39	4,52	5,65	6,79	7,92	9,05	10,18	11,31	12,44	13,57	14,70	15,83	16,96	18,10	19,23	20,36	21,49	22,62	28,27	33,93
132,34	212,98	115	1,08	2,16	3,25	4,33	5,41	6,49	7,57	8,65	9,74	10,82	11,90	12,98	14,06	15,15	16,23	17,31	18,39	19,47	20,55	21,64	27,04	32,45
138,09	222,24	120	1,04	2,07	3,11	4,15	5,18	6,22	7,26	8,29	9,33	10,37	11,40	12,44	13,48	14,51	15,55	16,59	17,62	18,66	19,70	20,73	25,92	31,10
143,848	231,5	125	1,00	1,99	2,99	3,98	4,98	5,97	6,97	7,96	8,96	9,95	10,95	11,94	12,94	13,93	14,93	15,92	16,92	17,91	18,91	19,90	24,88	29,86
149,60	240,76	130	0,96	1,91	2,87	3,83	4,78	5,74	6,70	7,66	8,61	9,57	10,53	11,48	12,44	13,40	14,35	15,31	16,27	17,23	18,18	19,14	23,92	28,71
155,356	250,02	135	0,92	1,84	2,76	3,69	4,61	5,53	6,45	7,37	8,29	9,22	10,14	11,06	11,98	12,90	13,82	14,74	15,67	16,59	17,51	18,43	23,04	27,65
161,11	259,28	140	0,89	1,78	2,67	3,55	4,44	5,33	6,22	7,11	8,00	8,89	9,77	10,66	11,55	12,44	13,33	14,22	15,11	16,00	16,88	17,77	22,22	26,66
166,86	268,54	145	0,86	1,72	2,57	3,43	4,29	5,15	6,01	6,86	7,72	8,58	9,44	10,30	11,15	12,01	12,87	13,73	14,59	15,44	16,30	17,16	21,45	25,74
172,62	277,80	150	0,83	1,66	2,49	3,32	4,15	4,98	5,81	6,63	7,46	8,29	9,12	9,95	10,78	11,61	12,44	13,27	14,10	14,93	15,76	16,59	20,73	24,88
178,37	287,06	155	0,80	1,61	2,41	3,21	4,01	4,82	5,62	6,42	7,22	8,03	8,83	9,63	10,43	11,24	12,04	12,84	13,64	14,45	15,25	16,05	20,07	24,08
184,13	296,32	160	0,78	1,56	2,33	3,11	3,89	4,67	5,44	6,22	7,00	7,78	8,55	9,33	10,11	10,89	11,66	12,44	13,22	14,00	14,77	15,55	19,44	23,33
189,88	305,58	165	0,75	1,51	2,26	3,02	3,77	4,52	5,28	6,03	6,79	7,54	8,29	9,05	9,80	10,56	11,31	12,06	12,82	13,57	14,33	15,08	18,85	22,62
195,63	314,84	170	0,73	1,46	2,20	2,93	3,66	4,39	5,12	5,85	6,59	7,32	8,05	8,78	9,51	10,25	10,98	11,71	12,44	13,17	13,90	14,64	18,30	21,95
201,39	324,10	175	0,71	1,42	2,13	2,84	3,55	4,27	4,98	5,69	6,40	7,11	7,82	8,53	9,24	9,95	10,66	11,37	12,09	12,80	13,51	14,22	17,77	21,33
207,14	333,36	180	0,69	1,38	2,07	2,76	3,46	4,15	4,84	5,53	6,22	6,91	7,60	8,29	8,98	9,68	10,37	11,06	11,75	12,44	13,13	13,82	17,28	20,73
212,89	342,62	185	0,67	1,34	2,02	2,69	3,36	4,03	4,71	5,38	6,05	6,72	7,40	8,07	8,74	9,41	10,09	10,76	11,43	12,10	12,78	13,45	16,81	20,17
218,65	351,88	190	0,65	1,31	1,96	2,62	3,27	3,93	4,58	5,24	5,89	6,55	7,20	7,86	8,51	9,17	9,82	10,48	11,13	11,79	12,44	13,10	16,37	19,64
224,40	361,14	195	0,64	1,28	1,91	2,55	3,19	3,83	4,47	5,10	5,74	6,38	7,02	7,66	8,29	8,93	9,57	10,21	10,85	11,48	12,12	12,76	15,95	19,14
230,16	370,40	200	0,62	1,24	1,87	2,49	3,11	3,73	4,35	4,98	5,60	6,22	6,84	7,46	8,09	8,71	9,33	9,95	10,57	11,20	11,82	12,44	15,55	18,66
235,91	379,66	205	0,61	1,21	1,82	2,43	3,03	3,64	4,25	4,85	5,46	6,07	6,68	7,28	7,89	8,50	9,10	9,71	10,32	10,92	11,53	12,14	15,17	18,21
241,66	388,92	210	0,59	1,18	1,78	2,37	2,96	3,55	4,15	4,74	5,33	5,92	6,52	7,11	7,70	8,29	8,89	9,48	10,07	10,66	11,26	11,85	14,81	17,77
247,42	398,18	215	0,58	1,16	1,74	2,31	2,89	3,47	4,05	4,63	5,21	5,79	6,36	6,94	7,52	8,10	8,68	9,26	9,84	10,42	10,99	11,57	14,47	17,36
253,17	407,44	220	0,57	1,13	1,70	2,26	2,83	3,39	3,96	4,52	5,09	5,65	6,22	6,79	7,35	7,92	8,48	9,05	9,61	10,18	10,74	11,31	14,14	16,96
258,93	416,70	225	0,55	1,11	1,66	2,21	2,76	3,32	3,87	4,42	4,98	5,53	6,08	6,63	7,19	7,74	8,29	8,85	9,40	9,95	10,51	11,06	13,82	16,59
264,68	425,96	230	0,54	1,08	1,62	2,16	2,70	3,25	3,79	4,33	4,87	5,41	5,95	6,49	7,03	7,57	8,11	8,65	9,20	9,74	10,28	10,82	13,52	16,23
270,43	435,22	235	0,53	1,06	1,59	2,12	2,65	3,18	3,71	4,24	4,76	5,29	5,82	6,35	6,88	7,41	7,94	8,47	9,00	9,53	10,06	10,59	13,23	15,88
276,19	444,48	240	0,52	1,04	1,56	2,07	2,59	3,11	3,63	4,15	4,67	5,18	5,70	6,22	6,74	7,26	7,78	8,29	8,81	9,33	9,85	10,37	12,96	15,55
281,94	453,74	245	0,51	1,02	1,52	2,03	2,54	3,05	3,55	4,06	4,57	5,08	5,59	6,09	6,60	7,11	7,62	8,12	8,63	9,14	9,65	10,16	12,69	15,23
287,70	463,00	250	0,50	1,00	1,49	1,99	2,49	2,99	3,48	3,98	4,48	4,98	5,47	5,97	6,47	6,97	7,46	7,96	8,46	8,96	9,45	9,95	12,44	14,93
293,45	472,26	255	0,49	0,98	1,46	1,95	2,44	2,93	3,42	3,90	4,39	4,88	5,37	5,85	6,34	6,83	7,32	7,81	8,29	8,78	9,27	9,76	12,20	14,64
230,16	370,40	200	0,62	1,24	1,87	2,49	3,11	3,73	4,35	4,98	5,60	6,22	6,84	7,46	8,09	8,71	9,33	9,95	10,57	11,20	11,82	12,44	15,55	18,66
		Ground sampling distance(m):	0,06	0,13	0,19	0,26	0,32	0,38	0,45	0,51	0,58	0,64	0,70	0,77	0,83	0,90	0,96	1,02	1,09	1,15	1,22	1,28	1,60	1,92

VNIR-1800   FOV Expander

Black frame times are suitable for max frame rate
Blue frames times are suitable only for binning modes
Red values indicate that the combination of altitude and speed will give sub-sampled images.

Spalt   0,3735 µm
Read-out t   110 µs

Binning	Max frame rate (Hz)	max int
1x binning	270	0,00381
2x	270	0,00381
3x	270	0,00381

3. Data Processing

A considerable amount of preprocessing and data storage is required to generate hyperspectral surface reflectance image products that are suitable for analysis from raw imagery. The HySpex data processing chain used here was originally developed by the German Space Agency (DLR) and was adapted by Dr. Marcel Buchhorn to meet the challenges of hyperspectral imaging at high latitudes organized in four processing steps (see Appendix 2 for further details). As a brief summary, the processing method takes raw imagery collected simultaneously from the two HySpex cameras as well as positional and navigational data collected during flight, and produces robust, geo-registered, surface radiance and reflectance products. In addition to the standard geometric and radiometric corrections, processing workflows were also established for specialized corrections to minimize the effects of BRDF. As said before, BRDF effects are particularly prominent in scenes of high latitude regions, such as the Yukon Flats. The full preprocessing chain is shown below in Appendix II.

3.1 Raw images to at-sensor radiance images

The 16-bit raw integer value data acquired per each flight line was converted to at-sensor radiance value imagery with the "HySpex RAD" software provided by NEO in three steps. A 32-bit float, band sequential interleaved (bsq) file type was selected as output for subsequent processing. During recording, raw image data are stored in a binary file which contains a header with metadata about the image, including RE[i,j], QE[i,j], SF, BG[i,j], dw, A, W and 1 [i], as detailed below.

The first step involves the image acquisition in the raw VNIR and SWIR file format. For each flight line this information was recorded on the DAU during image acquisition in 16-bit digital number (DN) format (*_raw.hyspex) following:

$$DN[i,j] = Ni[i,j] \cdot QE[i] \cdot RE[i,j] \cdot BG[i,j] \qquad \text{(Eq. 1)}$$

where, i is the spectral band number, j is spatial pixel number, DN is the digital numbers stored in the *.hyspex raw data file (from 0 to 65535), N_i is the number of incoming photons corresponding to spatial picture, j and band, i during the integration time t, QE is the quantum efficiency (photoelectron to photon ratio) of the total system, including optics and detector for band i, SF is a scaling factor expressing DN per photoelectron (scaling factor is determined during radiometric calibration of the instrument), and BG is background matrix.

Raw data was then converted to real time calibrated data (*corr_hyspex), CN, using the relationship between real-time calibrated DN values and the incoming light that can be expressed as:

$$CN[i,j] = \frac{DN[i,j] - BG[i,j]}{RE[i,j]} \cdot dw \qquad \text{(Eq. 2)}$$

Finally, at-sensor absolute radiance in $W \cdot m^{-2} \cdot sr^{-1} \cdot nm^{-1}$ was computed as follows:

$$LN[,j] = \frac{CN[i,j] \cdot h \cdot c \cdot SL}{QE[i] \cdot SF \cdot dw \cdot t \cdot A \cdot W \cdot Dl[i] \cdot l[i]} \qquad \text{(Eq. 3)}$$

where, t is the integration time, h is the Planck constant, c is the speed of light, A is the area of the light entrance aperture, Ω is the solid angle of a single pixel (i.e. the steradian of a pixel, or the amount of the field of view from the particular point that a single pixel covers), $\Delta\lambda$ is the spectral sampling of the camera in nanometers (i.e. the spectral resolution), λ is the wavelength in nanometers, and SL is the scaling factor (determined during calibration).

More information about the DN to at-sensor radiance can be found at (Norsk Elektro Optikk, 2014).

3.2. Orthorectification

Orthorectification is a process that removes the effects of image perspective and topographic relief, creating a planimetrically correct image with each pixel representing a map projected coordinate on the Earth's surface. This process is performed for each flightline in a flight area on both the VNIR and SWIR at-sensor radiance images. Inputs are the at-sensor radiance flightline image (either VNIR or SWIR file), a sensor model for either VNIR or SWIR image, a digital elevation model (DEM) of the flightline area, a navigational information file for the flightline (IMU/GPS data), and a boresight calibration offset value file.
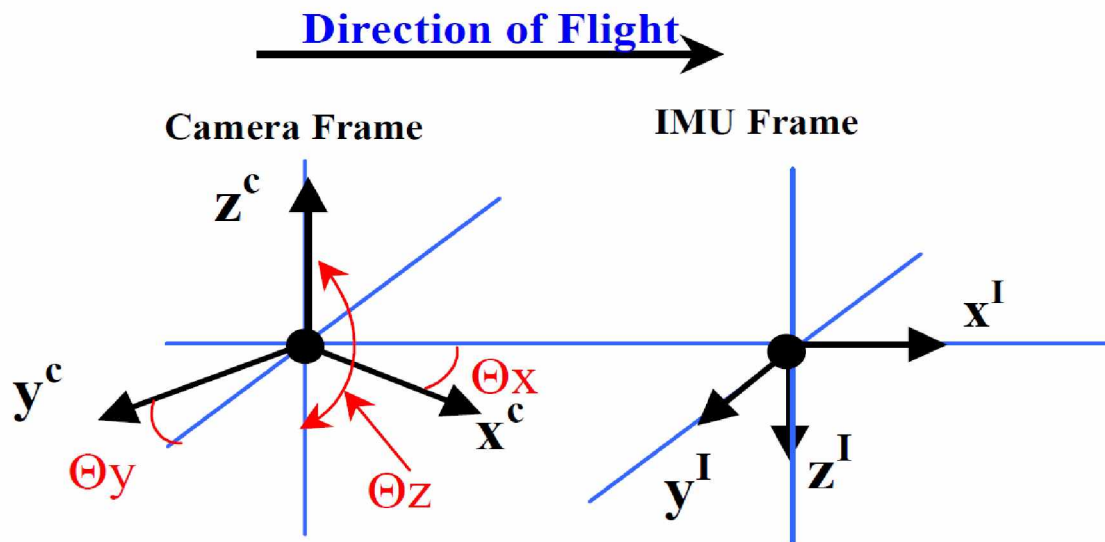

Figure 14. Camera/IMU boresight. Figure from Mostafa, Mohamed MR. "Boresight Calibration of Integrated Inertial/Camera Systems." In Proceedings of the International Symposium on Kinematic Systems in Geodesy, Geomatics and Navigation (KIS 2001), Banff, AB, Canada, 5–8, 2001.

33

During image acquisition, the IMU/GPS records flight-attitude (as acceleration, angular rate and roll / pitch / yaw of the aircraft), location and height (x, y and z coordinates), and time for each frame of a HySpex raw image and writes this data to navigation files generated for a flight area. To accurately translate this navigational data collected by the IMU to the camera frames during the orthorectification process, VNIR and SWIR flight line images were acquired over the University of Alaska Fairbanks campus, with the intent of performing a boresight calibration (see Figure 15). Boresight calibration accounts for misalignment of the physical mounting angles (Θx, Θy, Θz) between the IMU and the optical center of the VNIR-1800 and SWIR-384 camera frames of reference (Figure 14). Ground control points with high GPS accuracy were found in this collected image and used for aerotriangluation to determine the image attitude with respect to a local mapping frame, and compared to the IMU-derived attitude matrix to derive the boresight matrix. This process generated a boresight offset file which was applied during georectification to correct for the angular misalignment between the frames of reference of the IMU and the cameras.

Orthorectification and geocoding of VNIR and SWIR at-sensor radiance flightline files was performed with the ReSe Applications software, PARGE. PARGE reconstructs the scanning geometry for each image pixel using position and attitude of the airplane in conjunction with terrain elevation data (Figure 16). Using the custom software, "HySpex NAV" provided by NEO the navigation files generated by the IMU/GPS for a flight area were subdivided into discreet flightline files that hold the pertinent navigation information used by PARGE for flightline orthorectification. A subset and resampled portion of the 90 m resolution Global Land Survey Digital Elevation Model (GLSDEM) (source for this data set was the Global Land Cover Facility, www.landcover.org) was used for terrain elevation data input and resampled by PARGE to the final spatial resolution of the hyperspectral imagery. Orthorectification of each at-sensor radiance

flightline image for VNIR and SWIR was performed by inputting the corresponding VNIR or SWIR flightline navigation file, a sensor model file generated during system calibration, boresight calibration offsets, and DEM of the flight area into PARGE. Outputs required for later processing steps were VNIR and SWIR flightline orthoimage files, and corresponding VNIR or SWIR scan angle files. Both SWIR and VNIR images were resampled to 1m pixel resolution during orthorectification for subsequent band layer stacking of both images.

Orthorectification accuracy was evaluated in ENVI 5.3 by performing an automatic image to image registration between VNIR band 171 (954.6630 nm λ) and SWIR band 2 (954.6616 nm λ) flightline orthoimages. One hundred tie points were generated between corresponding pixels of the two images and their root mean square error (RMSE) evaluated. A RMSE of less than 0.5, indicating sub-pixel accuracy between tie points was deemed satisfactory.
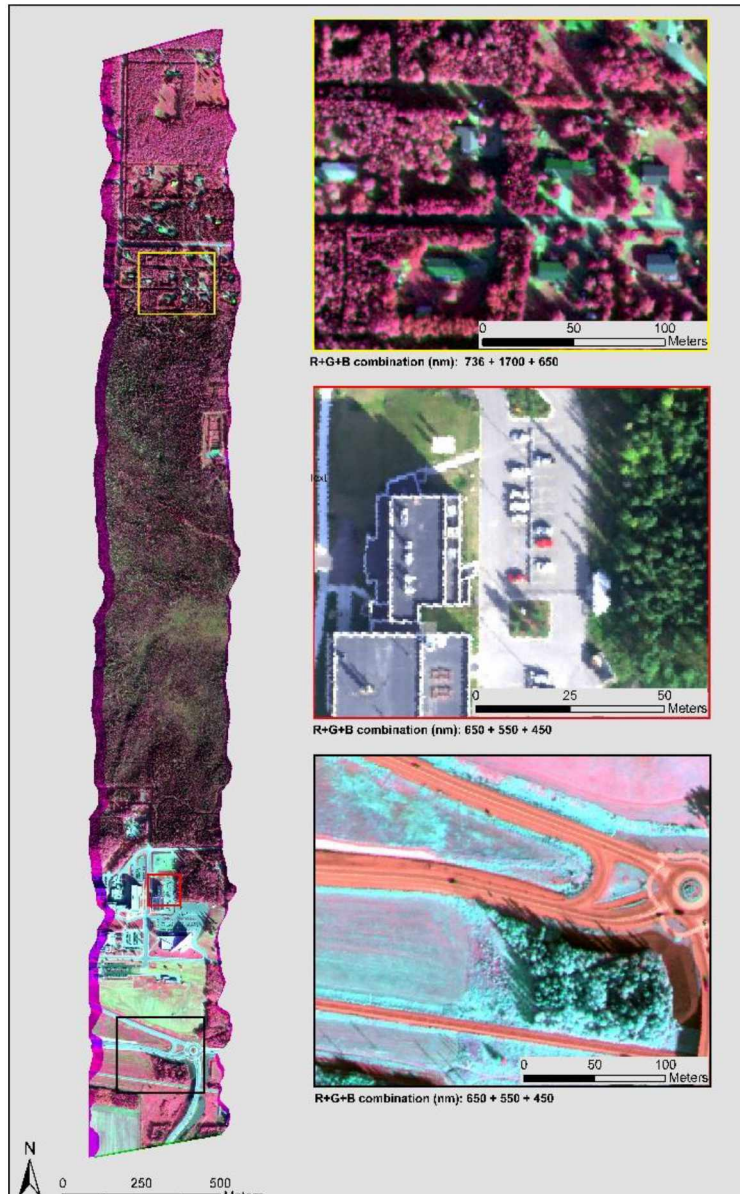
Figure 15. Boresight Calibration. Flight line used at UAF for the boresight calibration of VNIR and SWIR cameras on September 2nd 2015. Ground control points were found in this image and then translated to the boresight calibration process to geometrically align both cameras.
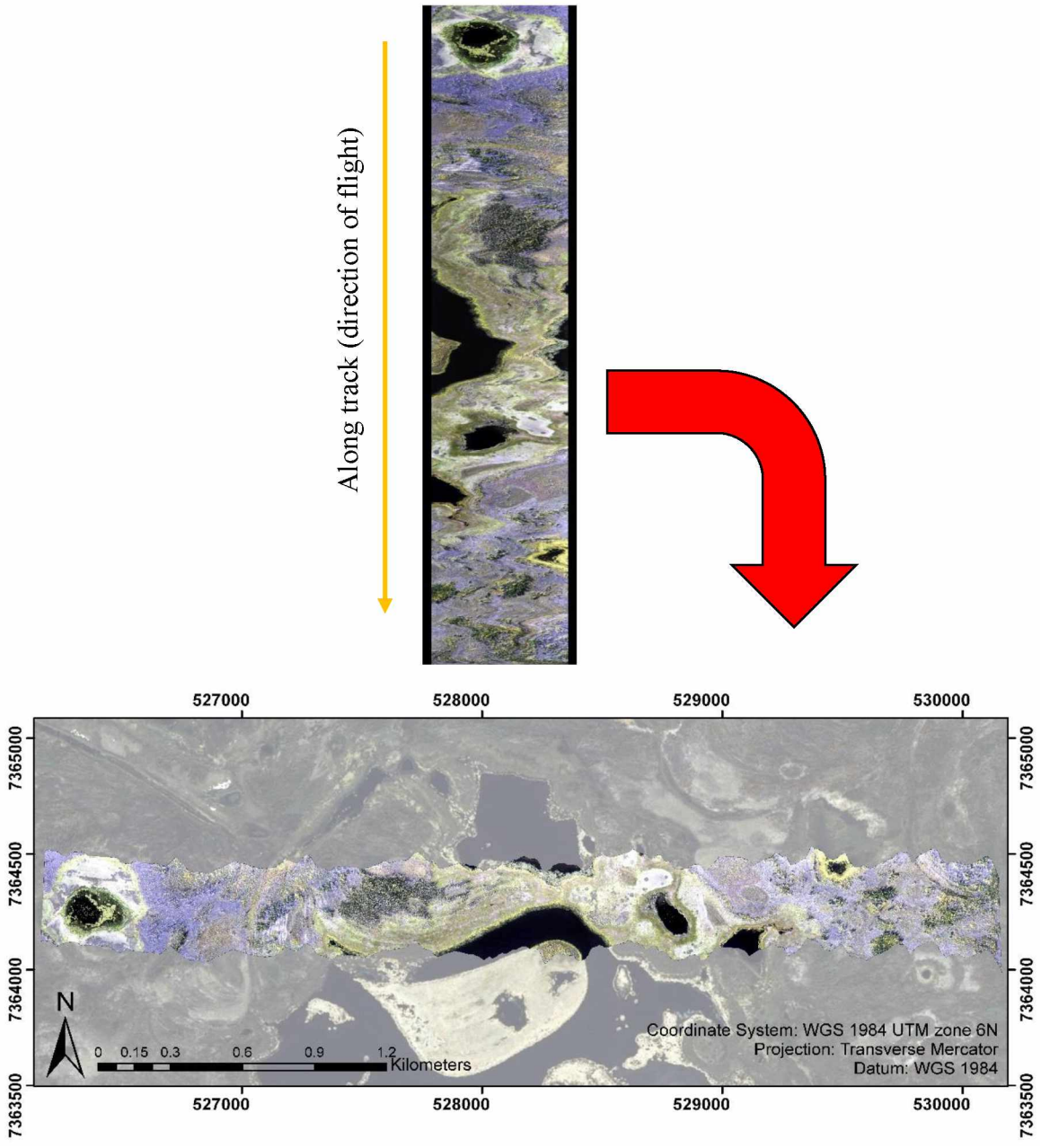
Figure 16. Orthorectification. At-sensor radiance VNIR flightline image (top) orthorectified into projected coordinate system image (bottom), shown here overlaid on an existing orthophoto of the area (Orthophoto from UAF GINA Best Data Layer)

3.3 Layer stacking VNIR and SWIR orthoimages for flightline hypercubes

Following orthorectification, the SWIR image was layer stacked onto the VNIR image in ENVI 5.3, omitting redundant spectral bands between the two sensors to create a hypercube flightline image that encompasses the full 400 nm to 2500 nm spectrum of the HySpex system (Figure 17). Any data from the VNIR or SWIR image that did not spatially overlap due to the differing spatial pixel sizes between the two sensors was masked out following layer-stacking. VNIR and SWIR scan angle files output by PARGE during the orthorectification process were also layer-stacked, and non-overlapping VNIR and SWIR data was similarly masked out. VNIR and SWIR flightline hypercube orthoimage metadata as well as the layer-stacked VNIR and SWIR scan angle file metadata was maintained through the layer-stacking process by manually copying necessary fields to the new hypercube and scan angle metadata files.
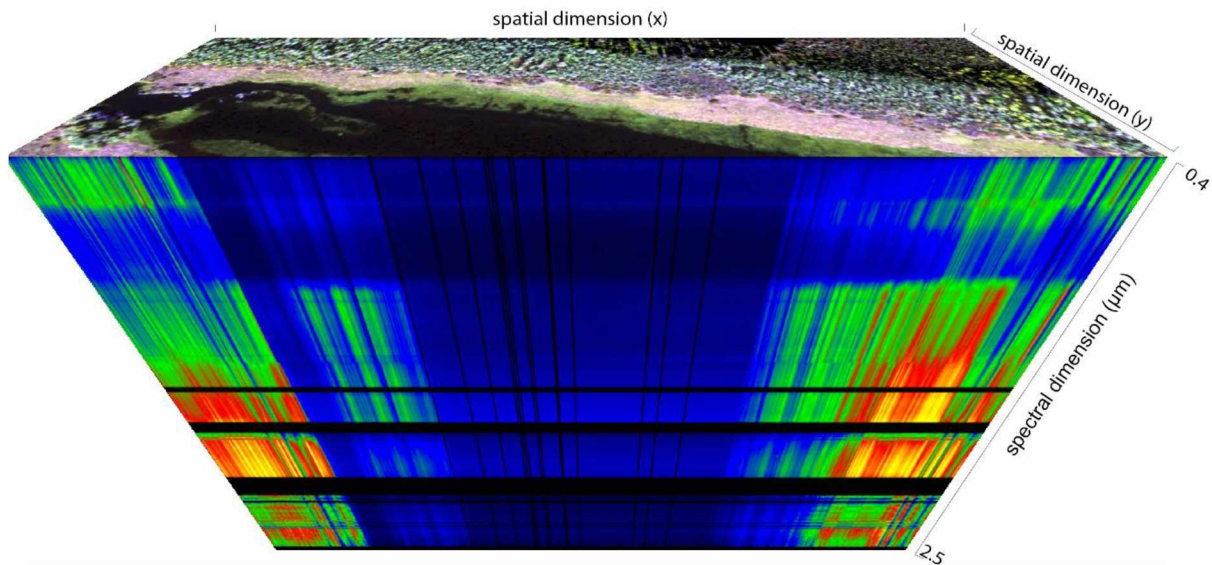

Figure 17. Hypercube. A flightline supercube with spatial dimensions, x and y (in m), and spectral dimension (in μm). Each pixel in the flightline has a corresponding spectral signal from 0.4 to 2.5 micrometers. Dark horizontal regions in the spectral dimension are masked out water absorption bands.

3.4. Radiometric correction

Following generation of an orthorectified flight line hypercube, a radiometric correction is applied though the ReSe Applications ATCOR-4 software, ensuring coherent radiometry between each flight line. The ATCOR software series perform both atmospheric and topographic corrections for satellite and airborne sensors in both optical (0.4 to 2.5 μm) and thermal regions (8.0 to 14.0 μm) (Richter and Schlapfer, 2015). Three different ATCOR modules are available: ATCOR2, ATCOR3, and ATCOR-4. The first mentioned two modules are designed for satellite imagery and ATCOR-4 is for airborne imagery (Richter and Schlapfer, 2015). For hyperspectral radiometric correction ATCOR-4 software that is specially designed for HySpex hyperspectral data was used. This procedure is necessary to correct for the effects of atmospheric water vapor, optical thickness of the atmosphere, position of the sun, and differences in illumination caused by topography.

A brief explanation about ATCOR can be found at (Davaadorj, 2019). For ATCOR, a key formula to perform atmospheric correction is as follows (Richter and Schlapfer, 2015):

$$L = L_{path} + L_{reflected} = L_{path} + \frac{\tau \rho E_g}{p} = c_0 + c_1 DN \qquad \text{(Eq. 4)}$$

where L_{path} is the path radiance or photons scattered from atmosphere without having ground contact, τ is the atmospheric transmittance, ρ is the surface reflectance, and E_g is global flux on the ground. From Eq. 4 the surface reflectance can be derived as:

$$\rho = \frac{\pi \{ d^2 (c_0 + c_1 DN) - L_{path} \}}{\tau E_g} \qquad \text{(Eq. 5)}$$

where d^2 is the Sun to Earth distance (d is in astronomic units). The lookup tables for path radiance and global flux are calculated for d=1 in ATCOR. Thus, for the ATCOR algorithm, it is important

to know the correct calibration coefficients c_0 and c_1 in each spectral band for the specified sensor as explained in section 3.1 "Raw images to at-sensor radiance images".

Using the ATCOR-4 software package, the orthorectified masked hypercubes were input alongside the flight line DEM, the total precipitable water vapor value (extracted from the Aqua – MODIS water vapor MYD_05 product), the hypercube slope, the scan angle, the slope and aspect maps generated during orthorectification, the sensor model for the hypercube generated during calibration, and the flight line navigation file. ATCOR-4 also requires information about aerosols. The days in which the imagery was taken were completely clear sky days and a default visibility value of 23 km was used to account for aerosols load.

The ATCOR-4 output was an radiometric corrected flight line hypercube image of ground reflectance values, and several additional ancillary files such as visibility index map (corresponding to total optical depth at 550 nm) and aerosol optical thickness map, a water vapor map, vegetation indices (SAVI, LAI, FPAR), spectral direct and diffuse irradiance cubes and masks of haze/cloud/water, and saturated pixels.

3.4.1. Bidirectional reflectance distribution function correction

An additional consideration when correcting radiometry is to account for the viewing and solar illumination geometry. Most Earth surfaces do not reflect incident radiation in a two-dimensional Lambertian function manner, where the apparent brightness remains the same to an observer regardless of view angle. Instead, Earth surfaces frequently exhibit anisotropic reflectance, where apparent brightness to an observer is dependent on the surface properties, the angles of incidence and reflection, and observer angle. The mechanisms for anisotropic reflectance

include specular reflections, volume scattering in vegetated canopies and snow and ice, sunglint on water from surface roughness, and geometric optical scattering such as shadows cast by leaves, shrubs, buildings, topography, etc.

Anisotropic reflectance can significantly alter the measured radiometry and surface reflectance of the same land cover type depending on the solar illumination, wavelength, surficial properties and viewing angle of the sensor and must, therefore, be corrected for to ensure consistent radiometry across a scene. High solar zenith angles that are exhibited in high-latitude regions further exacerbate this effect. The bidirectional reflectance distribution function (BRDF) describes surface reflection for incident light within a hemisphere from direction (θ_i, φ_i) observed from direction (θ_r, φ_r) (Figure 18). The BRDF is defined in equation 6 as the ratio of the spectral radiance $L_r(\theta_r, \varphi_r, \lambda)$ reflected from a surface in a particular viewing direction (θ_r, φ_r) to the spectral irradiance $E_i(\theta_i, \varphi_i, \lambda)$ at the surface in a direction (θ_i, φ_i) (Matsapey et al., 2013).
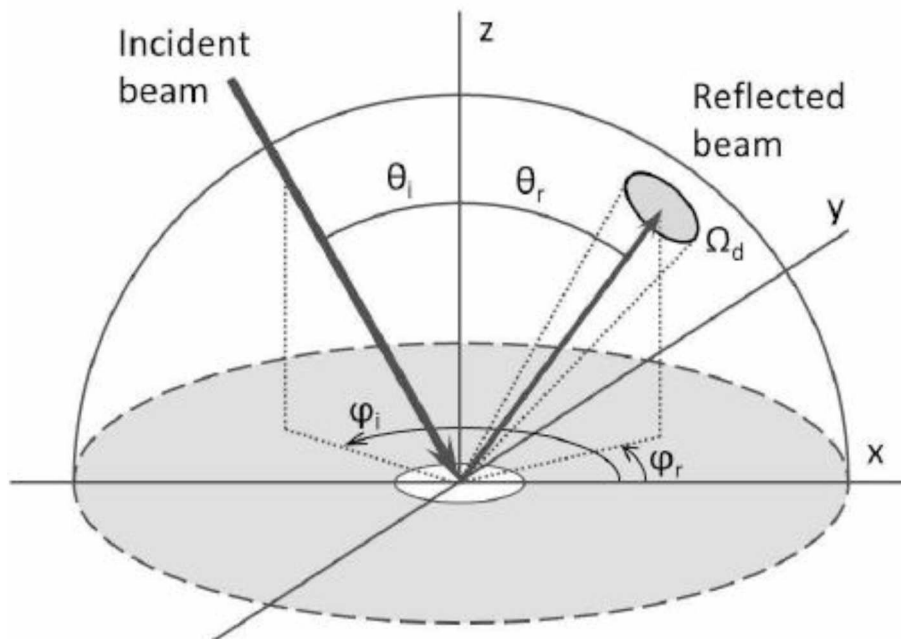

Figure 18. Geometry for the definition of the BRDF. From Matsapey et al., 2013. "Design of a Gonio-Spectro-Photometer for Optical Characterization of Gonio-Apparent Materials."

$$BRDF(\theta_i, \varphi_i, \theta_r, \varphi_r, \lambda) = \frac{L_r(\theta_r, \varphi_r, \lambda)}{E_i(\theta_i, \varphi_i, \lambda)} \qquad \text{(Eq. 6)}$$

BRDF effects are apparent in scenes where the view and/or solar zenith angles vary over a large angular range and the observed reflectance value following standard radiometric correction for vegetated surfaces may deviate up to 30 % (Richter and Schlapfer, 2015).

Thus, BRDF effects correction method (BREFCOR) was applied to the radiometrically corrected hypercube imagery in ATCOR-4. The BREFCOR method corrects observer BRDF effects by applying a fuzzy classification index that covers all surface types as a unified continues index, and then fits the Ross-Li-sparse reciprocal BRDF model to all flightline images within a flight area, and surface cover classes to obtain a generic BRDF correction function. This BRDF correction function is used to calculate a per-pixel anisotropy factor to correct for the deviation from an averaged spectral albedo. The resulting product is a spectral albedo image hypercube for each input flightline image that is corrected for observation BRDF effects. For a more detailed description, see (Richter and Schlapfer, 2015; Schläpfer and Richter, 2014).

3.5 Spectral binning and final mosaic

Spectral binning, also called spectral windowing, consists of reading two or more adjacent spectral pixels together in order to form a unique spectral band; therefore the reading configuration of the N spectral bands can be changed to adjust the sensor spectral range to the any requested bandwidth (Figure 19). If spectral binning is done by hardware during image acquisition then it is called on-chip binning, otherwise when performed by software in data postprocessing it is then called off-chip binning (Dell'Endice et al., 2009). By binning adjacent spectral bands spectral

noise can be reduced at the cost of some spectral sensitivity, and the amount of data input into any image post-processing such a classification is reduced, expediting the process.
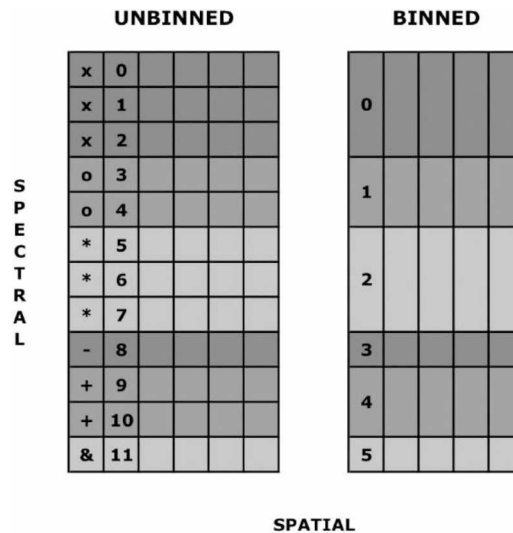
Figure 19. Spectral Binning Scheme. Two or several adjacent detector spectral rows are summed up together in order to form a single binned channel. For instance, the unbinned bands from 0 to 2 (left figure) are read together in order to form the binned band 0 (right figure). From Dell'Endice et al., "Improving Radiometry of Imaging Spectrometers by Using Programmable Spectral Regions of Interest."

The spectral albedo image hypercube output by BREFCOR contained 457 discrete spectral bands, which due to the high sensitivity of the instrument also contained some significant noise, thus spectral binning was applied to the whole dataset. After applying spectral binning the hypercube was reduced to a total of 229 bands (see Table 4 and Figure 20). Additionally, atmospheric water vapor bands were masked out of the data, as they contain no valuable information for the purposes of ground cover classification.

Once all flight lines for a flight area were orthorectified, radiometrically corrected, and spectrally binned they were mosaicked together in ENVI 5.3 to produce a single georeferenced hypercube image of the flight area. For each flight area, flightlines 1 and 2 were mosaicked, with

flightline 1 chosen as a base map. Flightline 3 was then mosaicked with the flightline 1 and 2 mosaic as a base map, and continued in the same fashion until a complete flight area mosaic was produced. To mosaic all flightline hypercubes automatic point selection was performed by ENVI 5.3 using band 3. It was ensured that at least 25 tie-points were found between two adjacent flightlines leading to a RMSE for each flight area of less than 0.5 pixels. Final mosaics were produced at 1-meter for both flight areas B and C.

Table 4. Number of bands, spectral range and spectral resolution before and after the binning process

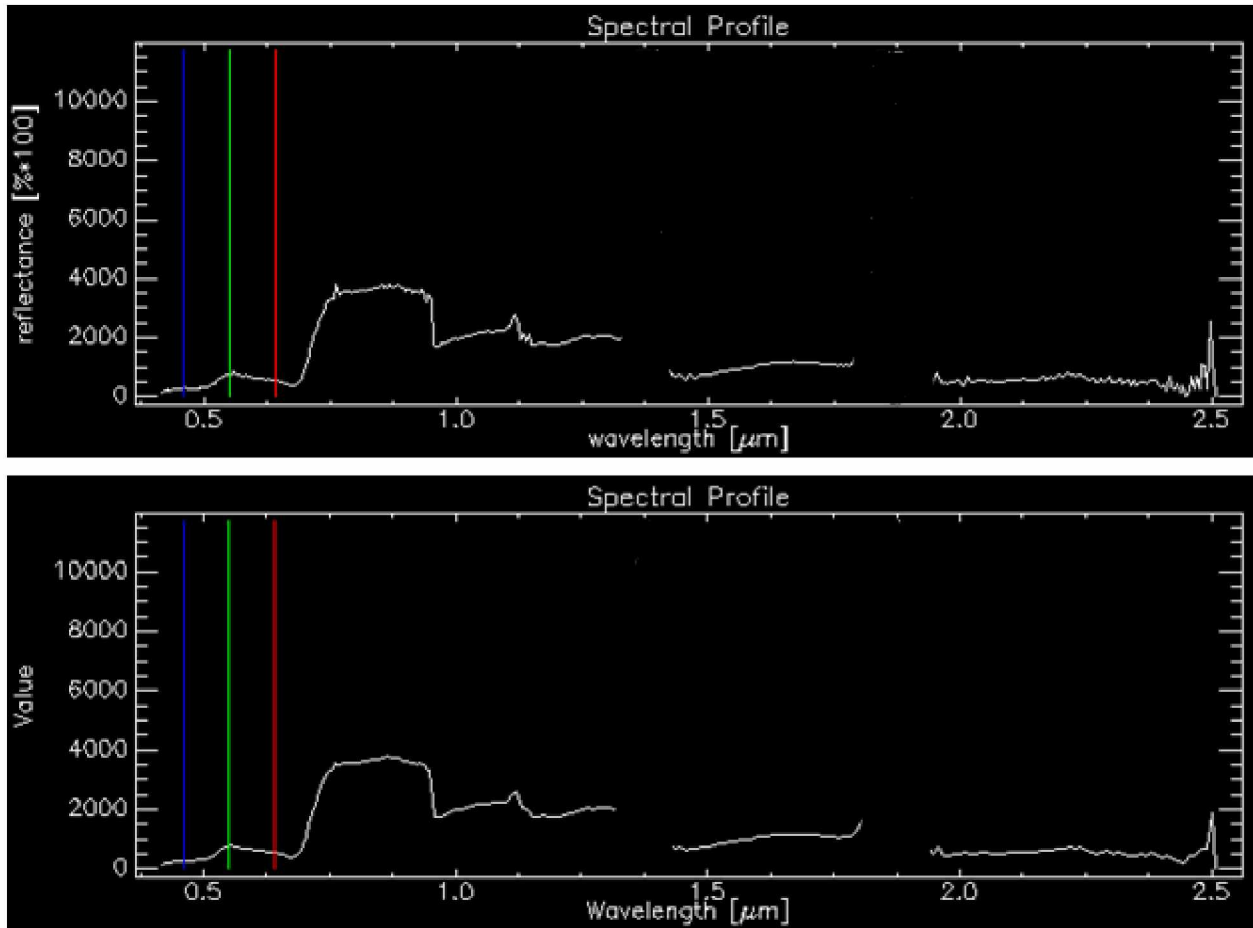|	Sensor	Band numbers in hypercube	Spectral Range (nm)	Spectral resolution per band (nm)
Without Binning	VNIR-1800	1 – 171	416.37 – 954.66	3.26
	SWIR-384	172 – 457	960.09 – 2508.55	5.45
2x Binning	VNIR-1800	1 – 85	417.96 – 949.91	6.33
	SWIR-384	86 – 229	957.37 – 2508.5	10.86

Figure 20. Spectral binning example. Single-pixel spectral profile of (top) unbinned 457-band hypercube, and (bottom) 2x-binned 229-band hypercube. Note the incresed noise in the unbinned profile

4. Wetlands Mapping

To map wetlands in the study areas B and C, unsupervised ISODATA, supervised maximum-likelihood classifications and Spectral Angle Mapping classifications were performed using ENVI 5.3 on 1-m resolution spectral albedo image hypercube mosaics.

4.1 Category definition

Flight areas B and C were classified according a six category legend (see Table 5) and further description on the main vegetation type characteristics can be found in Table 6 and Table 7. These categories included the most relevant and common vegetation found in the study area that could be detected by the available vegetation cartography. A brief category description, modified from the National Land Cover Database 92 Land Cover Class Definitions is as follows:

1. The category water was described as areas of open deepwater habitat, lacking emergent vegetation such as lakes, streams, rivers, and ponds.

2. Equisetum and emergent vegetation was described as areas where perennial herbaceous vegetation accounts for 75 to 100 percent of the cover and the soil or substrate is periodically saturated with or covered with water.

3. Bog, grasses, and sedge was described as areas characterized by natural herbaceous vegetation including grasses and forbs; herbaceous vegetation accounts for 75 to 100 percent of the cover.

4. White/Black spruce was described as areas of open or closed evergreen forest dominated by tree species (primarily *Picea mariana* and *Picea glauca*) that maintain their leaves all year, with a canopy that is never without green foliage.

5. Deciduous vegetation was described as areas dominated by trees tree species (primarily *Betula neoalaskana,* and *Populus tremuloides*) and shrubs characterized by natural or semi-

47

natural woody vegetation with aerial stems, generally less than 6 m tall, with individuals or clumps not touching to interlocking (including *Salix* ssp., and *Alnus* ssp.) that shed foliage simultaneously in response to seasonal change.

6. Bare ground was described as areas characterized by bare rock, gravel, sand, silt, clay, or other earthen material, with little or no "green" vegetation present regardless of its inherent ability to support life. Vegetation, if present, was more widely spaced and scrubby than that in the "green" vegetated categories.

Finally, it is important to note that it was not possible to deploy people on the ground to collect field spectra and vegetation samples due to time and accessibility constraints. In addition, it was ensured that these categories would be a priori detected in at least 1 m resolution pixel.

Table 5. Land cover classes

Class ID	Class Attribute	Class Description
1	wtr	Water
2	eq	Equisetum & emergent vegetation
3	bog	Bog, grasses, and sedge
4	sp	White/black spruce
5	d	Deciduous vegetation (including shrubs)
6	bg	Bare ground

Table 6. Main vegetation type characteristics for Equisetum & Emergent Vegetation (I)

Species name	Dominant wetland type	Photo	Description
Schoenoplectus tabernaemontani (syn. *Scirpus validus)*	Brackish Wetlands		Soft-stem bulrush *Schoenoplectus tabernaemontani* is a tall, perennial, herbaceous plant that grows up to ten feet tall. The leaves are highly modified into long sheaths that closely girdle stem bases. The flowers are borne in an open inflorescence of many stalked, budlike spikelet, covered by reddish brown scales below the top of the stem. The fruit is a brownish gray achene.
Carex aquatilus	Brackish Wetlands		Sod-forming perennial grass-like sedge growing 15 to 100 cm (6 to 40 in) tall. Plants arise singly or in groups connected by thick, long rhizomes. The stems or culms are triangular in cross section. Leaves are borne on the lower half of the stems; the blades are 1.5 to 5.5 mm (0.06 to 0.22 in) wide and can be shorter or longer than the culms. Each culm has a leaf-like, 3 to 19 cm (1.2 to 7.5 in) long bract subtending the inflorescence. The inflorescence consists of 1 to 3 staminate spikes above 2 to 3 pistillate spikes, often with some androgynous (male and female with male flowers on top) transitional spikes. The terminal staminate spike is 1 to 3.5 cm (0.4 to 1.4 in) long. The pistillate spikes are 1.5 to 4.5cm (0.6 to 1.8 in) long and 3 to 5 mm (0.12 to 0.20 in) wide. Each fruit (achene) is subtended by a lanceolate to rounded, blackish or black purple scale, shorter to longer and narrower than the perigynia. The scale has a green to pale brown midrib. Each achene is enclosed in a perigynium, a leathery sack-like structure. The perigynia are 2 to 3.3 mm (0.08 to 0.13 in) long. The achenes are lenticular (lens shaped) with 2 stigmas.

Table 7. Main vegetation type characteristics for Equisetum & Emergent Vegetation (II)

Species name	Dominant wetland type	Photo	Description
Menyanthes trifoliata	Freshwater Bogs		It has a horizontal rhizome with alternate, trifoliate leaves that have three elliptic leaflets (to 4" long) on petioles 4-10" long. The inflorescence is an erect raceme of Starry, 5-petaled, hairy white flowers that bloom in terminal racemes in May and June atop stems rising to 12" tall.
Equisetum fluviatile	Freshwater Marsh		The jointed central stem of this herbaceous perennial plant is 1½ to 4' tall, 4 to 8 mm. across, and erect to ascending. One form of this species produces ascending lateral branches up to 5" (12 cm.) long in whorls from the lower-middle to upper-middle nodes of the central stem, while another form doesn't produce any lateral branches. The central stem is medium green, hairless, and terete with about 12 to 24 shallow furrows and rounded ridges. The texture of the central stem is relatively smooth to the touch. At intervals there occurs sheaths that surround the joints of the central stem. These sheaths are 5 to 10 mm. long and appressed tightly against the central stem; they are mostly green or dark brown. The teeth of these sheaths are dark brown, narrowly triangular, and persistent.

4.2 Training and test areas selection

Training areas were digitized utilizing the 30 m resolution "Vegetation Map and Classification: Northern, Western, and Interior Alaska," by the University of Alaska Anchorage (UAA) (Boggs et al., 2012) as a base map, and by visual interpretation of collected HySpex images. The base map was derived from 18 regional land cover maps that were developed within the last 31 years of its publication. As previously stated, there is currently an absence of detailed information in the study area and this was the best source available while this work was being carried out.

For each category and for each flight area a total number of 50 training areas of around 7 by 7 pixels were digitized. In the case of bare ground, because of its limited representation in the study areas, the total number of training areas was 20 for Area C and 34 for Area B. To digitize the training areas, the UAA vegetation map was used as a source to locate general category areas and then, a true color image composite of radiometrically-corrected HySpex imagery including bands 12 ($\lambda = 487$ nm), 41 ($\lambda = 671$ nm) and 55 ($\lambda = 760$ nm) and a false color image composite including bands 41 ($\lambda = 671$ nm), 55 ($\lambda = 760$ nm) and 62 ($\lambda = 804$ nm) were used to ensure the vegetation type by photointerpretation of each category. To ensure spatial and spectral representation for each category, training areas were digitized along the study area (if they were present) and selecting pure and heterogeneous category areas.

Finally, 70 % of the total number of training samples were used as a training set for supervised classification, with the remaining 30 % to be used in post-classification accuracy assessment as a test set. Assignment of training and validation samples was performed randomly.

4.3 Image classification methods: maximum likelihood, hybrid classification, and spectral angle mapper (SAM)

Although there are more specific methodologies for both supervised and unsupervised hyperspectral image classification such as endmember collection, object based image classifier or decision tree analysis as a first approach three standard and well-known methods were used for wetlands mapping: maximum likelihood supervised classification, a hybrid classification (unsupervised + supervised), and spectral angle mapper (SAM) classification.

Maximum likelihood classification:

This classification assumes that the statistics for each class in each band are normally distributed and calculates the probability that a given pixel belongs to a specific class (Richards, 2013). To calculate the probability function this method needs training areas defined *a priori* containing the categories to be used to classify the imagery. In this method each pixel is assigned to the class that has the highest probability (that is, the maximum likelihood). If the highest probability is smaller than a specified threshold, the pixel remains unclassified. Probability thresholds are set between 0 and 1. A single probability threshold value of 0.5 was used for all classes.

Hybrid classification:

This classification consists of an IsoData unsupervised classification in which pixels are aggregated into clusters depending on their spectral characteristics and a supervised classification in which the spectral clusters become thematic categories using training areas (Serra et al., 2003).

The IsoData unsupervised classification calculates class means evenly distributed in the data space then iteratively clusters the remaining pixels using minimum distance techniques. Each iteration recalculates means and reclassifies pixels with respect to the new means. Iterative class splitting, merging, and deleting is done based on input threshold parameters. All pixels are classified to the nearest class unless a standard deviation or distance threshold is specified, in which case some pixels may be unclassified if they do not meet the selected criteria. This process continues until the number of pixels in each class changes by less than the selected pixel change threshold or the maximum number of iterations is reached.

After a round of first guess tries, it was finally decided to run three tries for each spatial resolution (1 and 5 m) using the parameters on Table 8.

Table 8. ISODATA tries

ISODATA Parameter	Try 1	Try 2	Try 3
Minimum # of classes	7	7	24
Maximum # of classes	14	14	48
Maximum iterations	20	20	30
Change threshold percent	5	5	5
Minimum # of pixels in class	25	50	25
Maximum class standard deviation	1	1	1
Minimum class distance	5	15	5
Maximum # of merge pairs	2	6	6

Finally, in the supervised step depending on the fidelity and representativeness thresholds, each spectral class from the unsupervised classification class will be linked to a corresponding thematic class or left as unclassified.

Spectral Angel Mapper:

Spectral Angel Mapper (SAM) is a physically-based spectral classification that uses an n-D angle to match pixels to reference spectra (Kruse et al., 1993). The algorithm determines the spectral similarity between two spectra by calculating the angle between the spectra and treating them as vectors in a space with dimensionality equal to the number of bands. This technique, when used on calibrated reflectance data, is relatively insensitive to illumination and albedo effects.

Endmember spectra used by SAM were input as ROI average spectra from the training dataset. SAM compares the angle between the endmember spectrum vector and each pixel vector in n-D space. Smaller angles represent closer matches to the reference spectrum. Pixels further away than the specified maximum angle threshold in radians are not classified (Kruse et al., 1993).

After a first batch of SAM classification results, four threshold configurations were set for each area (see Table 9).

Table 9. SAM Tries

		Threshold angles in radians					
Category	Try	Water	Equisetum	Bog	Spruce	Deciduous	Bare ground
Area B	1	1.75	0.25	0.15	0.2	0.2	0.15
	2	1.75	0.25	0.15	0.2	0.2	0.15
	3	1	0.2	0.175	0.25	0.2	0.15
	4	0.5	0.15	0.175	0.2	0.2	0.15
Area C	1	0.1	0.3	0.1	0.1	0.2	0.1
	2	0.5	0.2	0.1	0.2	0.2	0.1
	3	1	0.3	0.2	0.3	0.2	0.1
	4	1.75	0.25	0.15	0.2	0.2	0.15

4.4 Classification overall accuracy: confusion (error) matrix

The error matrix is a means of comparing two thematic maps. This is typically done in a tabular or array form (see Figure 21). In remote sensing image analysis, the two thematic maps are often a "ground truth" map (the reference map) and a map derived from automated image classification (the classified map). The error matrix permits the calculation of a range of measures that describes the accuracy of the classified map with respect to the reference map. Usually, the information in the horizontal rows normally corresponds to the thematic classes of the reference map. The vertical columns show the thematic information resulting from automated image classification.

Thematic map to test							
		Urban	Crops	Water	Forest	Total	Commission error	CA %
Ground truth	Urban	100	15	2	9	126	21	79
	Crops	0	114	5	23	142	20	80
	Water	2	5	78	6	91	14	86
	Forest	12	17	4	214	247	13	87
	Total	114	151	89	252	606		
	Omission error	12	25	12	15			
	PA %	88	75	88	85			

Figure 21. Example of a confusion (error) matrix. PA % is the Producer's accuracy, CA % is User's accuracy, Omission error is 1-PA, Commission error is 1-CA.

To generate the error matrix, the thematic information was extracted from the three classification procedures (see Section 4.3 Image classification methods: maximum likelihood,

hybrid classification, and spectral angle mapper (SAM)) where the ground truth from test dataset was located (see Section 4.2 Training and test areas selection).

The overall model accuracy is calculated by dividing the total number of correctly classified points (diagonal in the error matrix) by the total number of points within the error matrix. As it is named, the overall accuracy gives a general idea of the model's performance, but more detailed calculations are needed to assess each class separately. The producer's accuracy is calculated by dividing the number of correct pixels for each class by the total number of pixels in that class. This accuracy represents the probability of a reference point of that class being classified correctly. It gives the producer of the map an idea about how accurately each class can be classified. The user's accuracy is calculated by dividing the number of correctly classified points by the total number of points classified as that class. This accuracy provides the reliability to the user of the map that each class on the map actually represents that class on the ground. The kappa analysis is computed by running the KHAT statistics as follows:

$$K = \frac{N \sum_{i=1}^{r} x_{ii} - \sum_{i=1}^{r}(x_{i+} * x_{+i})}{N^2 - \sum_{i=1}^{r}(x_{i+} * x_{+i})}$$

(Eq. 7)

where N is the total number of observations, r is the number of rows in the matrix, xii is the number of observations in row i and column i, xi+ and x+i are the marginal totals of row i and column i, respectively (Congalton, 1991).

The kappa analysis can be used to determine how much better the results are from the error matrix than random results. A kappa value of 0 means that our results are no better than a random result while a kappa value closer to 1 indicates that our results are significantly better than a random result.

5. Results and Discussion

Imaging spectroscopy generates a large volume of data that is often complex and time-consuming to process and analyze. Results presented in this study are from the inaugural campaign for the HySpex system at the University of Alaska Fairbanks. The acquisition over the Yukon Flats was intended to be a test of the system's feasibility for acquiring robust and timely hyperspectral data in Alaska. As such, there have been some systematic data errors within the collected imagery that need to be addressed. The two most prominent errors are a systematic sensor response drop in the VNIR sensor when the field of view optics were attached, and striping present in some bands of the corrected VNIR and SWIR images.

5.1 Commissioning and data acquisition

The HySpex system was successfully commissioned into the US Fish and Wildlife Service single engine Found Aircraft Bush Hawk. The designed flexibility and modular nature of the HySpex system made it relatively straight forward to test, transport, install, and remove the system multiple times before the acquisition flights. This allowed us to perform preflight measurements and test components of the system at the USFWS hangar at the Fairbanks International Airport, or at the University of Alaska Fairbanks Geophysical Institute depending on our needs. Fabrication of an aluminum mounting plate for the vibration dampening mount and wooden mounting board for the DAU and power system with measured mounting hardpoints for the camera system and aircraft floor plates (Figure 22. Mounting plates and boards. Fabrication of mounting plates and boards, and modular design of HySpex camera system allowed for rapid commissioning into aircraft, and potential for rapid deployment in subsequent acquisition campaigns) was essential for timely recommissioning into the same aircraft, streamlining the commissioning process for potential future acquisition

campaigns. Moreover, the implemented design in Figure 22 was also successfully implemented to other small aircraft such as a Husky and a Beaver.

During initial commissioning, the HySpex system was removed from the aircraft to allow for USFWS refuge wildlife inventory flights, and then quickly reintegrated into the aircraft for hyperspectral image acquisition flights during favorable weather windows. This is a particularly useful feature for aircraft and agencies with multiple concurrent missions and studies, and for remote sensing in a region with dynamic and rapidly changing weather conditions.

Before proceeding to the study area, a flightline containing previously selected and easily distinguished features with high GPS accuracy was collected over the University of Alaska campus to be used in a boresight calibration (see Figure 15).

The HySpex system requires the system to power on while the aircraft is on the ground to establish an internal navigation system solution (INS solution) for accurate positional data to be collected and recorded by the IMU. Typically, if the system is powered on after flight has begun, or shut down for a prolonged period, an INS solution cannot be made. During the September 2 acquisition flight, the HySpex system experienced a power failure when the connection from the UPS to the aircraft electrical system was disrupted. The low capacity of the UPS battery backup was insufficient for the system's power needs, and power was lost, resulting in an internal navigation system failure (INS failure). However, the connection to the aircraft power was quickly repaired in flight, and the system was restarted. The INS solution was reestablished with an "INS Solution Good" message displayed, and image acquisition was continued. No errors were found in the navigation log file.

Figure 22. Mounting plates and boards. Fabrication of mounting plates and boards, and modular design of HySpex camera system allowed for rapid commissioning into aircraft, and potential for rapid deployment in subsequent acquisition campaigns

5.2 Image Processing

5.2.1 Systematic VNIR sensor response drop correction and systematic stripping in VNIR and SWIR spectral bands

During initial geometric processing, a systematic drop in the VNIR sensor response was discovered (Figure 23) along the edges of the acquired imagery. To maintain high radiometric fidelity in the final mosaicked flight area image, the low sensor-response areas along the edges of the raw image files were masked out for all flight lines and reprocessed for geometric correction, resulting in geometrically corrected flight lines without this systematic radiometric artifact. A script was developed to help automate the masking of the first and last 100 pixels showing sensor-response drop for the 18 VNIR flight line radiance images of flight areas B and C. VNIR radiance images were then reprocessed from the georectification step onwards to produce masked spectral albedo image hypercubes for spectral binning and mosaicking.

After discovering the sensor response drop in the imagery, an investigation into the cause of this behavior was conducted on the HySpex cameras. The cameras were tested utilizing a calibrated integration sphere with and without field of view expander optics attached. Response drop was observed only when the optics were attached, and was determined to be the cause of the error during flight acquisition.

One adverse effect of masking out the VNIR sensor response drop areas was the introduction of some minor data gaps within the final flight area mosaics (Figure 24). Planned flightline sidelap was initially calculated based on the full swath of the sensors. In some areas of the mosaic, the combination of aircraft banking during flight correction and reduced swath of the flightline following sensor response drop masking of edge pixels resulted in a loss of data for some

areas along flightline edges. Thus, it is essential to account for Hyspex sensor response drop areas in future campaigns.

During geometric and atmospheric processing, several bands within the VNIR and SWIR images were found to exhibit systematic striping across the image in the along-track (or flight) direction. To ensure high radiometric fidelity, bands 1 to 3, 99 to 102, 122 to 128, 136 to 150, 156, and 200 to 204 exhibiting systematic striping, as well as spectral noise due to water vapor were omitted from the final data set, after the spectral binning step and prior to orthomosaicking and classification.
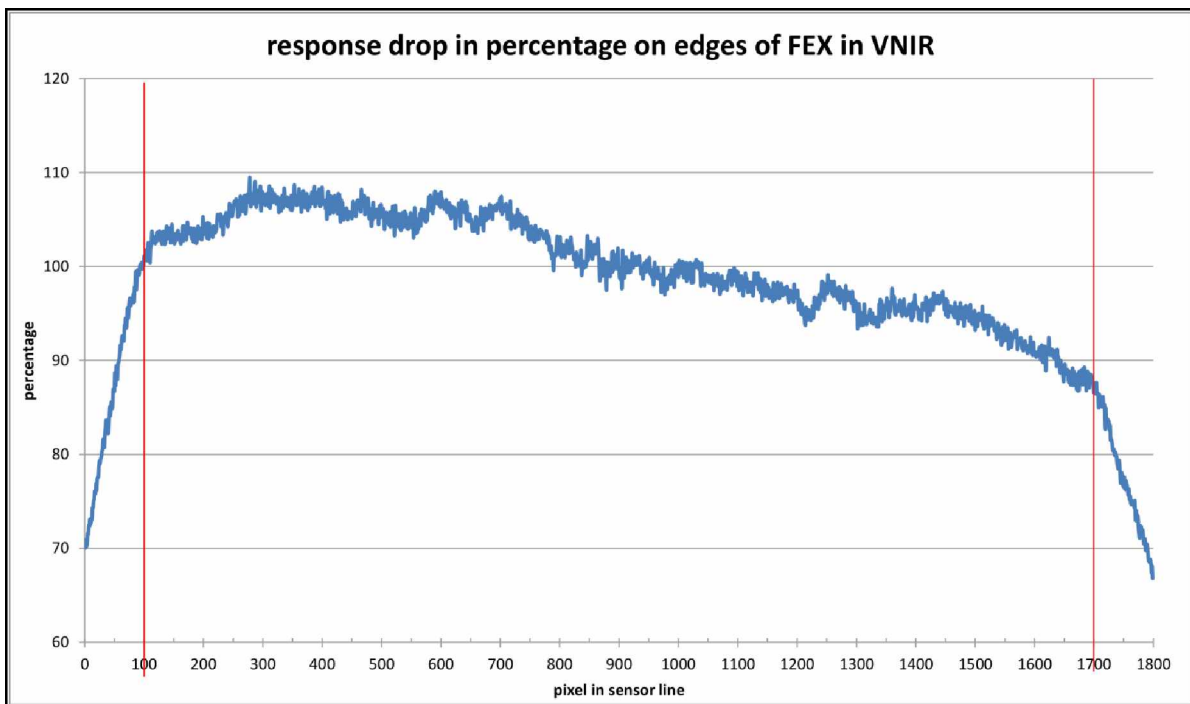

Figure 23. Sensor response drop on edge pixels of VNIR flightline, shown by red line.

Figure 24. Example of data gap. Data gap shown in red box, and detailed in lower right window in flight area C orthomosaic introduced by masking flightline edge-pixels.

5.2.2 Geometric and radiometric corrections

While the small size and modularity of the HySpex system allows it to be commissioned in small aircraft, issues with geometric correction do arise from the relative instability of flight in smaller aircraft. The Bush Hawk was an excellent aircraft choice for flights in the remote areas of Interior Alaska and an overall well-performing acquisition platform for HySpex imagery, however there were some issues that should be considered for future flights. Flight attitude corrections during acquisition may have led to some image artifacts that were not adequately corrected for during georectification. Several areas in georectified flightlines exhibit a "smearing" effect in areas of the flightline where flight-attitude corrections were made. This may have occurred due to high

roll and/or pitch rates that approached or exceeded the sampling rate of the IMU, or frameperiod of the camera system. Although the aircraft pilot performed an excellent flight, it is possible that a larger and more stable platform may need fewer flight attitude corrections while collecting imagery in a flightline, reducing geometric errors in the results. The trade-off is that the larger airplanes will not have the same flexibility as the smaller airplanes have when commissioning instrumentation and flying in remote areas, as they require more time for permits and mission planning. We chose to give a higher importance to the flexibility and went with a small aircraft and put significant efforts in data processing to reduce geometric errors. The data processing resulted in geometric corrections with a desired RMSE lower than 0.5 pixels. For future acquisitions, if issues described in this section together with those in sections 5.2.1 and 5.2.2 are taken into account in the flight planning step, this will further alleviate issues in the image acquisition step. This will help to generate image mosaics with higher geometric fidelity and with greater ease.

Another factor that might help increase the geometric accuracy, especially when planning repeated flight campaigns in the same area, is using Real-Time Kinematic (RTK) GPS measurements that provide more accurate GPS readings allowing for a more accurate geometric correction. Subscription to satellite-based augmentation systems, such as OmniStar that utilize L1/L2 carrier-phase correction signals with dual frequency compatible receivers, such as the IMAR iTRACE, or use of post-processing differential GPS correction in regions with GPS receiver base stations with long residence times and high positional accuracy might also be used to increase the accuracy of georectification. Unfortunately, these high-accuracy measurements could not be acquired for this mission but they are paramount when acquiring imagery in the same area and comparing results.

A current limitation of the HySpex system is the need to perform a boresight calibration. In more advanced platforms in which HySpex technology is used, HySpex ODIN-1024, there is no need to apply further boresight calibrations as both camera are optimally coregistered. Unfortunately, at the time the HySpex VNIR-1800 and SWIR-384 were acquired by UAF, the HySpex ODIN-1024 was not available in the market. This limitation required an additional image resampling when coregistering the VNIR and the SWIR datasets. The SWIR dataset was resampled twice, when geometrically correcting each flightline and again when mosaicking each flight line area. It is important to note that in order to avoid a second resampling for SWIR imagery, a new methodology in the boresight calibration was tried where VNIR image coordinates were mapped to projected coordinates, SWIR image coordinates were mapped to VNIR image coordinates, and then projected VNIR coordinates were then linked to SWIR image coordinates, thus eliminating a resampling of the SWIR flightline. However, this method only worked for a limited number of flight lines and ultimately had to be discarded.

A final consideration for improving the geometric accuracy is the precise measurement of the lever arm offset between the IMU and GPS antenna receiver, and the virtual measurement point of the HySpex cameras. These offsets must be measured and applied to the IMU initialization files to account for the discrepancy between the position of the antenna, and the position of the IMU collecting angular rate, acceleration, attitude, true heading, and velocity measurements and the optical center of the boresight calibration and point where data is collected. Accurate measurements of sub-centimeter precision of these offsets that are utilized for georectification is essential, as inaccuracies can introduce large systematic errors to the final projection of image pixel coordinates of VNIR and SWIR flightlines. Accurate radiometry through the whole spectral profile is contingent upon good geometric coregistration between the camera systems. For

example, a misregistration between VNIR and SWIR pixels along an ecotone with sharp vegetation transition may drastically alter the spectral profile for a hypercube pixel. Therefore, the importance of accurate georectification is heightened when using a dual camera hyperspectral system.

The radiometric correction displayed a good visual performance for all land categories except for water (see Figure 25 and Figure 26). Although no field spectra were taken due to logistics, when land categories were visually compared to similar spectra taken from available spectral libraries (Ecosystem Spectral Information System, https://ecosis.org/search/ and ECOSTRESS, https://speclib.jpl.nasa.gov/library) these followed a similar shape. However, in the water category, ATCOR4 under corrected the water spectra giving negative values beyond 820 nm where water reflectance was supposed to be 0 (see Figure 25 and Figure 26). This was not critical for the classification process as this issue was the same for all flight lines. However, if absolute values or reflectance are needed to model surface energy fluxes such as albedo, a better radiometric correction for this category is needed as well as in situ field spectra collection.
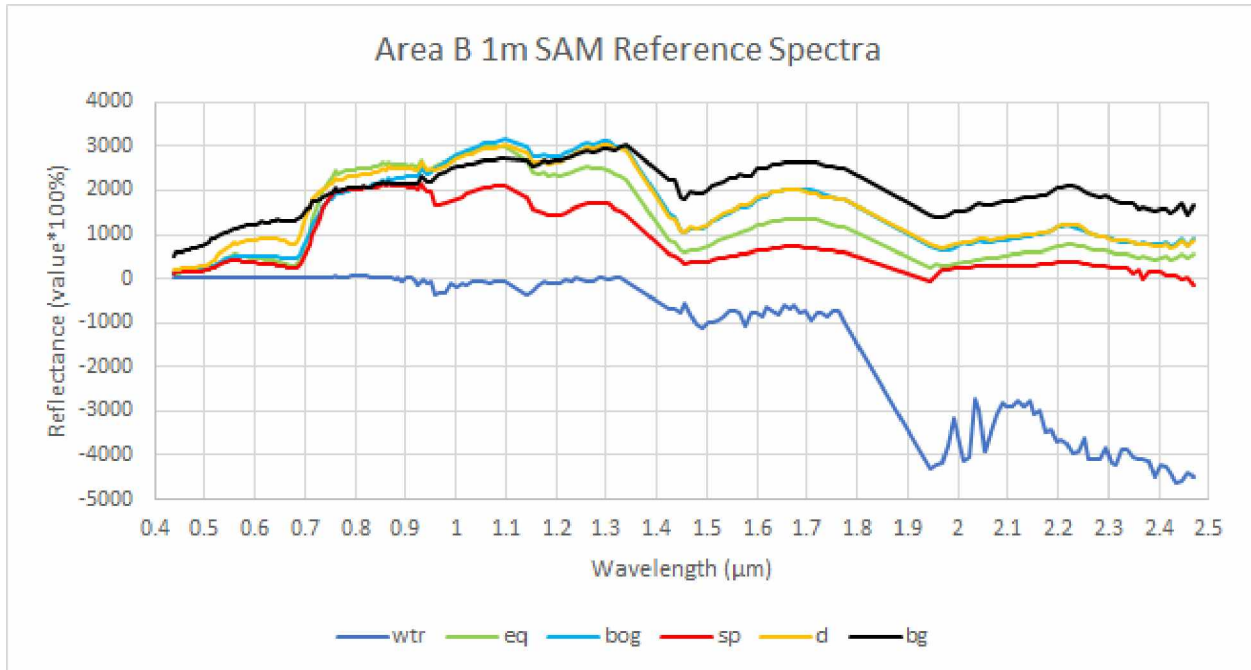
Figure 25. Spectral signatures for area B. Water (wtr), equisetum & emergent vegetation (eq), bog, grasses, and sedge (bog), white/black spruce (sp), deciduous vegetation (d) and bare ground (bg) shown
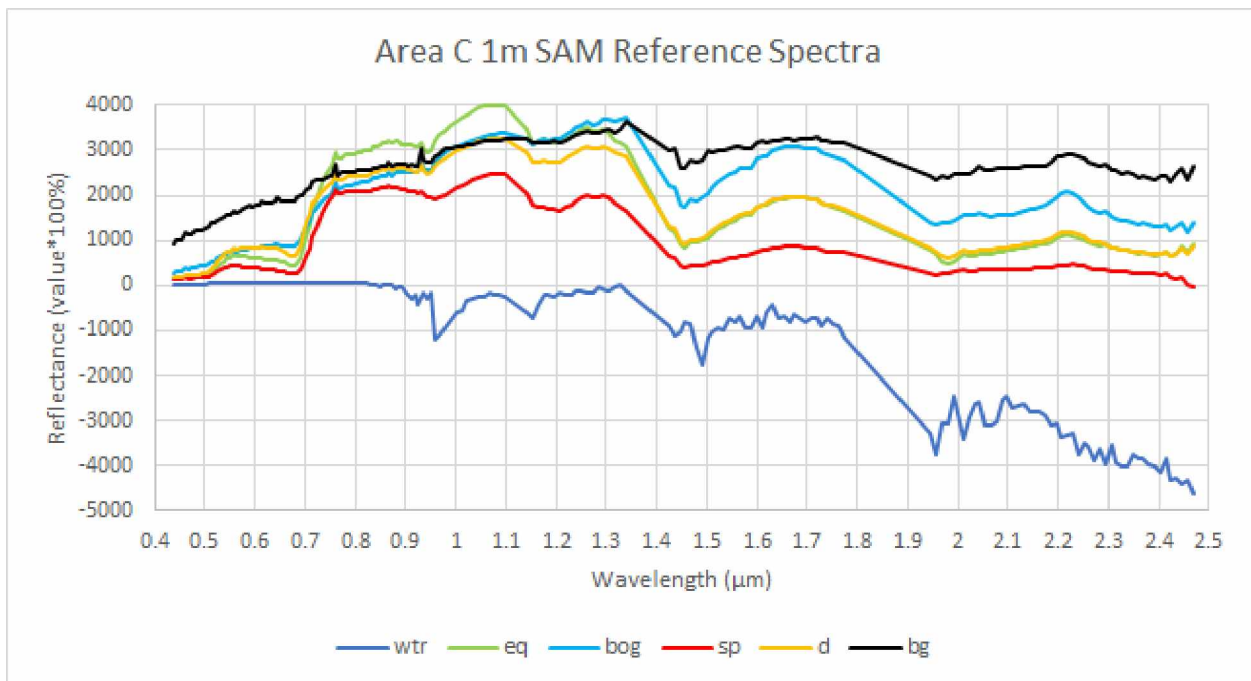

Figure 26. Spectral signatures for area C. Water (wtr), equisetum & emergent vegetation (eq), bog, grasses, and sedge (bog), white/black spruce (sp), deciduous vegetation (d) and bare ground (bg) shown

5.2.3 Orthomosaic and final hypercube integration

Figure 27 and Figure 28 show the final orthomosaics for B and C area, respectively. Thanks to the geometric correction of less than 0.5 pixel RMSE, both mosaics were almost seamless. However, there were minor areas in both mosaics in which the automatic registration process applied to generate the final mosaic between all flightlines produced a disjointed area. Those areas were small and located at the edges of the flightlines and a difference of around three pixels was visually detected between two consecutive flightlines where the disjointed area was. In the registration process, tie-points between two adjacent flightlines are taken automatically and a minimum of 20 tie-points with RMSE values less than 0.5 were ensured. However, sudden changes in roll, pitch or yaw because of flight conditions may introduce geometric artifacts that the geometric correction could not solve properly. To address this issue, more tie-points will need to be added manually.

Finally, and unfortunately, although data were collected under a clear sky day there was a low cirrus cloud that obstructed one of the flightlines in area B, altering reflectance values (see Figure 27 bottom right area).
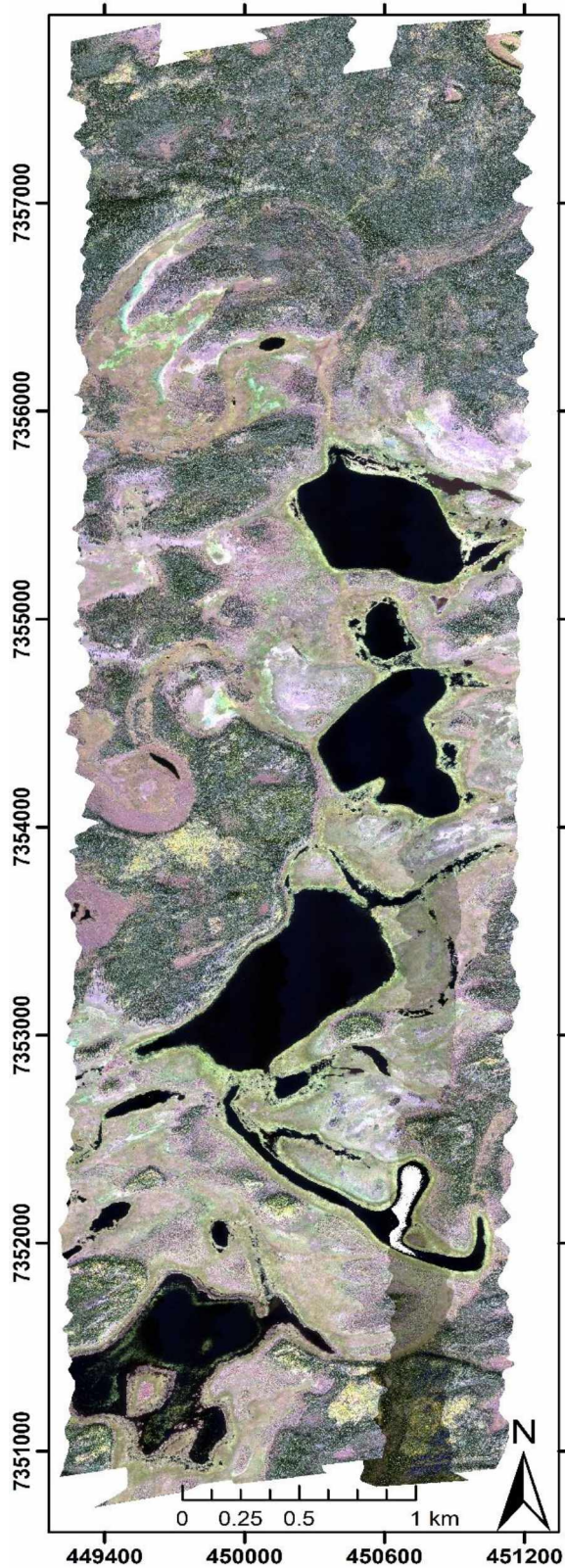
Figure 27. Area B true color orthomosaic. True color (Red: band 72; Green: band 43; Blue: band 15) orthomosaic for area B at 1m spatial resolution. Coordinates in UTM-6N and datum in WGS-84.
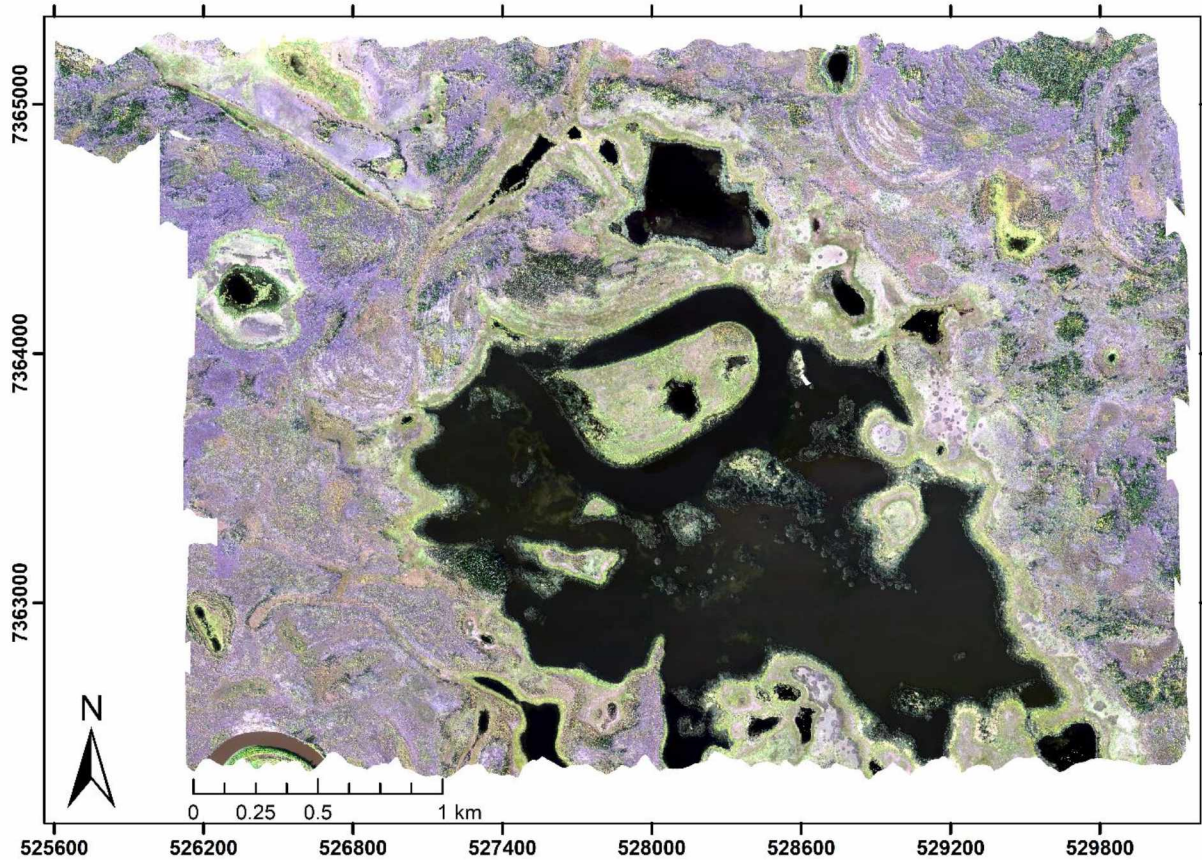
Figure 28. Area C true color orthomosaic. True color (Red: band 72; Green: band 43; Blue: band 15) orthomosaic for area C at 1m spatial resolution. Coordinates in UTM-6N and datum in WGS-84.

5.3 Image classification: results

Figure 30 and Figure 31 and Table 10 and Table 11 show the classification and accuracy results for the best hybrid classification using the try 3 configuration (see Table 9) for B and C areas, respectively. Kappa values for hybrid classifications area B and C were of 0.42 and 0.44, respectively.

Figure 32 and Figure 33 and Table 12 and Table 13 show the classification and accuracy results for the best maximum likelihood classification with a try using a 0.5 probability threshold

and 3x3 mode filter window applied for B and C areas, respectively. Kappa values for maximum likelihood classifications area B and C were 0.9 and 0.92, respectively.

Figure 34 and Figure 35 and Table 14 and Table 15 show the classification and accuracy results for the best SAM classification using try 1 and try 4 for areas B and C (see Table 9), respectively. Kappa values for hybrid classifications area B and C were 0.57 and 0.6, respectively.

Best classification performance occurred when using the maximum likelihood classifier, followed by the SAM classifier and lastly by the hybrid classifier showing lower performance in both flight areas. In all three cases, Kappa values were higher for the maximum likelihood classifier as well as the producer's and user's accuracy. It would be expected that SAM methodology, widely used for hyperspectral image classification would yield higher performance than maximum likelihood techniques. We believe that the lack of field spectra or a specific spectral library for high latitude areas including different types of vegetation, water and soils might have caused this method to perform more poorly, as SAM classification relies on this external dataset. In the absence of standard spectral libraries for Arctic vegetation and field-based spectra, training areas were used in place of a spectral reference dataset. When these training areas were used with the SAM classifier, more than 35 % of the final image was not classified due to the lack of proper spectra. To assign non classified pixels to categories a selective mode filter with a 3 by 3 convolution matrix was used. This helped to remove non classified pixels and increased image accuracy, but the performance was still lower than the maximum likelihood method. Jollineau and Howarth (2008) similarly found maximum likelihood classification achieved higher accuracy than SAM based on image-derived spectral endmembers utilizing airborne hyperspectral CASI data in an inland wetland complex near the Grand River, a tributary of Lake Erie in Ontario, Canada. This study also grouped different wetland vegetation species into broader land cover classes. Pixel-

based classifiers, such as SAM have also shown to perform best for hyperspectral imagery when extracting individual spectra for different plant species (Harken and Sugumaran, 2005).

Hybrid classification showed the poorest performance with a Kappa around 0.4. The misclassification between equisetum, spruce and deciduous was the main reason for this lower performance. Finally, it is interesting to note that the low cirrus cloud that affected area B bottom right section caused misclassification in the hybrid and maximum likelihood classifications, it did not impact the final map for SAM classification. An advantage of SAM classification is that because it is dependent on the angle between two vectors in n-dimensional space, but not the vector magnitude, it is insensitive to varying magnitudes of illumination for equivalent cover types (Kruse et al., 1993; Leckie et al., 2005).

For the maximum likelihood classifications, there was confusion between spruce and equisetum categories in emergent areas, and especially in SAM and hybrid classifications. Better results were found in the maximum likelihood classifications due to an increase of the training dataset on these areas *a posteriori*. Those expanded training datasets were also used in the hybrid classification, but the results did not improve. The mixing of plant and water signals in areas of flooded emergent vegetation results in a decrease in total reflected radiation, and the intensity of this effect is dependent on vegetation density, water depth, and canopy structure (Silva et al., 2008). Due to the wide range of reflectance values that may be represented in areas of emergent vegetation, the spectral signature of this class may overlap the signals from water, terrestrial vegetation, and soil. The lowered reflectance values of the equisetum class in some areas were similar to the spruce class spectral signature, causing misclassification between the two when using spectrally-based methods. Similar SAM misclassifications for hyperspectral imagery between conifer species and emergent vegetation have been described by Harken and Sugumaran (2005)

71

and generally in several other wetland studies (Jollineau and Howarth, 2008; Ozesmi and Bauer, 2002; Silva et al., 2008). To solve this issue, a buffer of around 100m along the lakes could be applied to mask out spruce pixels within these areas and reclassify them into equisetum category. If available, a LIDAR flight or a Digital Surface Model could also help to discriminate between both categories as spruce trees are taller than equisetum.

Timing image acquisition during periods of maximum spectral separability between plant communities or species of interest may further enhance classification efforts. Best et al. (1981) found that spectral reflectance differences were statistically significant between stands of hydrophytes, with maximum separation of species occurring during flowering or early seed stages. This, however, requires a detailed characterization of spectral responses over time between land cover types, which currently do not exist for Alaska in published spectral libraries.

Deciduous and spruce classes also showed some confusion. Deciduous and spruce usually form mixed forest which is not easy to classify in this landscape. Moreover, due to the low angle of the Sun above the horizon the resulting imagery has self-cast shadows projected in the same vegetation that could also lead to misclassification between both categories. Spruce and deciduous classes were notably misinterpreted as equisetum class in these shadowed forested areas. Therefore, resampling the whole imagery at 5m spatial resolution could be useful to increase the accuracy for both categories by integrating the shadowed regions within a pixel and averaging the spectral response between shadowed and non-shadowed areas of the same class. The addition of a shadow class could also be useful here, especially for any spatial statistical analyses that end users might perform on the thematic maps for land management or other purposes.

Bare ground category showed intermediate accuracy in area B, low accuracy in area C, and had the least area representativeness of all other categories. Thus, it was not an easy category to

72

classify and it needs to be better defined. The spectral endmember of the bare ground category may not be pure, and when compared to dead vegetation spectra this category also showed some similarities. An example spectral profile for a bare ground class training pixel (Figure 29, left) shows a visual similarity to ground spectra of dead vegetation shown as a dark black line in the right panel of Figure 29.
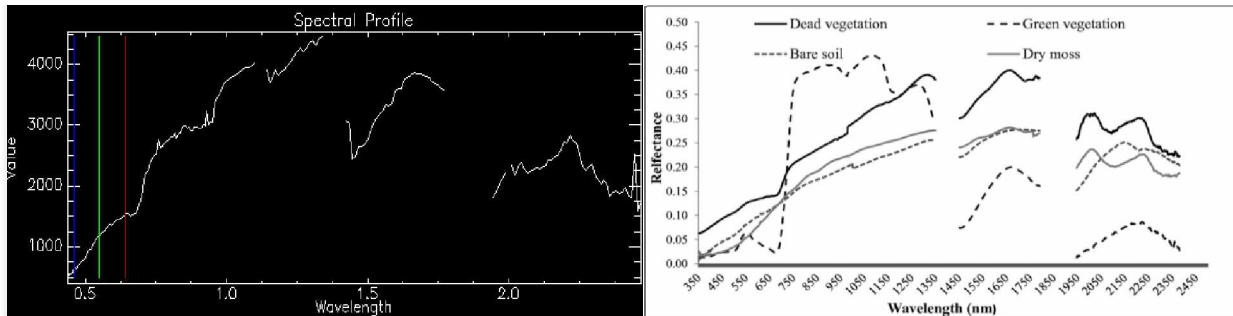

Figure 29. Comparison of Bare Ground Spectra. Left: bare ground spectra from HySpex imagery. Right: spectra from dead vegetation (Image from Li et al., 2014)

Finally, water, bog and equisetum categories yielded high accuracy of more than 90 % in users' and producer's accuracy. These categories each covered fairly broad land cover types, and incorporated different vegetation types with similar spectral, spatial, and canopy characteristics. Further segmentation of these classes into narrower categories would require more *in situ* knowledge of and data for the imaged areas, as well as detailed spectral characterization, and possibly alternate classification techniques to accurately identify and assign classes.
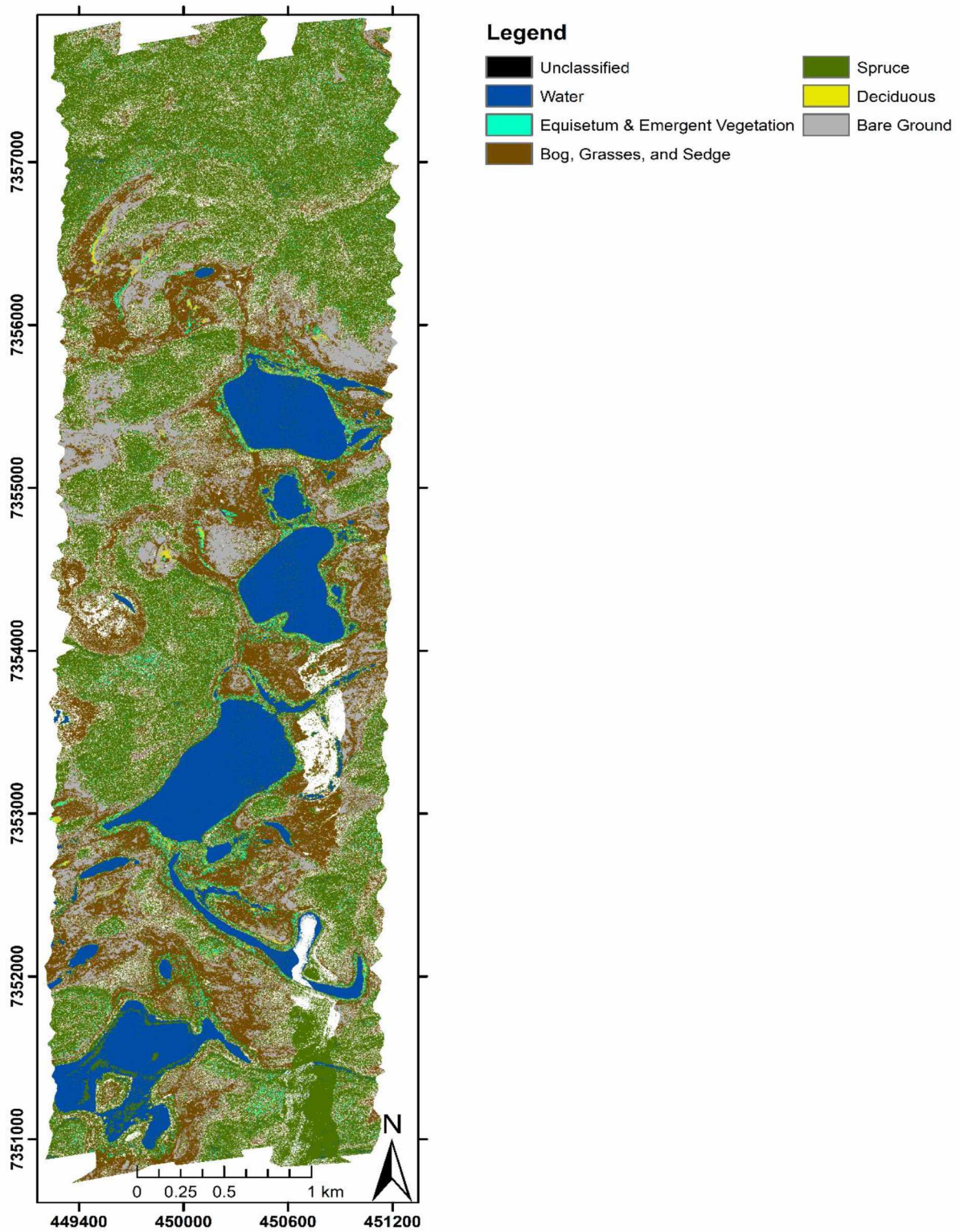
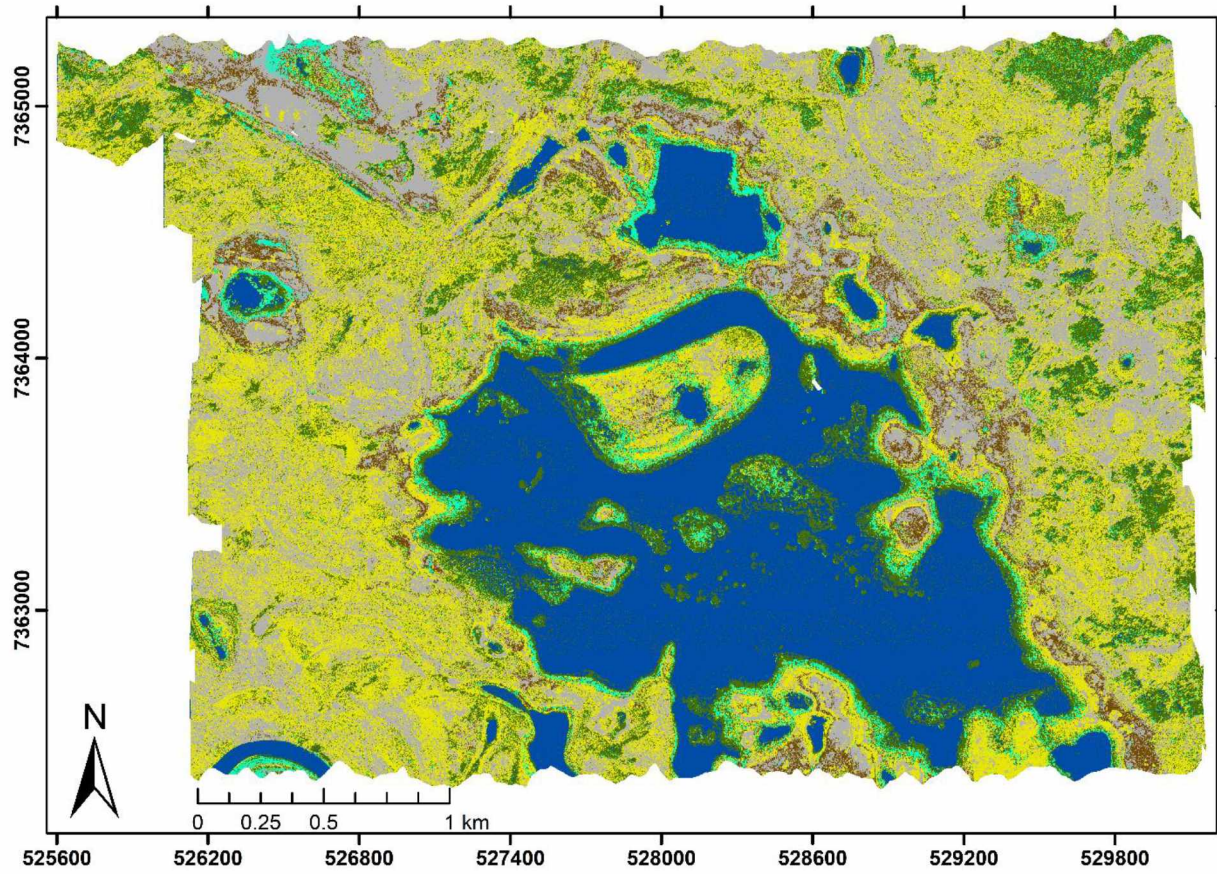Figure 30. Best hybrid classification for Area B. Coordinates in UTM-6N and datum in WGS-84

Figure 31. Best hybrid classification for Area C. Coordinates in UTM-6N and datum in WGS-84
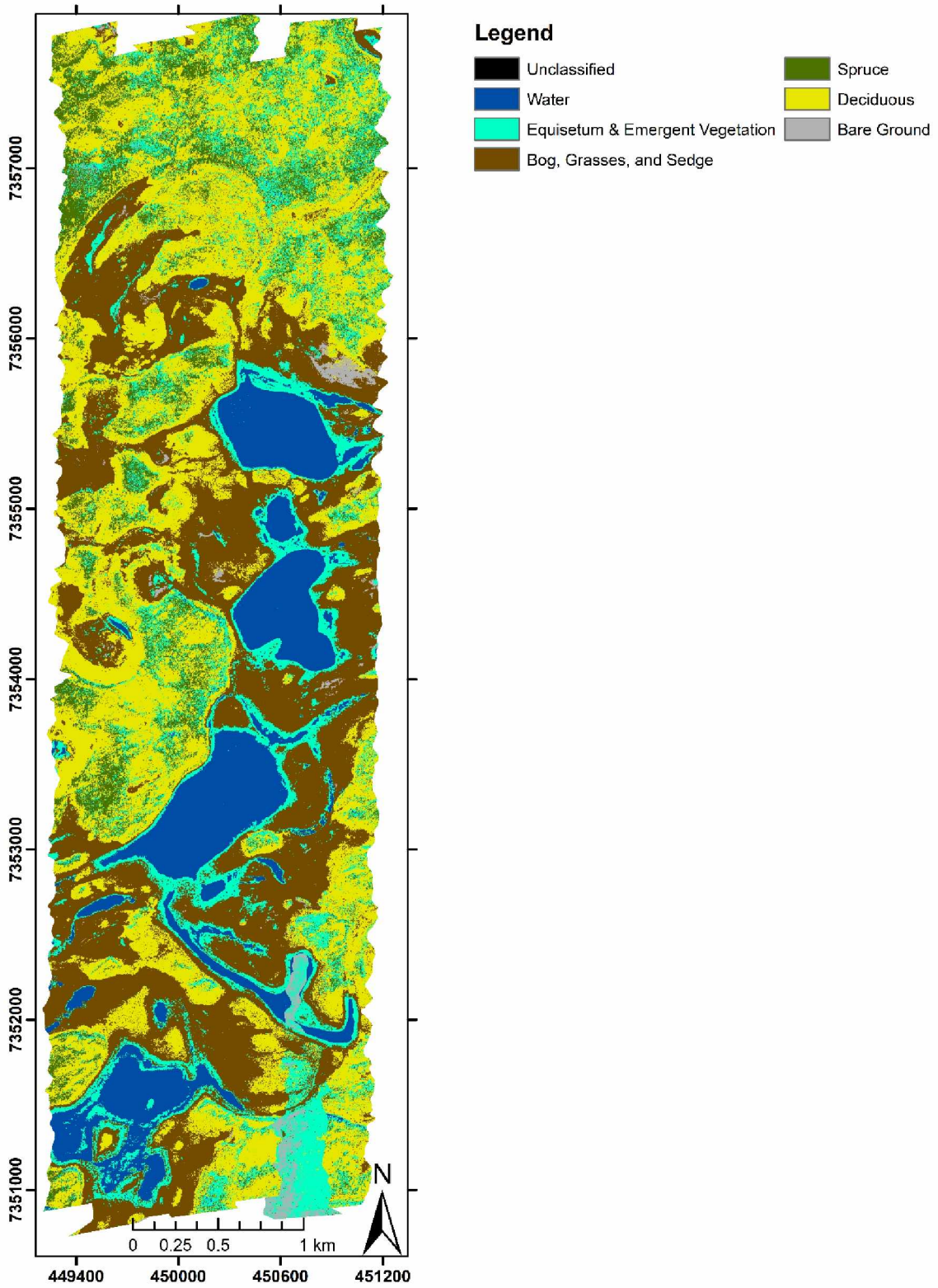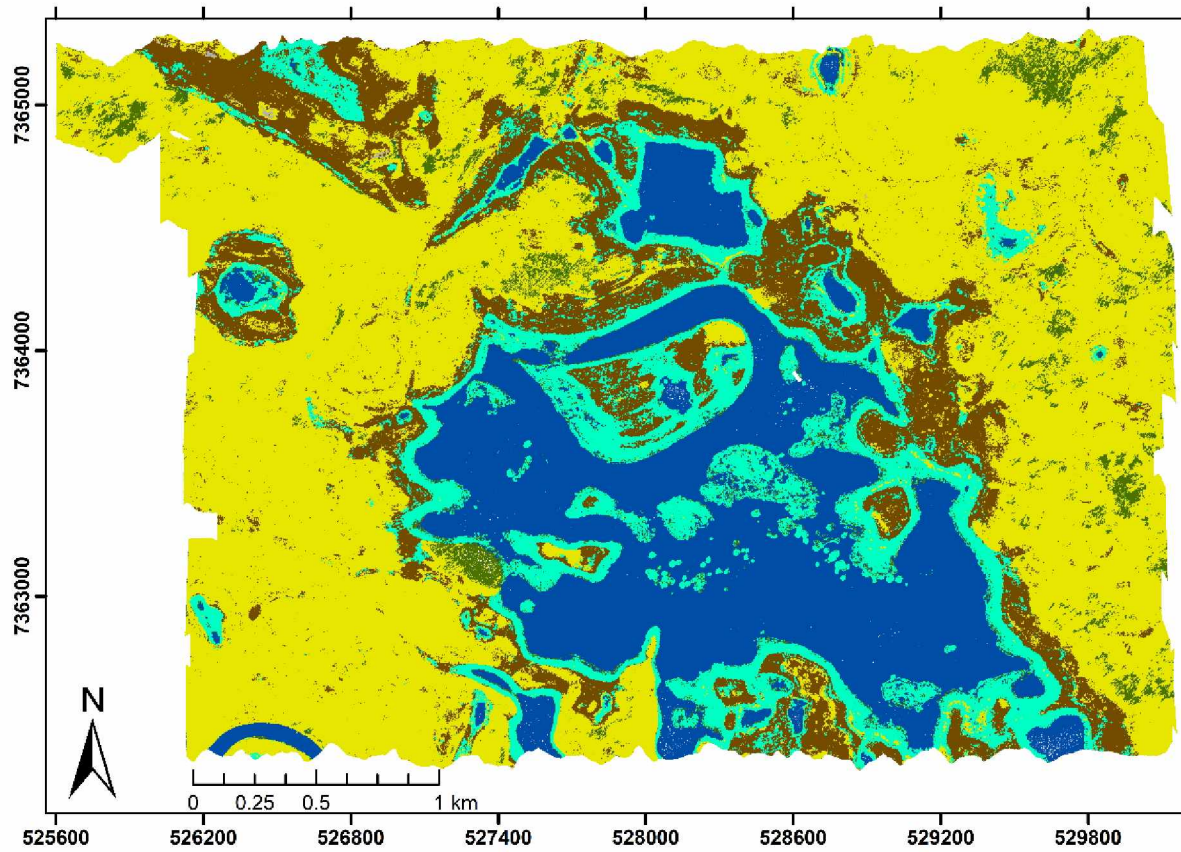
Figure 32. Best hybrid classification for Area C. Coordinates in UTM-6N and datum in WGS-84

Figure 33. Best maximum likelihood classification for Area C. Coordinates in UTM-6N and datum in WGS-84
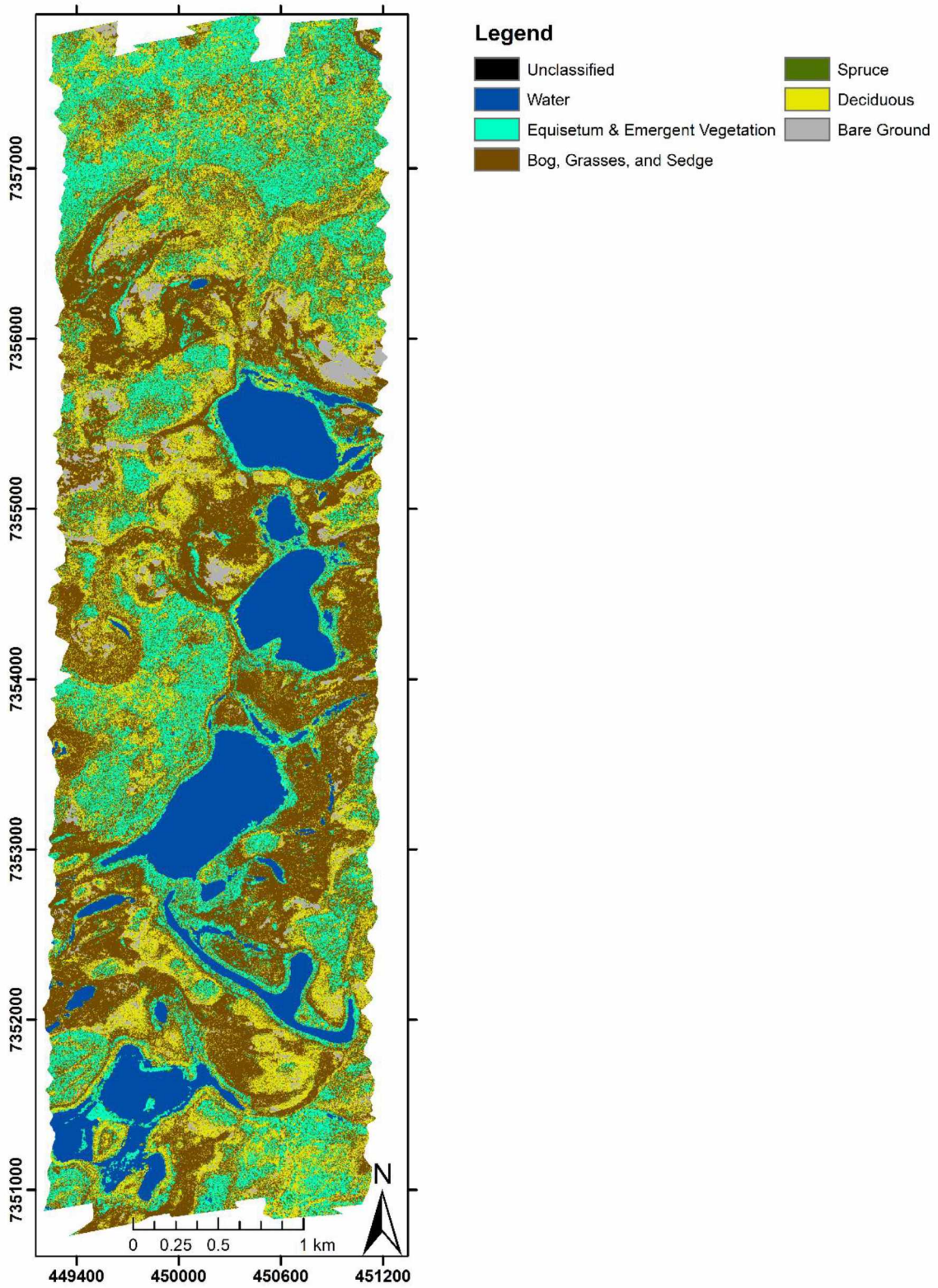
Figure 34. Best SAM classification for Area B. Coordinates in UTM-6N and datum in WGS-84

Figure 35. Best SAM classification for Area C. Coordinates in UTM-6N and datum in WGS-84

Table 10 Confusion matrix for area B hybrid classification. Results in %.

		Thematic map to test							Comission error	User's accuracy
		a	b	c	d	e	f	Total		
Ground truth	Water (a)	99.64	0.00	0.00	0.00	0.00	0.00	100	0	100
	Equisetum (b)	0.00	23.21	1.26	11.72	24.14	0.00	100	59.38	40.62
	Bog (c)	0.00	7.74	44.47	4.14	27.59	34.38	100	28.34	71.66
	Spruce (d)	0.36	52.98	3.52	71.72	16.55	0.00	100	55.17	44.83
	Deciduous (e)	0.00	10.12	0.00	0.69	8.97	0.00	100	58.06	41.94
	Bare ground (f)	0.00	5.36	41.71	0.69	12.41	50.00	100	92.38	7.62
	Total	100	100	100	100	100	100			
	Omission Error	0.36	76.79	55.53	28.28	91.03	50			
	Producer's Accuracy	99.64	23.21	44.47	71.72	8.97	50			

Table 11. Confusion matrix for area C hybrid classification. Results in %.

		Thematic map to test							Comission n error	User's accuracy
		a	b	c	d	e	f	Total		
Ground truth	Water (a)	97.12	0.00	0.00	5.73	0.00	0.00	100	3.71	96.29
	Equisetum (b)	0.00	62.69	0.00	23.35	39.86	0.00	100	56.7	43.3
	Bog (c)	0.00	20.52	4.16	0.00	6.21	2.38	100	83.67	16.33
	Spruce (d)	2.88	0.37	0.00	67.84	16.47	0.00	100	34.19	65.81
	Deciduous (f)	0.00	11.19	9.09	3.08	34.37	4.76	100	33.94	66.06
	Bare ground (g)	0.00	5.22	86.75	0.00	3.10	92.86	100	90.25	9.75
	Total	100	100	100	100	100	100			
	Omission Error	2.88	37.31	95.84	32.16	65.63	7.14			
	Producer's Accuracy	97.12	62.69	4.16	67.84	34.37	92.86			

Table 12. Confusion matrix for area B maximum likelihood classification. Results in %

		Thematic map to test							Comission error	User's accuracy
		a	b	c	d	e	f	Total		
Ground truth	Water (a)	98.22	0.60	0.00	0.00	0.00	0.00	100	0.36	99.64
	Equisetum (b)	1.78	98.81	1.51	14.48	1.38	0.00	100	17.41	82.59
	Bog (c)	0.00	0.00	86.43	6.90	6.90	7.79	100	7.03	92.97
	Spruce (d)	0.00	0.60	0.00	61.38	0.69	0.00	100	2.2	97.8
	Deciduous (e)	0.00	0.00	4.27	17.24	91.03	0.00	100	24.14	75.86
	Bare ground (f)	0.00	0.00	7.79	0.00	0.00	92.21	100	55.36	44.64
	Total	100	100	100	100	100	100			
	Omission Error	1.78	1.19	13.57	38.62	8.97	21.88			
	Producer's Accuracy	98.22	98.81	86.43	61.38	91.03	78.13			

Table 13. Confusion matrix for area C maximum likelihood classification. Results in %.

Ground truth	Thematic map to test								
		a	b	c	d	e	f	Total	Comission error	User's accuracy
	Water (a)	98.56	0.00	0.00	2.20	0.00	0.00	100	1.44	98.56
	Equisetum (b)	0.29	99.25	4.42	0.00	0.48	0.00	100	6.99	93.01
	Bog (c)	0.00	0.37	94.55	0.00	0.24	0.00	100	1.89	98.11
	Spruce (d)	1.15	0.00	0.26	69.16	0.00	0.00	100	3.09	96.91
	Deciduous (e)	0.00	0.37	0.78	28.63	99.28	0.00	100	18.27	81.73
	Bare ground (f)	0.00	11.90	0.00	0.00	57.14	30.95	100	0	100
	Total	100	100	100	100	100	100			
	Omission Error	1.44	0.75	5.45	30.84	0.72	69.05			
	Producer's Accuracy	98.56	99.25	94.55	69.16	99.28	30.95			

Table 14. Confusion matrix for area B SAM classification. Results in %.

Ground truth	Thematic map to test								
		a	b	c	d	e	f	Total	Comission error	User's accuracy
	Water (a)	100.00	0.00	0.00	0.00	0.00	0.00	100	0.00	100.00
	Equisetum (b)	0.00	70.83	12.06	60.69	28.28	0.00	100	59.80	40.20
	Bog (c)	0.00	4.17	57.29	4.83	15.17	0.00	100	13.64	86.36
	Spruce (d)	0.00	24.40	0.00	31.72	8.97	0.00	100	54.00	46.00
	Deciduous (e)	0.00	0.60	7.54	2.76	45.52	9.38	100	36.54	63.46
	Bare ground (f)	0.00	0.00	23.12	0.00	2.07	90.63	100	76.61	23.39
	Total	100	100	100	100	100	100			
	Omission Error	0.00	29.17	42.71	68.28	54.48	9.38			
	Producer's Accuracy	100.00	70.83	57.29	31.72	45.52	90.62			

Table 15. Confusion matrix for area C SAM classification. Results in %.

Ground truth	Thematic map to test								
		a	b	c	d	e	f	Total	Comission error	User's accuracy
	Water (a)	99.43	0.00	0.00	0.45	0.00	0.00	100	0.29	99.71
	Equisetum (b)	0.00	35.43	0.00	34.08	19.21	0.00	100	63.11	36.89
	Bog (c)	0.00	0.00	93.07	7.62	23.40	53.66	100	27.74	72.26
	Spruce (d)	0.00	1.97	0.00	52.02	18.23	0.00	100	40.51	59.49
	Deciduous (e)	0.00	62.60	6.93	5.83	39.16	0.00	100	55.46	44.54
	Bare ground (f)	0.00	0.00	0.00	0.00	0.00	46.34	100	0.00	100.00
	Total	100	100	100	100	100	100			
	Omission Error	0.57	64.57	6.93	47.98	60.84	53.66			
	Producer's Accuracy	99.43	35.43	93.07	52.02	39.16	46.34			

6. Conclusions and Future Work

In this study a hyperspectral imaging system (HySpex), purchased when UAF established HyLab (http://hyperspectral.alaska.edu/) was commissioned in a small airplane (Bush Hawk). Data were acquired, processed and used to successfully map wetland areas in a remote region of Interior Alaska, the Yukon Flats National Wildlife Refuge.

Improvements in sensor commissioning were achieved by designing a customized board to install the hyperspectral cameras (VNIR and SWIR) that allows for sensor integration in small airplanes and minimized the data loss due to a precise camera set-up.

Hyperspectral data acquisition was carefully planned considering the study area was in a high latitude environment with strong BRDF effects, taking into account considerations of flight direction, flight speed, and flight acquisition time, among others. Data were taken in seven areas with different types of vegetation cover and lakes of differing water chemistry in a clear sky, two-day mission in early September, 2015.

Hyperspectral data were processed according to a processing chain developed by the German Space Agency (DLR) that was improved for high latitude environments, by adding a step for BRDF correction. A test flight was carried out at UAF to ensure proper bore-sight calibration between the VNIR and SWIR camera and radiometry quality. Thanks to this test flight each flightline was geometrically corrected with a RMSE of 0.5 pixels at 1 m spatial resolution for both VNIR and SWIR cameras. ATCOR4 was used to successfully radiometrically correct the imagery using water vapor from the Terra/Aqua water vapor product (MOD05). Due to logistics, no field spectral measurements could be collected concurrent to the airborne mission. Once radiometrically corrected, every flightline for each area was mosaicked automatically using tie-points between

flightlines. In a few areas where automatic flightline co-registration failed due to lack of automatic tie-points, tie-points were selected manually to accurately mosaic the imagery.

For wetlands mapping, a 6-category legend was established based on previous USGS and USFW information and maps and three different classification methods were used in two selected areas: hybrid classification, spectral angle mapper and maximum likelihood. To train and test the classifiers more than 50 polygons of around 7 by7 m were digitized per each category and study area (around 600 polygons). Final maps were successfully classified using a maximum likelihood method with Kappa values and user's and producer's accuracy are more than 90 % for almost all categories. Best classification performance occurred when using the maximum likelihood classifier, followed by the SAM classifier and lastly by the hybrid classifier, with the classifier resulting in a Kappa index of around 0.9, 0.6 and 0.4, respectively for both areas. Although SAM methodology is specifically suited for hyperspectral mapping, the lack of field spectra hampered the final outcome. It is important to note that spruce and equisetum spectra in emergent areas are quite similar due to decrease in reflectance caused by the integration of water in pixels covering areas of emergent vegetation. This led to misclassification especially in SAM and hybrid classifiers decreasing their performance. Misclassification also occurred between spruce and deciduous categories, although it was minor.

This research has contributed to the current body of knowledge that may be utilized for understanding and quantifying the effects, impacts, and implications of a changing global climate by demonstrating the viability of airborne hyperspectral imaging for wetland mapping in Alaska. Procedures and methods of integrating the HySpex camera system into small aircraft suitable for missions in the state have been developed, allowing for repeated image acquisition campaigns and flexibility in platform. Effective data processing procedures that ensure a high level of data

integrity and accuracy have been established and may be developed further to improve results in successive studies. High-resolution, orthorectified imagery with good radiometry has been produced for an area where only low-resolution and decades-old imagery existed before and has demonstrated capability for accurate land cover classification. This imagery is, therefore, an important contribution for detailed mapping and monitoring of vegetation cover, which is critical to understand how vegetation is responding to the rapidly changing climate in Interior Alaska.

In order to improve the results of future work several elements are recommended:

1. In the case of repeating a similar campaign in the same area, use more accurate GPS measurements to improve georectification such as RTK measurements.

2. Build a spectral library for Alaska vegetation and concurrently collect ground spectral measurements during acquisition flight for ground training/validation to improve classification efforts, especially for spectral unmixing and other hyperspectral classification techniques that could be applied.

3. In order to improve image classification, acquire LIDAR data or use a digital surface model derived from standard RGB data to distinguish between equisetum and spruce categories.

References

Adam, E., Mutanga, O., Rugege, D., 2010. Multispectral and hyperspectral remote sensing for identification and mapping of wetland vegetation: a review. Wetlands Ecol Manage 18, 281–296. https://doi.org/10.1007/s11273-009-9169-z

Arctic Council, 2013. Summary for policy-makers. Arctic Resilience Interim Report 2013. Stockholm Environment Institute; Stockholm Resilience Centre, Stockholm, Sweden.

Arp, C.D., Jones, B.M., 2009. Geography of Alaska Lake Districts: Identification, Description, and Analysis of Lake-Rich Regions of a Diverse and Dynamic State (No. 5215), Scientific Investigations Report 2008. U.S. Geological Survey, Reston, Virginia.

Bates, B., Kundzewicz, Z., Wu, S., 2008. Climate Change and Water. Intergovernmental Panel on Climate Change Secretariat.

Bedini, E., 2009. Mapping lithology of the Sarfartoq carbonatite complex, southern West Greenland, using HyMap imaging spectrometer data. Remote Sensing of Environment 113, 1208–1219. https://doi.org/10.1016/j.rse.2009.02.007

Ben-Dor, E., Patkin, K., Banin, A., Karnieli, A., 2002. Mapping of several soil properties using DAIS-7915 hyperspectral scanner data - a case study over clayey soils in Israel. International Journal of Remote Sensing 23, 1043–1062. https://doi.org/10.1080/01431160010006962

Best, R.G., Wehde, M.E., Linder, R.L., 1981. Spectral reflectance of hydrophytes. Remote Sensing of Environment 11, 27–35. https://doi.org/10.1016/0034-4257(81)90004-3

Bhatt, U.S., Walker, D.A., Raynolds, M.K., Comiso, J.C., Epstein, H.E., Jia, G., Gens, R., Pinzon, J.E., Tucker, C.J., Tweedie, C.E., Webber, P.J., 2010. Circumpolar Arctic Tundra Vegetation Change Is Linked to Sea Ice Decline. Earth Interact. 14, 1–20. https://doi.org/10.1175/2010EI315.1

Bintanja, R., Selten, F.M., 2014. Future increases in Arctic precipitation linked to local evaporation and sea-ice retreat. Nature 509, 479–482. https://doi.org/10.1038/nature13259

Boggs, K., Flagstad, L., Boucher, T., Kuo, T., Fehringer, D., Guyer, S., Aisu, M., 2012. Vegetation Map and Classification: Northern, Western, and Interior Alaska. Anchorage: Alaska Natural Heritage Program, University of Alaska 110.

Buchhorn, M., 2014. Ground-based hyperspectral and spectro-directional reflectance characterization of Arctic tundra vegetation communities: field spectroscopy and field spectro-goniometry of Siberian and Alaskan tundra in preparation of the EnMAP satellite mission (phd). Universitaetsverlag Potsdam.

Carter, G.A., 1993. Responses of Leaf Spectral Reflectance to Plant Stress. American Journal of Botany 80, 239–243. https://doi.org/10.2307/2445346

Carter, G.A., Knapp, A.K., 2001. Leaf optical properties in higher plants: linking spectral characteristics to stress and chlorophyll concentration. American Journal of Botany 88, 677–684. https://doi.org/10.2307/2657068

Carter, V., 1996. Wetland hydrology, water quality, and associated functions. National Water Summary on Wetland Resources 35–48.

Chen, M., Rowland, J.C., Wilson, C.J., Altmann, G.L., Brumby, S.P., 2014. Temporal and spatial pattern of thermokarst lake area changes at Yukon Flats, Alaska. Hydrological Processes 28, 837–852. https://doi.org/10.1002/hyp.9642

Clark, R.N., Swayze, G.A., Livo, K.E., Kokaly, R.F., Sutley, S.J., Dalton, J.B., McDougal, R.R., Gent, C.A., 2003. Imaging spectroscopy: Earth and planetary remote sensing with the USGS Tetracorder and expert systems. Journal of Geophysical Research: Planets 108. https://doi.org/10.1029/2002JE001847

Congalton, R.G., 1991. A review of assessing the accuracy of classifications of remotely sensed data. Remote Sensing of Environment 37, 35–46. https://doi.org/10.1016/0034-4257(91)90048-B

Cowardin, L.M., Carter, V., Golet, F.C., Laroe, E.T., 2005. Classification of Wetlands and Deepwater Habitats of the United States, in: Lehr, J.H., Keeley, J. (Eds.), Water Encyclopedia. John Wiley & Sons, Inc., Hoboken, NJ, USA, p. sw2162. https://doi.org/10.1002/047147844X.sw2162

Cristóbal, J., Graham, P., Buchhorn, M., Prakash, A., 2016. A New Integrated High-Latitude Thermal Laboratory for the Characterization of Land Surface Processes in Alaska's Arctic and Boreal Regions. Data 1, 13. https://doi.org/10.3390/data1020013

Dahl, T.E., 1990. Wetlands Losses in the United States 1780s to 1980s (Technical Report No. PB-91-169284/XAB). U.S. Department of the Interior, Fish and Wildlife Service, Washington, D.C.

Davaadorj, A., 2019. EVALUATING ATMOSPHERIC CORRECTION METHODS USING WORLDVIEW-3 IMAGE. University of Twente, Enshede, The Netherlands.

Dell'Endice, F., Nieke, J., Koetz, B., Schaepman, M.E., Itten, K., 2009. Improving radiometry of imaging spectrometers by using programmable spectral regions of interest. ISPRS Journal of Photogrammetry and Remote Sensing 64, 632–639. https://doi.org/10.1016/j.isprsjprs.2009.05.007

Duffy, P.A., Epting, J., Graham, J.M., Rupp, T.S., McGuire, A.D., 2007. Analysis of Alaskan burn severity patterns using remotely sensed data. Int. J. Wildland Fire 16, 277–284. https://doi.org/10.1071/WF06034

Filella, I., Penuelas, J., 2007. The red edge position and shape as indicators of plant chlorophyll content, biomass and hydric status. International Journal of Remote Sensing. https://doi.org/10.1080/01431169408954177

Finlayson, C.M., van der Valk, A.G., 1995. Wetland classification and inventory: A summary. Vegetatio 118, 185–192. https://doi.org/10.1007/BF00045199

Flagstad, L., Steer, A., Boucher, T., Aisu, M., Lema, P., 2013. Wetlands across Alaska: Statewide wetland map and Assessment of rare wetland ecosystems 150.

Ford, J., Bedford, B.L., 1987. The Hydrology of Alaskan Wetlands, U.S.A.: A Review. Arctic and Alpine Research 19, 209–229. https://doi.org/10.1080/00040851.1987.12002596

Goetz, S.J., Bunn, A.G., Fiske, G.J., Houghton, R.A., 2005. Satellite-observed photosynthetic trends across boreal North America associated with climate and fire disturbance. PNAS 102, 13521–13525. https://doi.org/10.1073/pnas.0506179102

Govender, M., Chetty, K., Bulcock, H., 2009. A review of hyperspectral remote sensing and its application in vegetation and water resource studies. WSA 33. https://doi.org/10.4314/wsa.v33i2.49049

Green, R.O., Team, C., 2017. New measurements of the earth's spectroscopic diversity acquired during the aviris-ng campaign to India, in: 2017 IEEE International Geoscience and Remote Sensing Symposium (IGARSS). Presented at the 2017 IEEE International Geoscience and Remote Sensing Symposium (IGARSS), IEEE, Fort Worth, TX, pp. 3066–3069. https://doi.org/10.1109/IGARSS.2017.8127646

Hall, J.V., Frayer, W.E., Wilen, B.O., 1994. Status of Alaska Wetlands. U.S. Fish and Wildlife Service, Anchorage, Alaska.

Harken, J., Sugumaran, R., 2005. Classification of Iowa wetlands using an airborne hyperspectral image: a comparison of the spectral angle mapper classifier and an object-oriented approach. Canadian Journal of Remote Sensing 31, 167–174. https://doi.org/10.5589/m05-003

Heglund, P.J., 1994. Patterns of wetland use among aquatic birds in the interior boreal forest region of Alaska. (Ph.D. Dissertation). University of Missouri, Columbia, Missouri, USA.

Heglund, P.J., Jones, J.R., 2003. Limnology of Shallow Lakes in the Yukon Flats National Wildlife Refuge, Interior Alaska. Lake and Reservoir Management 19, 133–140. https://doi.org/10.1080/07438140309354079

Huntington, T.G., 2006. Evidence for intensification of the global water cycle: Review and synthesis. Journal of Hydrology 319, 83–95. https://doi.org/10.1016/j.jhydrol.2005.07.003

Jackson, R.B., Carpenter, S.R., Dahm, C.N., McKnight, D.M., Naiman, R.J., Postel, S.L., Running, S.W., 2001. Water in a Changing World. Ecological Applications 11, 1027–1045. https://doi.org/10.1890/1051-0761(2001)011[1027:WIACW]2.0.CO;2

Jia, G.J., Epstein, H.E., Walker, D.A., 2003. Greening of arctic Alaska, 1981–2001. Geophysical Research Letters 30. https://doi.org/10.1029/2003GL018268

Johnson, E.A., 1996. Fire and Vegetation Dynamics: Studies from the North American Boreal Forest. Cambridge University Press.

Jollineau, M.Y., Howarth, P.J., 2008. Mapping an inland wetland complex using hyperspectral imagery. International Journal of Remote Sensing 29, 3609–3631. https://doi.org/10.1080/01431160701469099

Jorgenson, M.T., Racine, C.H., Walters, J.C., Osterkamp, T.E., 2001. Permafrost degradation and ecological changes associated with a warming climate in central Alaska. Climatic Change 48, 551–579. https://doi.org/10.1023/A:1005667424292

Jorgenson, M.T., Roth, J.E., Emers, M., Davis, W.A., Schlentner, S.F., Macander, M.J., 2004. Landcover Mapping for Bering Land Bridge National Preserve and Cape Krusenstern National Monument, Northwestern Alaska. Fort Collins, Colorado: US Department of the Interior, National Park Service.

Jorgenson, M.T., Shur, Y.L., Pullman, E.R., 2006. Abrupt increase in permafrost degradation in Arctic Alaska. Geophys. Res. Lett. 33, L02503. https://doi.org/10.1029/2005GL024960

Jung, M., Reichstein, M., Ciais, P., Seneviratne, S.I., Sheffield, J., Goulden, M.L., Bonan, G., Cescatti, A., Chen, J., Jeu, R. de, Dolman, A.J., Eugster, W., Gerten, D., Gianelle, D., Gobron, N., Heinke, J., Kimball, J., Law, B.E., Montagnani, L., Mu, Q., Mueller, B., Oleson, K., Papale, D., Richardson, A.D., Roupsard, O., Running, S., Tomelleri, E., Viovy, N., Weber, U., Williams, C., Wood, E., Zaehle, S., Zhang, K., 2010. Recent decline in the global land evapotranspiration trend due to limited moisture supply. Nature 467, 951–954. https://doi.org/10.1038/nature09396

Kaufmann, H., Förster, S., Wulf, H., Segl, K., Guanter, L., Bochow, M., Heiden, U., Müller, A., Heldens, W., Schneiderhan, T., others, 2012. Science plan of the environmental mapping and analysis program (EnMAP) (Technical Report). Deutsches GeoForschungsZentrum GFZ, Potsdam.

Klemas, V., 2011. Remote Sensing of Wetlands: Case Studies Comparing Practical Techniques. coas 27, 418–427. https://doi.org/10.2112/JCOASTRES-D-10-00174.1

Knipling, E.B., 1970. Physical and physiological basis for the reflectance of visible and near-infrared radiation from vegetation. Remote Sensing of Environment 1, 155–159. https://doi.org/10.1016/S0034-4257(70)80021-9

Kruse, F.A., Lefkoff, A.B., Boardman, J.W., Heidebrecht, K.B., Shapiro, A.T., Barloon, P.J., Goetz, A.F.H., 1993. The spectral image processing system (SIPS)—interactive visualization and analysis of imaging spectrometer data. Remote Sensing of Environment, Airbone Imaging Spectrometry 44, 145–163. https://doi.org/10.1016/0034-4257(93)90013-N

Lammers, R.B., Shiklomanov, A.I., Vörösmarty, C.J., Fekete, B.M., Peterson, B.J., 2001. Assessment of contemporary Arctic river runoff based on observational discharge records. Journal of Geophysical Research: Atmospheres 106, 3321–3334. https://doi.org/10.1029/2000JD900444

Leckie, D.G., Cloney, E.E., Jay, C., Paradine, D., 2005. Automated mapping of stream features with high-resolution multi-spectral imagery: an example of the capabilities.

Lewis, T.L., Lindberg, M.S., Schmutz, J.A., Bertram, M.R., Dubour, A.J., 2015a. Species richness and distributions of boreal waterbird broods in relation to nesting and brood-rearing habitats: Distribution and Diversity of Waterbird Broods. Jour. Wild. Mgmt. 79, 296–310. https://doi.org/10.1002/jwmg.837

Lewis, T.L., Lindberg, M.S., Schmutz, J.A., Heglund, P.J., Rover, J., Koch, J.C., Bertram, M.R., 2015b. Pronounced chemical response of Subarctic lakes to climate-driven losses in surface area. Global Change Biology 21, 1140–1152. https://doi.org/10.1111/gcb.12759

Matsapey, N., Faucheu, J., Flury, M., Delafosse, D., 2013. Design of a gonio-spectro-photometer for optical characterization of gonio-apparent materials. Measurement Science and Technology 24, 065901. https://doi.org/10.1088/0957-0233/24/6/065901

McGuire, A.D., Wirth, C., Apps, M., Beringer, J., Clein, J., Epstein, H., Kicklighter, D.W., Bhatti, J., Chapin, F.S., Groot, B. de, Efremov, D., Eugster, W., Fukuda, M., Gower, T., Hinzman, L., Huntley, B., Jia, G.J., Kasischke, E., Melillo, J., Romanovsky, V., Shvidenko, A., Vaganov, E., Walker, D., 2002. Environmental variation, vegetation distribution, carbon dynamics and water/energy exchange at high latitudes. Journal of Vegetation Science 13, 301–314. https://doi.org/10.1111/j.1654-1103.2002.tb02055.x

Meltofte, H. (Ed.), 2013. Arctic Biodiversity Assessment: status and trends in Arcitc biodiversity. The Conservation of Arctic Flora and Fauna, Akureyri, Iceland.

Niemi, G.J., McDonald, M.E., 2004. Application of Ecological Indicators. Annu. Rev. Ecol. Evol. Syst. 35, 89–111. https://doi.org/10.1146/annurev.ecolsys.35.112202.130132

Norsk Elektro Optikk, 2014. Imaging Spectrometer Users Manual.

Ozesmi, S.L., Bauer, M.E., 2002. Satellite remote sensing of wetlands. Wetlands Ecology and Management 10, 381–402. https://doi.org/10.1023/A:1020908432489

Pastick, N.J., Jorgenson, M.T., Wylie, B.K., Minsley, B.J., Ji, L., Walvoord, M.A., Smith, B.D., Abraham, J.D., Rose, J.R., 2013. Extending Airborne Electromagnetic Surveys for Regional Active Layer and Permafrost Mapping with Remote Sensing and Ancillary Data, Yukon Flats Ecoregion, Central Alaska. Permafrost and Periglacial Processes 24, 184–199. https://doi.org/10.1002/ppp.1775

Randerson, J.T., Liu, H., Flanner, M.G., Chambers, S.D., Jin, Y., Hess, P.G., Pfister, G., Mack, M.C., Treseder, K.K., Welp, L.R., Chapin, F.S., Harden, J.W., Goulden, M.L., Lyons, E., Neff, J.C., Schuur, E. a. G., Zender, C.S., 2006. The Impact of Boreal Forest Fire on Climate Warming. Science 314, 1130–1132. https://doi.org/10.1126/science.1132075

Richards, J.A., 2013. Supervised Classification Techniques, in: Richards, J.A. (Ed.), Remote Sensing Digital Image Analysis: An Introduction. Springer, Berlin, Heidelberg, pp. 247–318. https://doi.org/10.1007/978-3-642-30062-2_8

Richter, R., Schlapfer, D., 2015. Atmospheric / Topographic Correction for Airborne Imagery. ReSe Applications, Langeggweg 3, Ch-9500 wil SG, Switzerland, 1 DLR - German Aerospace Center, D - 82234 Wessling, Germany.

Roach, J.K., Griffith, B., Verbyla, D., 2013. Landscape influences on climate-related lake shrinkage at high latitudes. Global Change Biology 19, 2276–2284. https://doi.org/10.1111/gcb.12196

Schläpfer, D., Richter, R., 2014. Evaluation of brefcor BRDF effects correction for HYSPEX, CASI, and APEX imaging spectroscopy data, in: 2014 6th Workshop on Hyperspectral Image and Signal Processing: Evolution in Remote Sensing (WHISPERS). Presented at the 2014 6th Workshop on Hyperspectral Image and Signal Processing: Evolution in Remote Sensing (WHISPERS), pp. 1–4. https://doi.org/10.1109/WHISPERS.2014.8077488

Schmidt, K.S., Skidmore, A.K., 2003. Spectral discrimination of vegetation types in a coastal wetland. Remote Sensing of Environment 85, 92–108. https://doi.org/10.1016/S0034-4257(02)00196-7

Schuur, E.A.G., Bockheim, J., Canadell, J.G., Euskirchen, E., Field, C.B., Goryachkin, S.V., Hagemann, S., Kuhry, P., Lafleur, P.M., Lee, H., Mazhitova, G., Nelson, F.E., Rinke, A., Romanovsky, V.E., Shiklomanov, N., Tarnocai, C., Venevsky, S., Vogel, J.G., Zimov, S.A., 2008. Vulnerability of Permafrost Carbon to Climate Change: Implications for the Global Carbon Cycle. BioScience 58, 701–714. https://doi.org/10.1641/B580807

Serra, P., Pons, X., Saurí, D., 2003. Post-classification change detection with data from different sensors: Some accuracy considerations. International Journal of Remote Sensing 24, 3311–3340. https://doi.org/10.1080/0143116021000021189

Serreze, M.C., Barry, R.G., 2011. Processes and impacts of Arctic amplification: A research synthesis. Global and Planetary Change 77, 85–96. https://doi.org/10.1016/j.gloplacha.2011.03.004

Shur, Y., Kanevskiy, M., Jorgenson, T., Dillon, M., Stephani, E., Bray, M., Fortier, D., 2012. Permafrost Degradation and Thaw Settlement under Lakes in Yedoma Environment, in: Proceedings of the Tenth International Conference on Permafrost. Presented at the Tenth International Conference on Permafrost, The Northern Publisher, Salekhard, Russia, pp. 5–29.

Silva, T.S.F., Costa, M.P.F., Melack, J.M., Novo, E.M.L.M., 2008. Remote sensing of aquatic vegetation: theory and applications. Environ Monit Assess 140, 131–145. https://doi.org/10.1007/s10661-007-9855-3

Solomon, S., Manning, M., Marquis, M., Qin, D., 2007. Climate change 2007-the physical science basis: Working group I contribution to the fourth assessment report of the IPCC. Cambridge university press.

Tiner, R.W., 2012. Defining Hydrophytes for Wetland Identification and Delineation: Defense Technical Information Center, Fort Belvoir, VA. https://doi.org/10.21236/ADA555761

Tiner, R.W., 2009. Status report for the National Wetlands Inventory program: 2009. US Fish and Wildlife Service, Division of Habitat and Resource Conservation, Branch of Resource and Mapping Support, Arlington, Virginia, USA.

Verbyla, D., 2008. The greening and browning of Alaska based on 1982–2003 satellite data. Global Ecology and Biogeography 17, 547–555. https://doi.org/10.1111/j.1466-8238.2008.00396.x

Wendler, G., Shulski, M., 2009. A Century of Climate Change for Fairbanks, Alaska. Arctic 62, 295-295–300. https://doi.org/10.14430/arctic149

Xu, L., Myneni, R.B., Iii, F.S.C., Callaghan, T.V., Pinzon, J.E., Tucker, C.J., Zhu, Z., Bi, J., Ciais, P., Tømmervik, H., Euskirchen, E.S., Forbes, B.C., Piao, S.L., Anderson, B.T., Ganguly, S., Nemani, R.R., Goetz, S.J., Beck, P.S.A., Bunn, A.G., Cao, C., Stroeve, J.C., 2013. Temperature and vegetation seasonality diminishment over northern lands. Nature Clim Change 3, 581–586. https://doi.org/10.1038/nclimate1836

Yang, F., Kumar, A., Schlesinger, M.E., Wang, W., 2003. Intensity of Hydrological Cycles in Warmer Climates. J. Climate 16, 2419–2423. https://doi.org/10.1175/2779.1

Appendix 1: Flight planning

From September 2nd to 3rd of 2015, seven areas at Yukon Flats National Wildlife Refuge were flown and hyperspectral imagery was acquired using the HySpex camera (see Figures, 6 11 and 12). Although it was anticipated to fly over 5 areas (area codes: A, B, C, D, E), a total of 7 areas were covered. Two extra areas were opportunistically acquired (area codes: X, Z) as they were of importance for USFW service. However, there was no flight planning for these two areas and in this Appendix only anticipated areas flight plans are shown. Below there is a technical description of the flight planning as they were submitted to USFW before flying.

Flight date: September 2nd and 3rd, 2015

Flight Time: from 12 p.m. to 16 p.m. (AKDT)

Pilot: Nikki Guldager

Flight crew: Dr. Marcel Buchhorn, Dr. Jordi Cristóbal and Mr. Patrick Graham (Geophysical Institute-UAF).

HySpex operator: Mr. Patrick Graham

Flight details:

It was planned to fly over Yukon Flats and it was requested 15 hours flight around solar noon (2 p.m. AKDT) for at least 3 days. It was selected 5 possible flight scenarios and ranked them from 1 to 5 (see table 1). Flights from 1 to 5 should be doable within a 3-hour flight.

Table 16. Flightline specifications per area

Ranking	Sensor-object distance (ft)	Flight height (ft)	Direction	GSD (m)
1	2900 feet, **E-to-W**	2779 ft	East to West	0.5
2	2900 feet, **N-to-S**	2900 ft	North to South	0.5
3	2900 feet, **E-to-W**	2900 ft	East to West	0.5
4	2900 feet, **E-to-W**	2900 ft	East to West	0.5
5	2900 feet, **E-to-W**	2900 ft	East to West	0.5

The imagery will be acquired with a HySpex VNIR-1800 and HySpex SWIR-384 hyperspectral cameras from NEO (more info at http://www.hyspex.no/products/vnir_1800.php). In all cases we plan to fly at 165 km/h (102 mph or 89 knots) and with an effective frame width 40 % to 75 % sidelap.

Flight 1: Yukon Flats Area A, 2779 feet ASL, East to West

Table 17. Flightline specifications for area A (I)

Lowest elevation (m)	100.00
Flying height (AGL in m)	2451.00
Flying height (ASL in m)	849.00
Flying height (ASL in ft)	2779.00
No of lines	13.00
Length of line (km)	5.00
Total length of flight with 3km turning radius (km)	197.00
Flying speed (km/h)	165.00
Total line time (minutes)	72.00

Table 18. Flightline specifications for area A (II)

| line	heading	ASL (ft)	Speed (knots)	start		end	
				Lat (DD)	Long (DD)	Lat (DD)	Long (DD)
1	West	2779	89	64.877738	-147.859608	64.844373	-147.859608
2	West	2779	89	64.877738	-147.8542852	64.844373	-147.8542918
3	West	2779	89	64.877738	-147.8489624	64.844373	-147.8489756
4	West	2779	89	64.877738	-147.8436396	64.844373	-147.8436594
5	West	2779	89	64.877738	-147.8383168	64.844373	-147.8383432
6	West	2779	89	64.877738	-147.832994	64.844373	-147.833027
7	West	2779	89	64.877737	-147.8276711	64.844373	-147.8277108
8	West	2779	89	64.877737	-147.8223483	64.844373	-147.8223945
9	West	2779	89	64.877737	-147.8170255	64.844372	-147.8170783
10	West	2779	89	66.255518	-148.953730	66.255478	-148.841967
11	West	2779	89	66.253258	-148.953730	66.253218	-148.841967
12	West	2779	89	66.250998	-148.953730	66.250958	-148.841967
13	West	2779	89	66.248738	-148.9537303	66.248698	-148.8419673
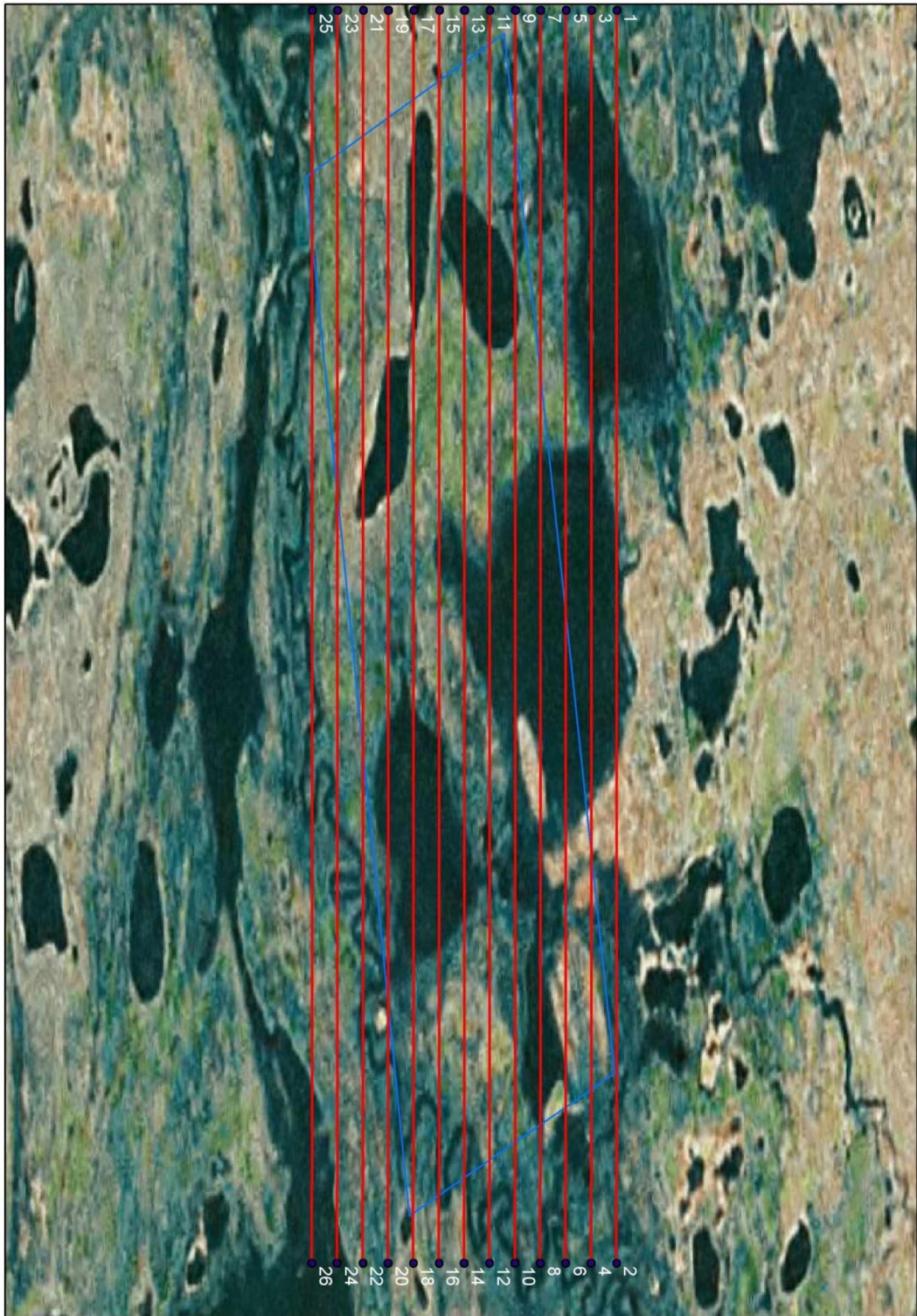
Figure 36. Flight lines for B area.

Flight 2: Yukon Flats Area B, 2779 feet ASL, North to South

Table 19. Flightline specifications for area B (I)

Lowest elevation (m)	100.00
Flying height (AGL in m)	2451.00
Flying height (ASL in m)	849.00
Flying height (ASL in ft)	2779.00
No of lines	7.00
Length of line (km)	5.00
Total length of flight with 3km turning radius (km)	101.00
Flying speed (km/h)	165.00
Total line time (minutes)	37.00

Table 20. Flightline specifications for area B (II)

| line	heading	ASL (ft)	Speed (knots)	start Lat (DD)	start Long (DD)	end Lat (DD)	end Long (DD)
1	South	2779	89	66.320673	-148.1274	66.275707	-148.127409
2	South	2779	89	66.320673	-148.1217	66.275707	-148.121792
3	South	2779	89	66.320673	-148.1161	66.275707	-148.116175
4	South	2779	89	66.320673	-148.1105	66.275707	-148.110558
5	South	2779	89	66.320673	-148.1049	66.275707	-148.104942
6	South	2779	89	66.320673	-148.0992	66.27507	-148.099325
7	South	2779	89	66.32063	-148.0936	66.275706	-148.0937087
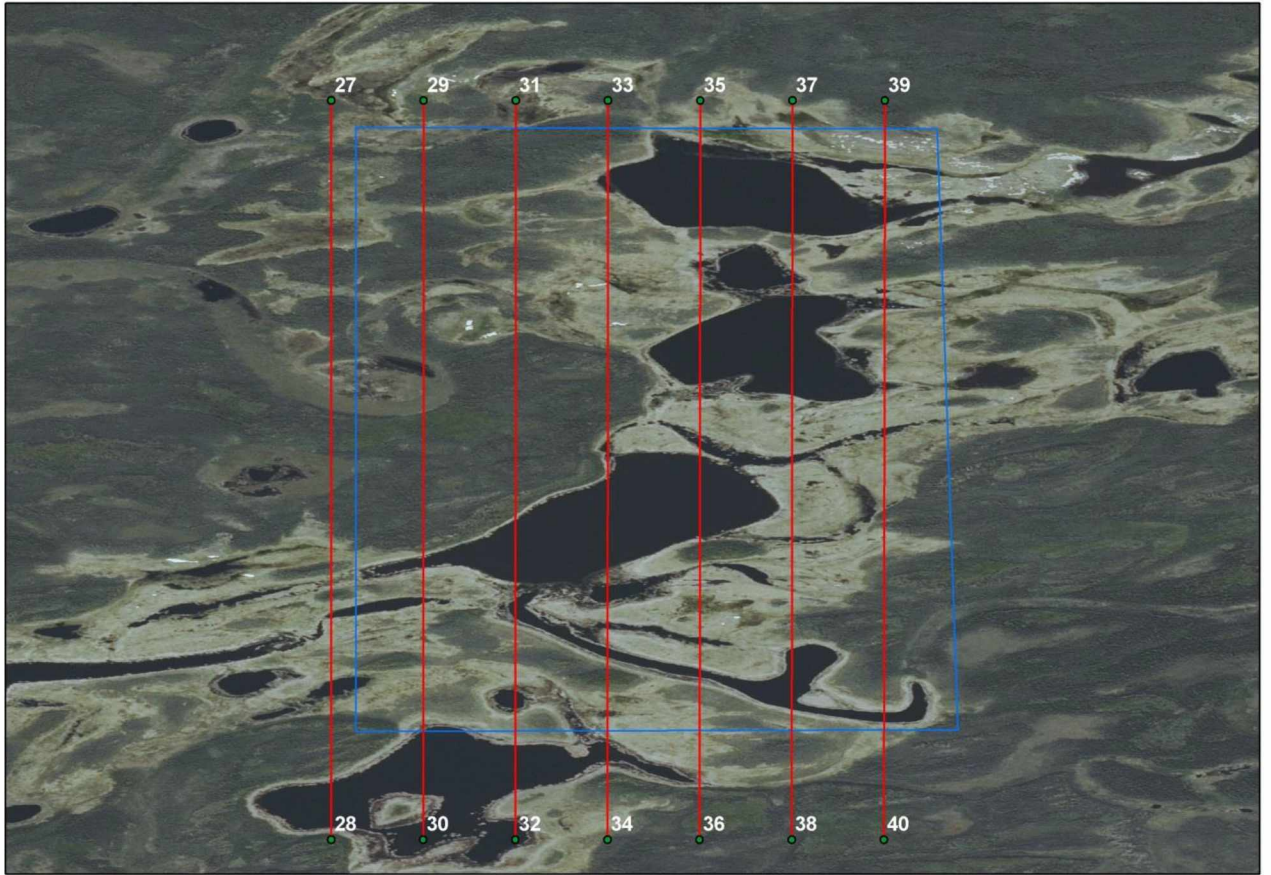
Figure 37. Flight lines for B area.

Flight 4: Yukon Flats Area C, 2779 feet ASL, East to West

Table 21. Flightline specifications for area C (I)

Lowest elevation (m)	100.00
Flying height (AGL in m)	2451.00
Flying height (ASL in m)	849.00
Flying height (ASL in ft)	2779.00
No of lines	11.00
Length of line (km)	3.00
Total length of flight with 3km turning radius (km)	123.00
Flying speed (km/h)	165.00
Total line time (minutes)	45.00

Table 22. Flightline specifications for area C (II)

line	heading	ASL (ft)	Speed (knots)	start		end	
				Lat (DD)	Long (DD)	Lat (DD)	Long (DD)
1	West	2779	89	66.403320	-146.3985	66.43305	-146.331133
2	West	2779	89	66.401060	-146.3985	66.401046	-146.331133
3	West	2779	89	66.398800	-146.3985	66.398786	-146.331133
4	West	2779	89	66.396540	-146.3985	66.396526	-146.331133
5	West	2779	89	66.394281	-146.3985	66.394266	-146.331133
6	West	2779	89	66.392021	-146.3985	66.392006	-146.331133
7	West	2779	89	66.389761	-146.3985	66.389746	-146.331133
8	West	2779	89	66.387501	-146.3985	66.387487	-146.331133
9	West	2779	89	66.385241	-146.3985	66.385227	-146.331133
10	West	2779	89	66.382982	-146.3985	66.382967	-146.331133
11	West	2779	89	66.380722	-146.3985	66.380707	-146.3311339

Figure 38. Flight lines for C area.

Flight 4: Yukon Flats Area D, 2779 feet ASL, East to West

Table 23. Flightline specifications for area D (II)

Lowest elevation (m)	100.00
Flying height (AGL in m)	2451.00
Flying height (ASL in m)	849.00
Flying height (ASL in ft)	2779.00
No of lines	15.00
Length of line (km)	4.00
Total length of flight with 3km turning radius (km)	200.00
Flying speed (km/h)	165.00
Total line time (minutes)	73.00

Table 24. Flightline specifications for area D (II)

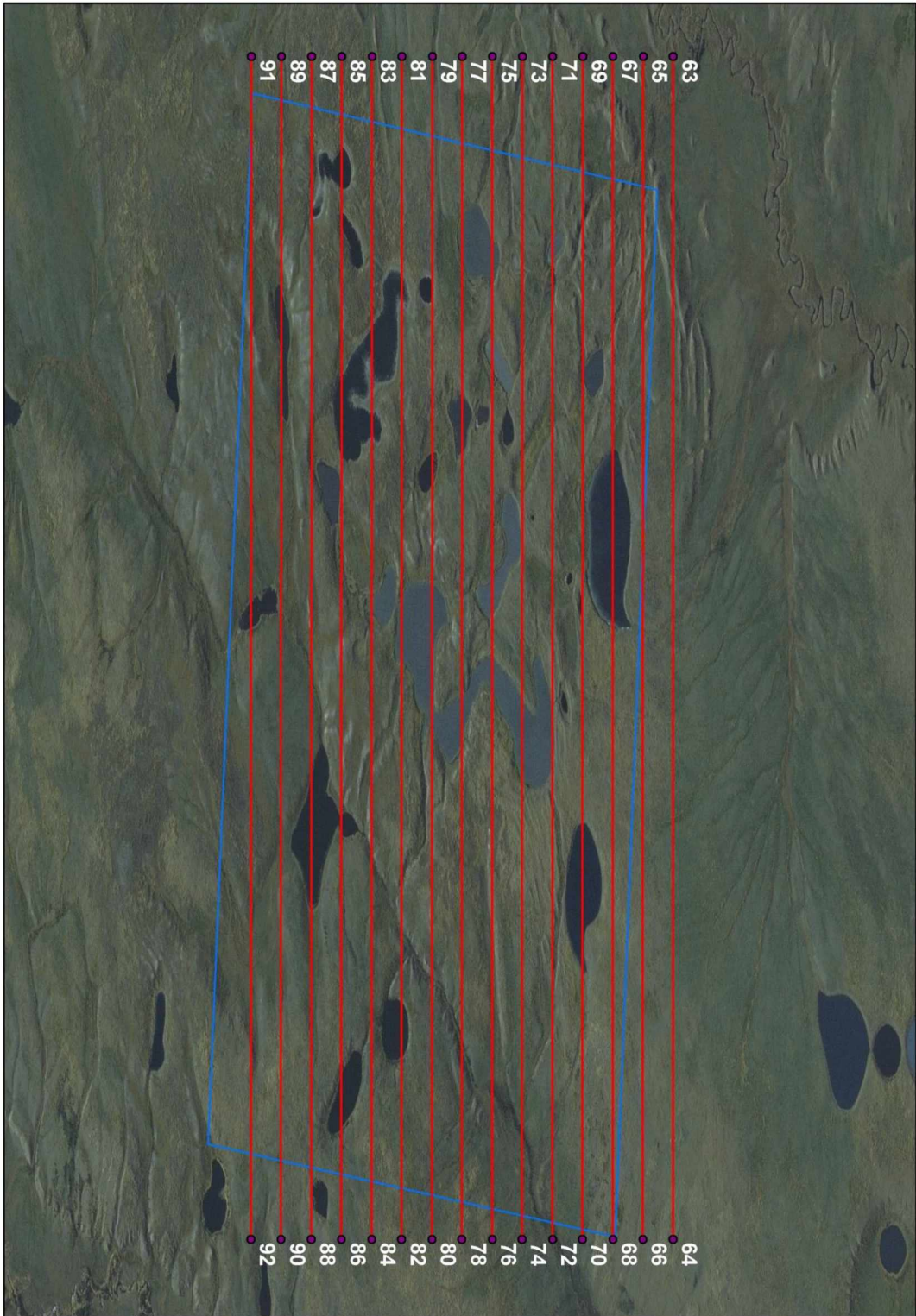| line	heading	ASL (ft)	Speed (knots)	start		End	
				Lat (DD)	Long (DD)	Lat (DD)	Long (DD)
1	West	2779	89	66.403320	-146.3985	66.403305	-146.331133
2	West	2779	89	66.401060	-146.3985	66.401046	-146.331133
3	West	2779	89	66.398800	-146.3985	66.398786	-146.331133
4	West	2779	89	66.396540	-146.3985	66.396526	-146.331133
5	West	2779	89	66.394281	-146.3985	66.394266	-146.331133
6	West	2779	89	66.392021	-146.3985	66.392006	-146.331133
7	West	2779	89	66.389761	-146.3985	66.389746	-146.331133
8	West	2779	89	66.387501	-146.3985	66.387487	-146.331133
9	West	2779	89	66.385241	-146.3985	66.385227	-146.331133
10	West	2779	89	66.382982	-146.3985	66.382967	-146.331133
11	West	2779	89	66.380722	-146.3985	66.380707	-146.331133

Figure 39. Flight lines for D area.

Flight 5: Yukon Flats Area E, 2779 feet ASL, East to West

Table 25. Flightline specifications for area E (I)

Lowest elevation (m)	100.00
Flying height (AGL in m)	2451.00
Flying height (ASL in m)	849.00
Flying height (ASL in ft)	2779.00
No of lines	9.00
Length of line (km)	3.50
Total length of flight with 3km turning radius (km)	107.00
Flying speed (km/h)	165.00
Total line time (minutes)	39.00

Table 26. Flightline specifications for area E (II)

line	heading	ASL (ft)	Speed (knots)	Start		End	
				Lat (DD)	Long (DD)	Lat (DD)	Long (DD)
1	West	2779	89	66.186060	-148.0306	66.186040	-147.952648
2	West	2779	89	66.183800	-148.0306	66.183780	-147.952648
3	West	2779	89	66.181540	-148.0306	66.181520	-147.952648
4	West	2779	89	66.179280	-148.0306	66.179261	-147.952648
5	West	2779	89	66.177020	-148.0306	66.177001	-147.952648
6	West	2779	89	66.174761	-148.0306	66.174741	-147.952648
7	West	2779	89	66.172501	-148.0306	66.172481	-147.952648
8	West	2779	89	66.170241	-148.0306	66.170221	-147.952648
9	West	2779	89	66.167981	-148.0306	66.167962	147.9526482

Figure 40. Flight lines for E area.

Appendix 2: Preprocessing Workflow

The Hyspex data processing workflow was an adapted version of the workflow established by DLR in 2012. It includes an additional step for correcting the effects of Bidrectional Reflection Distribution Function (BRDF), a phenomenon that particularly impacts imagery acquired in high-latitude study sites. For ease, the processing workflow is presented in four steps.

Step 1. Image orthorectification.

For quality control general sensor characteristics (e.g. spectral smile), sensor calibration and performance issues (eg. striping, data drops), and external conditions during overflight (e.g. cloud cover) are assessed (Figure 41). Using the HySpex RAD module (part of the software provided by the manufacturer) the laboratory derived calibration coefficients to convert brightness values (DN values) to at-sensor radiance are applied. The IMU/GPS data is then input in the Hyspex NAV module. Later, images are orthorectified in the PARGE software using the NAV data, the HySpex sensor model, and a digital elevation model (DEM). Additionally, offset angles from a boresight calibration are applied. The outputs from Step 1 are VNIR and SWIR orthorectified images, scan angle files, and DEMs.
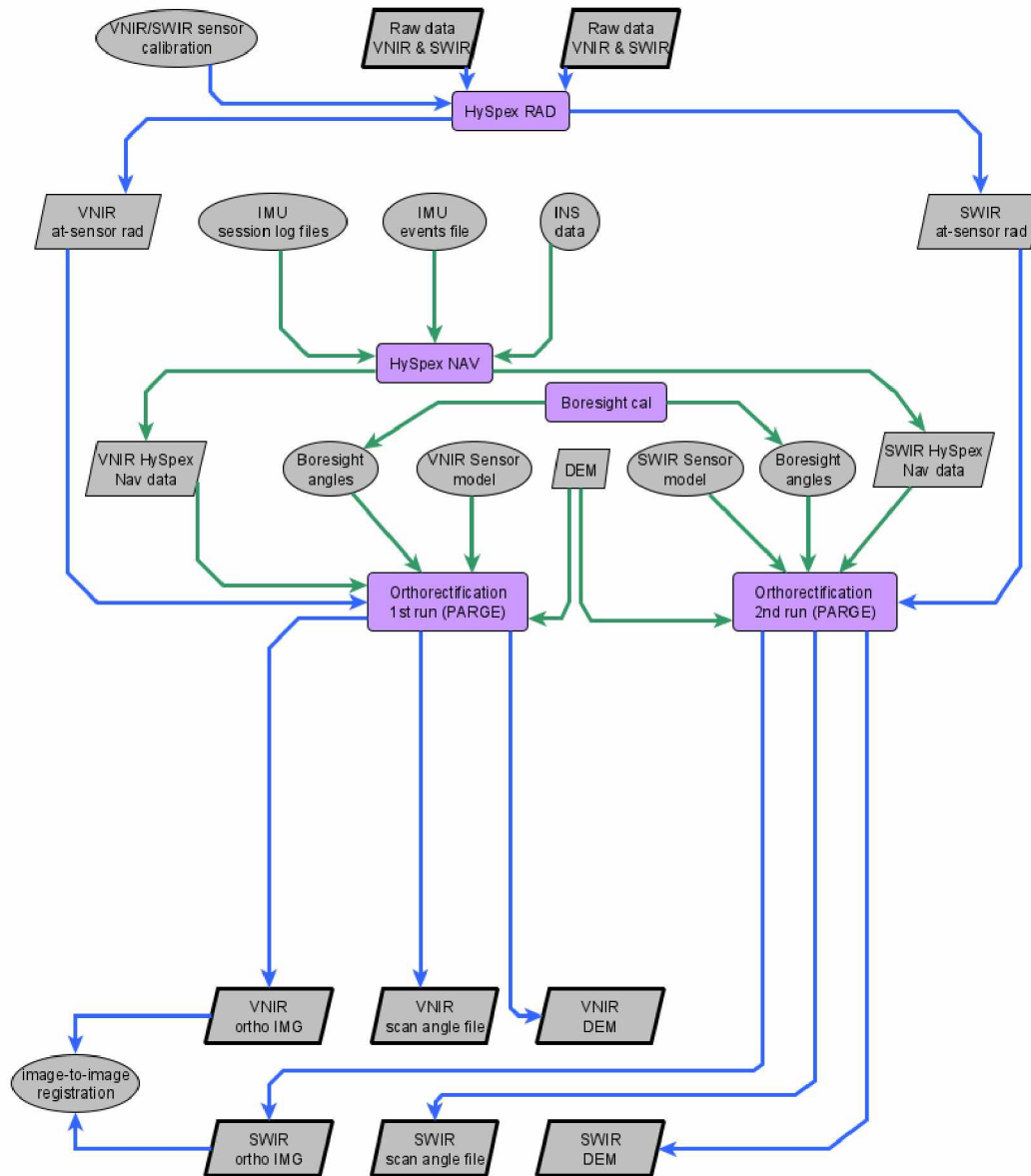
Figure 41. Flow chart diagram of Step 1.

Step 2. Generate supercube and DEM derivatives.

In this step, the orthorectified VNIR and SWIR at-sensor radiance images are stacked. The scan angle files from both sensors are used to generate a mask that includes common image area acquired by both sensors (Figure 42). Finally, the stacked images are clipped with the mask to

generate one large supercube of image data. Furthermore, slope, aspect, and skyview products from the VNIR and SWIR DEMs, generated in Step 1 are derived as they are needed for further processing.
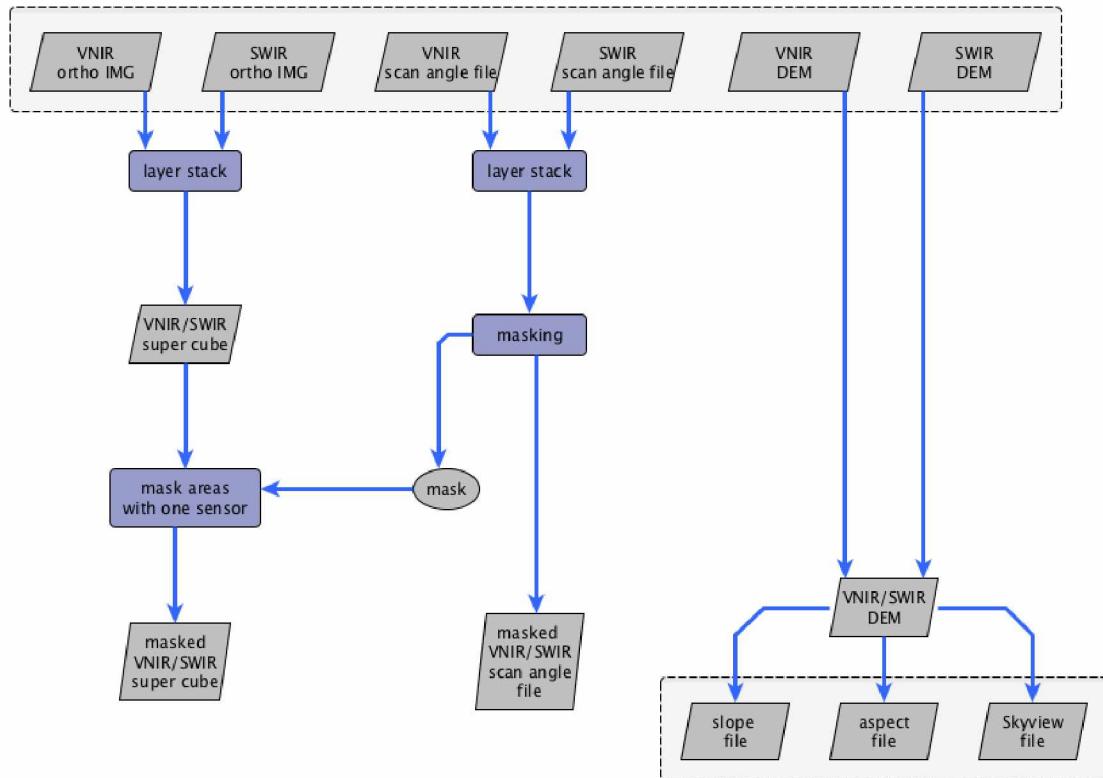

Figure 42. Flow chart diagram of Step 2.

Step 3. Complete radiometric (including atmospheric and BRDF) corrections.

This step brings together several input parameters measured or derived in the earlier steps, into the SPECTRA module (Figure 43). Atmospheric correction is performed using a radiative transfer-based approach with ATCOR software to convert at-sensor radiance to surface reflectance values. Reliable atmospheric correction of the hyperspectral data requires a DEM and robust parameterization of atmospheric column properties including atmospheric gases (water vapor and

oxygen) and aerosol optical thickness (AOT). The user can supply a high-resolution DEM (if available) or the workflow will use the DEM products generated in Step 2. The DEM products are also used to apply BRDF corrections at this stage. Similarly, the user can provide atmospheric parameters based on atmospheric profiles of the study site (if available), or the processing chain will use a modeled standard atmosphere for the specific geographic region. The output from this step is a data cube corrected for geometric, atmospheric, and BRDF effects.
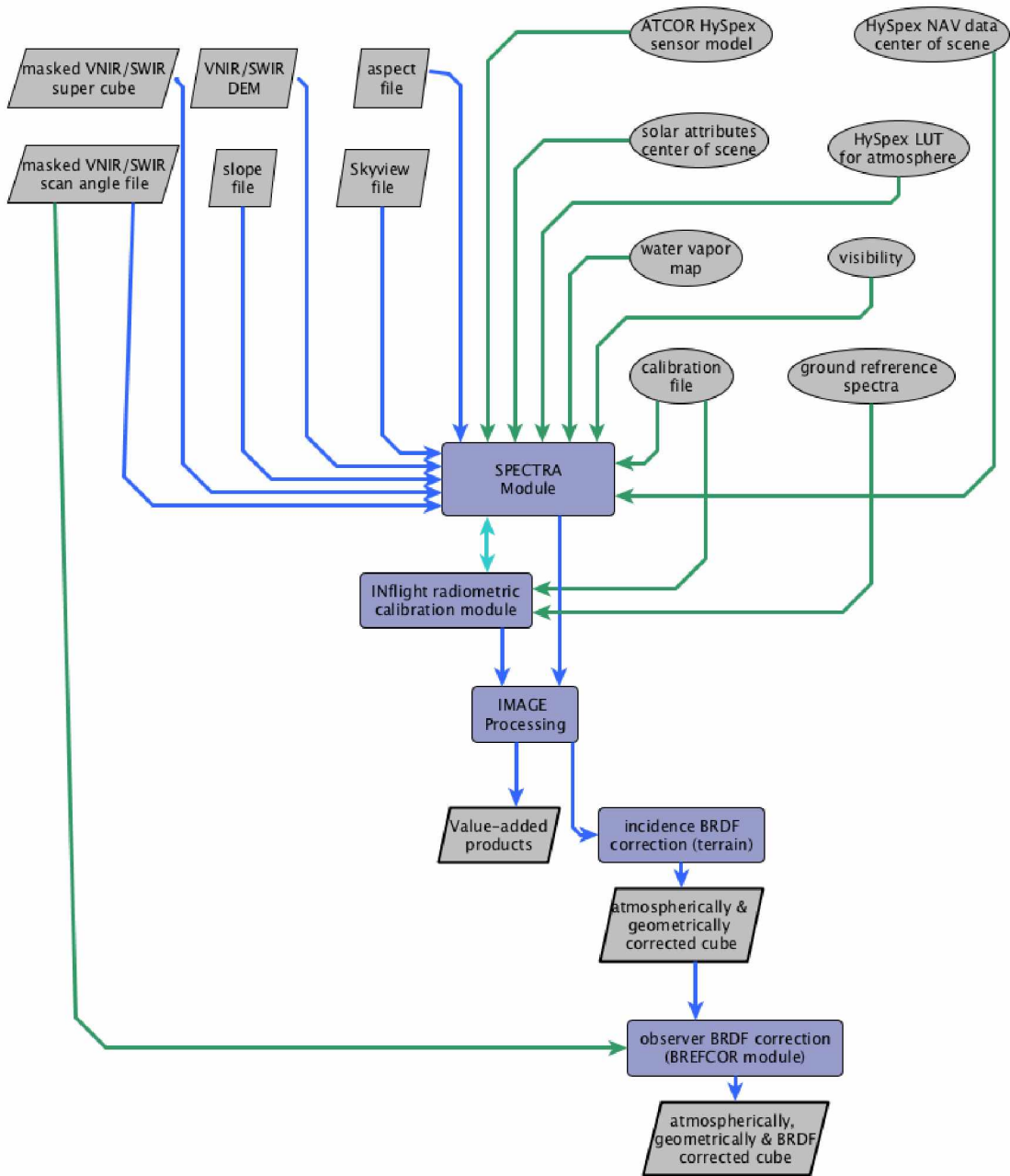
Figure 43. Flow chart diagram of Step 3.

Step 4. Spectral polishing, mosaicking, binning.

Hyspex data has very narrow spectral bands, and even after optimal corrections for spectral smile and atmospheric effects, the spectral profile may contain artifacts (Figure 44). If required, spectral polishing can be applied to remove such remnant artefacts. We then mosaic the individual corrected flight lines. To further increase the signal to noise ratio, if the application so demands, we can perform a spectral binning.
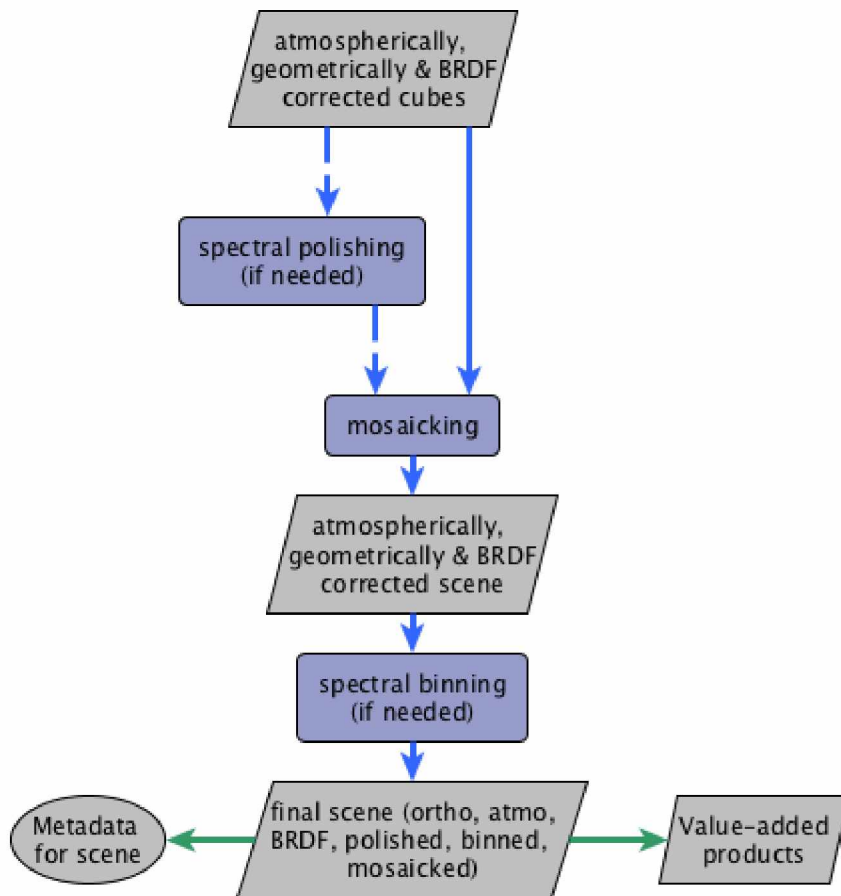
Figure 44. Flow chart diagram of Step 4.